Università degli Studi di Catania

Dipartimento di Matematica e Informatica

Dottorato di ricerca in

MATEMATICA E INFORMATICA

- XXIX CICLO -

DYNAMICS OF PERIODIC STRATIFIED SHEAR FLOWS

Candidato

Giordano Ponetti

Supervisor

Prof. Marco Sammartino

March 2017

Abstract

In this thesis we study instabilities in stratified shear flows where the density stratification is assumed to be stabilizing. Despite the common idea of buoyancy forces having a restoring effects, in few cases such stratifications proved to be capable of destabilizing otherwise stable fluids. Here we study two different systems and how the density stratification affects the stability of their equilibrium solutions.

In the first case we consider the stratified analogue of the Kolmogorov flow which have been widely studied and shows a rich number of states departing from the laminar solution as viscosity is lowered. We conduct finer investigation of the series of transition leading to chaotic states, showing the existence of previously unseen states and proving the chaotic nature of solutions at high Reynolds numbers. Therefore we compare these results to the route to chaos of increasingly stratified fluids and observe that stratification does not affect the bifurcations for Richardson number lower than 10^{-3}. Whereas new dynamics appear when $Ri = 10^{-3}$ or greater. We observe that the stabilizing density gradient increases the critical Reynolds numbers needed to trigger state's transitions, and "unlocks" a number of new states inaccessible to the unstratified Kolmogorov flow.

The second part of the thesis is devoted to the analysis of instabilities due to waves generated by density defects. We consider multilayered fluids with a background linear shear velocity. Layering is a common structure in natural systems as oceans and lakes. The high density gradient between each layer supports the formation of Interfacial waves. Thanks to the background shear velocity these waves can resonantly interact and become unstable (Taylor-Caulfield Instabilities - TCI). The number of density interfaces in a multi-layered fluid allows a multitude of waves to interact and produce structures that may affect the stability of the system. In this work the main purpose is to investigate the susceptibility of a number of constant density layers separated by equally spaced sharp interfaces to TCI and their subsequent nonlinear evolution. We provide a linear instability analysis for a staircase with piecewise-constant density profile, allowing for an arbitrary number of interfaces. The staircase is embedded in a background linear shear flow. For long wavelength, weakly nonlinear structures in weakly stratified fluid, we study the onset of instability. Fully nonlinear states are studied numerically in the long-wave and weak stratification limit.

Acknowledgments

I heartily thank all the people that shared with me the course of my PhD study. First I wish to thank Prof. Marco Sammartino for his guidance and support. I am grateful to him because he introduced me to the mesmerizing world of fluid dynamics and always pushed me to deepen my knowledge. I am also pleased to had the opportunity to spend part of my PhD program as a Visiting Researcher at the University of British Columbia under the supervision of Prof. Neil Balmforth. I am truthfully grateful for his guidance from both scientific and life matters.

I also would like to thank Prof. Maria Carmela Lombardo, Prof. Vincenzo Sciacca, Dr. Francesco Gargano and Dr. Gaetana Gambino at the DiMI of University of Palermo for their guidance, suggestions and pleasant chats. My thanks goes also to my friends and colleagues Rachele and Salvatore who walked this perilous path with me and shared with me joyful and tense moments.

A special thanks goes to my parents and friends, in these years our bonds strengthened day after day. Your ubiquitous presence in my life gave me courage and determination, comfort and love, joy and excitement.

I am grateful for the financial support of Gruppo Nazionale di Fisica Matematica (GNFM-INDAM) grant "Progetto Giovani" which made possible fundamental interactions with the scientific community around the world. I wish to thank the Departments of Mathematics and Informatics from the Universities of Catania, Messina and Palermo, since this PhD Course is due to their joint cooperation and a truthful thank goes to Prof. Giovanni Russo who flawlessly and kindly guided it throughout.

Contents

Chapter 1

Introduction

The hydrodynamic stability studies the stability or instability of given flows in a fluid, and how the onset of instability can eventually lead to turbulent regimes. Thanks to the pioneering works of Helmholtz (1868), Kelvin (1871), Rayleigh (1880) and Reynolds (1883), interest rose on fluid dynamics across the years, still providing a large number of open problems. In simple fluid geometries, Navier-Stokes equations have been widely studied, with scientific community interested in finding simple solutions and their stability properties. Reynolds work on viscous flows in a Poiseuille fluid illustrated how by tuning a single dimensionless parameter, containing physical quantities of the fluid geometry, it is possible to drive the fluid from laminar states up turbulent motions. Inspired by Reynolds' work the Orr-Sommerfeld equation - Orr (1907a,b) and Sommerfeld (1908) - has been derived in order to address the problem of stability of parallel flows to small traveling waves perturbations.

Answer to these questions came from strongly idealized systems, whereas recent works, supported by modern technologies, account for more realistic and physically meaningful phenomenologies. A first step in the analysis of flow states is to study their asymptotic stability, that is trajectories starting nearby converge to the given state eventually. When the first hydrodynamic stability studies have been proposed, the technique of normal modes linear stability analysis was already highly developed for system of particles and rigid bodies. Stability of a given state is investigated by adding a normal mode perturbation of small amplitude. Governing equations are simplified by neglecting the products of perturbations. It is also assumed that time dependence of these modes is exponential - i.e. $e^{-i\omega t}$ where ω is their growth rate. This quantity can be complex and when $\omega > 0$ arbitrarily

small normal modes are unstable, that is they will grow exponentially until are no longer small and nonlinearities are no more negligible. The aforementioned works, inspired by this analysis, introduced the method of normal modes to fluid dynamics. The transition from ordinary differential equations, describing particles and rigid body physics, to partial differential equations, typical in continuum mechanics, marked a perilous path for hydrodynamic stability which have been overcome only in few (simple) flow configurations. In these cases the mathematics is simple enough to provide a detailed stability analysis, where informations as wavelength, growth rate, phase speed of unstable waves can be computed analytically or numerically. Disturbances detected by the linear stability approach can grow until becoming strong enough that their products in the governing equations are no more negligible. Therefore nonlinear phenomena saturate the disturbances to finite amplitude equilibrium states. In some cases the new state may suffer secondary instabilities possibly reaching another steady state, and so on. Finally, the flow has so many large disturbances with random phase that its state becomes chaotic. The linear stability analysis of normal modes perturbations therefore examines only the initial behavior of the disturbances. When laminar states become unstable, it is not granted the flow reaches turbulent states and when it does only in few simple cases linear stability can describe the very beginning of the process of transition to turbulence. Another deficiency of the method is that it may predict stability of infinitesimal disturbances (linearly stable), while misses instabilities due to sufficiently large disturbances (nonlinearly unstable). Despite its limits, linear stability theory is a powerful tool that proved its reliability also in the description of natural phenomena and laboratory experiments. For example, there is a striking agreement between prediction of thermal convection instabilities in a fluid layer and experiments. Or the onset of the Tollmien-Schlichting waves (see Tollmien (1929) and Schlichting (1933)) in a viscous boundary layer, which have been observed experimentally in Schubauer and Skramstad (1947). Moreover people suggest that in Taylor (1923) the first rigorous confirmation of Navier-Stokes equations comes from the striking theoretical predictions of secondary flow instabilities in a rotating Couette flow.

A particular class of fluid that have been widely studied is that of steady two-dimensional flows with parallel streamlines. In this analysis a cornerstone work is Reynolds (1883) where he investigated experimentally the stability of parallel flows with or without inflection points in their profile, for both inviscid and viscous fluids. He observed that in the first case,

viscosity suppresses any instability whilst inviscid fluid show turbulence. In the second case, instabilities were readily available for any viscosity. This results are in line with Rayleigh (1880) inflection-point theorem for inviscid fluids.

The main purpose of this thesis is to investigate the impact a stabilizing density stratification has on the stability of laminar states in shear flows and transition to chaos. Stratified shear flows are a common stable structure observed in lakes, oceans, atmospheres and stars. Seasonal temperature variations regulate the density structure in lakes, whereas temperature and salinity are the key scalar fields in oceans. The density stratification of our atmosphere is due to its chemical composition and thermal interaction between its constituents and sun radiation. In stars interiors the interaction of light and particles produced by nuclear fusion with outer layers is what builds up a star density stratification. Stratified fluids are also part of our daily life, just think about pouring coffee in your glass of milk. These examples give an idea on how common and important these structures are. When these structures are perturbed by some external forces, internal waves are generated. These ubiquitous motions take many forms, and they must be used to describe phenomena ranging from the temperature fluctuations in the deep ocean to surface waves generated by wind blowing to the formation of clouds in the sheltered side of a mountain.

We consider density stratification of stabilizing effect, therefore heavier fluids lay below lighter ones. Without any external influence such stratifications are globally stable. To produce any new configuration of the fluid there must be an external energy input which counterbalance the restoring effect of buoyancy forces. In this work we consider two fluid configuration of a stratified shear flow: we consider two different shear and density profiles. In the first case we chose a simple linear density stratification which stabilizes a background shear which periodically changes direction - the so called Kolmogorov flow. It presents a number of inflection points from which instabilities comes from. This structure shows a rich variety of states before chaotic solutions appear and we will study how the transition to these states is affected by a stabilizing density gradient. The second case consider an unbounded linear shear with a number of density interfaces separating constant density layers. At each interface the layer above is lighter than the layer below, therefore the density staircase is stable. On each interface reside internal gravity waves of which propagation velocity is Doppler shifted by the background shear.

In the first case we investigate the stability of a shear flow which satisfies the necessary

condition of Rayleigh's inflection-point theorem. It is one of the few general results end exact solution of the Orr-Sommerfeld equation. It has been introduced by Kolmogorov and first studied by Meshalkin and Sinai (1961). It is a two-dimensional incompressible viscous shear flow in which the velocity has alternating directions. The linear state is of sinusoidal form $(\bar{U}, 0) \propto (\cos ny, 0)$ and is usually referred as *Kolmogorov flow*. This particular shear configuration can be realized by magnetic forces applied to an electrolyte fluid - see Bondarenko et al. (1979) and Suri et al. (2014) - or on wind driven soap films (Burgess et al. (1999)), but it also have been successfully used to describe geophysical systems (Manfroi and Young (1999)) and astrophysical systems (Garaud et al. (2015)) as well. The presence of a number of inflection points make the Kolmogorov flow readily unstable and, as have been shown by Franceschini et al. (1984), Okamoto and Shoji (1993) and Armbruster et al. (1996), it supports the formation of a number of stable states when viscosity is lowered, until it is small enough to show turbulent behaviors. Our intention is to study the effect of a stabilizing stratification on stability and dynamics of a shear flow is therefore realized by superposing a background vertical density stratification to the Kolmogorov flow. A key parameter that measures the gradients of density stratifications is the Richardson number, for which a stability criterion exist: there exist global stability if the local Richardson number is everywhere greater than or equal to on quarter. This suggest that if we consider strong enough density gradients the background Kolmogorov become stable for any viscosity. As we already mentioned, most of the attention was on unstratified realizations of the Kolmogorov flow and few works introduced stabilizing stratifications, all of them accounting for weakly stratified fluids. Here we progressively increase the density stratification, being careful to not overcome the Richardson number stability criterion. We observe an overall increase in the Reynolds number necessary to trigger instabilities and an increased number of available states in between the laminar Kolmogorov flow and chaotic states.

In the second case we study the stability of interfacial waves in a stratified shear flow where the density profile takes the form of a staircase of interfaces separating uniform layers, such as may arise from double-diffusive processes in lakes and oceans. Internal gravity waves riding on density interfaces can resonantly interact due to a background shear flow, resulting in the Taylor-Caulfield instability. The classical Kelvin-Helmholtz instability is the most well-known variety of stratified shear instability and is commonly interpreted at

the resonant interaction of waves riding on vorticity interfaces. Holmboe waves (HWI) are the next most studied type of instability, arising when a wave on a vorticity interface resonantly interacts with a gravity wave lying at a density interface Holmboe (1962). KHI and HWI are considered robust instabilities in the sense that they have been observed in natural systems and experiments.

Taylor (1931) also pointed out the possibility of a third instability in which waves riding on density interfaces could resonantly interact when their phase speeds become locked due to the Doppler-shifting effect of a background shear flow. This instability has been more elusive to observe, with the scientific community more concerned with why one might find basic states with layered density profiles in the first place. Taylor's instability was quantified and studied in more detail by Caulfield (1994), in parallel with some first laboratory experiments Caulfield et al. (1995) and nonlinear simulations Lee and Caulfield (2001). Balmforth et al. (2012) provided a comprehensive study of TCI in the long-wave limit that two density interfaces were considered as a stratified "defect" in the shear flow.

Here we explore the linear stability and nonlinear evolution of multiple TCI growing on layered density profiles. We consider a density staircase with equally spaced steps of equal size superposed on a background linear shear flow. We study normal mode solutions of the incompressible 2D Navier-Stokes and heat equations under the Boussinesq approximation. Our results show a predominance of near-neighbor interfaces TCI which are particularly strong in the limit of small bulk Richardson numbers and wavenumbers. This limit allows to consider the defect theory approximation Balmforth et al. (2012) where by a multiple scale expansion it is possible to reduce the governing equations to a Vlasov-like problem. This limit allow us to study the nonlinear evolution of internal gravity waves of large wavelength and their mixing effect.

Formulation of the problem: We consider the incompressible Navier-Stokes equations on the plane (x^*, y^*) with a gravity field $-g$ along the cross-stream direction y. To account for density variations we use conservation of energy. The Boussinesq approximation, adopted here, relies on the linear relationship between density and temperature

$$\rho(T^*) = \rho_r \left\{1 - \alpha_T (T^* - T_r)\right\}, \tag{1.1}$$

where T_r and ρ_r are reference temperature and density, α_T is the thermal expansion coefficient - typical value for fresh water at 20 is $2.1 \times 10^{-4}\mathrm{K}^{-1}$ - and the basic density profile is

given by $\rho_0(y) = \rho(T_0^*)$. The magnitude of α_T allows to neglect density variations induced by temperature, except that in the buoyancy term in the Navier-Stoke equation. Throughout this work we also neglect contributions from other sources of density stratifications as salinity. The resulting system, written under these approximation, is

$$\frac{\partial \boldsymbol{u}^*}{\partial t^*} + \boldsymbol{u}^* \cdot \nabla^* \boldsymbol{u}^* + \frac{1}{\rho_r} \nabla^* p^* = \nu^* \Delta^* \boldsymbol{u}^* - \frac{g}{\rho_r}(\rho^* - \rho_0^*)\hat{\mathbf{y}} + \mathscr{F}\hat{\mathbf{x}}, \tag{1.2}$$

$$\nabla^* \cdot \boldsymbol{u}^* = 0, \tag{1.3}$$

$$\frac{\partial \rho^*}{\partial t^*} + \boldsymbol{u}^* \cdot \nabla^* \rho^* = \kappa_T^* \Delta^* \rho^*, \tag{1.4}$$

where the star is for physical quantities. The velocity field is $\boldsymbol{u}^* = (u^*, v^*)$, p^* is the pressure scalar field, ρ^* is the density of the fluid and $\mathscr{F}$ is an external forcing acting on the fluid. The material parameters are ν^*, the kinematic viscosity, and κ_T^*, the thermal conductivity. The divergence-free condition (1.3) of the velocity field allows to introduce the streamfunction vector potential $\boldsymbol{u}^* = \nabla^* \times (-\psi^* \widehat{\mathbf{k}})$ where because of the planar nature of the fluid reduces to a scalar field. We also consider the vorticity field $\zeta^* \widehat{\mathbf{k}} = \nabla^* \times \boldsymbol{u}^*$ and taking the curl of equation (1.2), of $\boldsymbol{u}^* = \nabla^* \times (-\psi^* \widehat{\mathbf{k}})$ and expressing ψ^* in (1.4) we get

$$\frac{\partial \zeta^*}{\partial t^*} + \psi_x^* \zeta_y^* - \psi_y^* \zeta_x^* = \nu^* \Delta^* \zeta^* - g\frac{\rho_x^*}{\rho_r} - \mathscr{F}_y, \tag{1.5}$$

$$\zeta^* = \Delta^* \psi^*, \tag{1.6}$$

$$\frac{\partial \rho^*}{\partial t^*} + \psi_x^* \rho_y^* - \psi_y^* \rho_x^* = \kappa^* \Delta^* \rho^*, \tag{1.7}$$

which are the governing equations for both problems under consideration in this thesis. For each of them, in the respective chapters, we suit the specific external forcing and boundary conditions to produce the basic states we want to investigate.

Outline of the Thesis: This work is subdivided in two main parts: Chapter 2 is devoted to the analysis of the route to chaos in a stratified Kolmogorov flow; in Chapter 3 the stability properties and nonlinear dynamics of Taylor-Caulfield Instabilities in a multilayered fluid are studied. The two Chapters are related to shear instabilities in stratified fluids, they have different equilibrium states and we study different aspects of their dynamical behavior.

In Chapter 2 we consider a two-dimensional fluid exposed to Kolmogorov's forcing $\cos(ny)$ and heated from above. The stabilizing effects of temperature are taken into account using the Boussinesq approximation. The fluid with no temperature stratification has been widely studied and, although relying on strong simplifications, it is considered an important tool for the theoretical and experimental study of transition to turbulence. In this thesis we are interested in the set of transitions leading the temperature stratified fluid from the laminar solution ($U \propto \big(\cos(ny), 0\big)$, $\mathrm{T} \propto y$), to more complex states until the onset of chaotic states. We will consider Reynolds numbers $0 < Re \leq 30$, while the Richardson numbers shall be kept in the regime of weak stratifications ($Ri \leq 5 \cdot 10^{-3}$). We will first review the non-stratified Kolmogorov flow and it is the case that this prior analysis unveils few details that went unnoticed in previous works, and that will play a role in the stratified fluid counterpart: we find a new period-tripling bifurcation as the precursor of chaotic states. Introducing the stabilizing temperature gradient we shall observe that higher Re are required to trigger instabilities. More importantly we shall see new states and phenomena: the newly discovered period-tripling bifurcation is supercritical or subcritical according to Ri; more period-tripling and doubling bifurcations may depart from this new state; strong enough stratifications trigger new regions of chaotic solutions, and on the drifting solution branch, non-chaotic bursting solutions. In our analysis we consider three possible stratification: *i*) Ri=0.0001 which have negligible effects on the set of transition; *ii*) Ri=0.001 which has modest differences compared to the unstratified counterpart and *iii*) Ri=0.005 which shows appreciable departures from the bifurcation diagram of the original Kolmogorov flow.

In Chapter 3 we study the stability of interfacial waves in a stratified shear flow where the density profile takes the form of a staircase of interfaces separating uniform layers, such as may arise from double-diffusive processes in lakes and oceans. Internal gravity waves riding on density interfaces can resonantly interact due to a background linear shear flow, resulting in the Taylor-Caulfield instability. The many steps of the density profile permit a multitude of interactions between different interfaces, and a rich variety of Taylor-Caulfield instabilities. We provide a linear instability analysis for a staircase with piecewise-constant density profile, allowing for an arbitrary number of interfaces. Instability bands in the parameters' space and relative growth rates are found, elucidating the strongest and most common instabilities. We test the robustness of these results by looking at two possible generalization of the system's geometry. In one case we consider uneven thick steps and

by considering a statistical number of realization of imperfect staircases we compare the results of the linear stability analysis to the ones relative to the evenly spaced staircase. In second instance we consider finite thickness continuos interfaces where we compare the case of the classical single TCI (two sharp interfaces) to a system with two piecewise-linear interfaces. For long wavelength, weakly nonlinear structures in weakly stratified fluid, we study the onset of instability. Under these approximations, that consider the staircase as a horizontal "defect" of the density field, we derive a simplified version of the system's governing equations. The defect equations are then used tu study the onset of instability for different shapes and size of interfaces and inviscid or viscous fluids. We observe that their thickness regulates the bifurcation point and slow down the growth of instabilities, whilst strong enough viscosities play a dramatic role on the stability of internal gravity waves allowing resonance-induced instabilities as well as lone waves instabilities. Next step is to move slightly from the linear regime towards the nonlinear one, indeed we accomodate a weakly nonlinear expansion around the equilibrium state and near its bifurcation point in order to describe the dynamics of the secondary state departing from the bifurcation point. Fully nonlinear states are studied numerically in the defect approximation, testing the results of the linear stability analysis and elucidating the mutual interactions of Taylor-Caulfield billows within the layers.

Finally, in Chapter 4 we summarize the whole thesis and discuss future issues.

Chapter 2

Part I: Stratified Kolmogorov Flow

2.1 Introduction

We study the route to chaos of the Kolmogorov flow under the effect of density gradients. The Kolmogorov flow is a two-dimensional incompressible viscous flow on the torus $(x, y) = [0, 2\pi/\alpha] \times [0, 2\pi]$ driven by the streamwise monochromatic force $(n^3 \cos ny, 0)$, being α the aspect ratio of the torus. It was introduced by Kolmogorov in 1959 Arnol'd and Meshalkin (1960) as a toy-model capable to ease the mathematical difficulties of the full NS equations, but still possessing the turbulent regimes typical of the NS solutions. The non-stratified Kolmogorov problem has been extensively studied in both laminar and turbulent regimes. For flows on the domain $\mathbb{R} \times [0, 2\pi]$ the possible destabilization of the laminar solution $(U, 0) = (n \cos nz, 0)$ was studied by Meshalkin and Sinai (1961). On the contrary, when the period number and the aspect ratio are both equal to 1 ($n = \alpha = 1$), the global stability of the laminar state holds for each forcing amplitudeMarchioro (1986). When $\alpha < 1$ the stability of the secondary state has been studied by weakly non-linear methodsSivashinsky (1985); Nepomniashchii (1976). The non-linear dynamics for higher Reynolds numbers has been investigated via numerical simulationArmbruster et al. (1996); She (1987); Nicolaenko and She (1990); Platt et al. (1991) showing the emergence of complex time-dependent structures. The appearance of these states was also described by a finite dimensional dynamical systems approachFranceschini et al. (1984); Kurganskii (1980); Gambino et al. (2009); Lucas and Kerswell (2015) and by multiple-scale analysisSivashinsky (1985).

One of the features of the classical Kolmogorov model is to coalesce small scale struc-

tures to the largest scale available to the physical system. For this reason the model has been used to understand coalescence effects observed in many fields of fluid dynamics. For example, Kolmogorov's model has been applied in geophysical fluid dynamics to study the stability of finite-amplitude Rossby waves in the atmosphere Lorenz (1972) and to see whether baroclinic instabilities might cascade into easterly flows of planetary-scale Manfroi and Young (1999). The model was also reproduced in laboratory showing the effect of drag forces on the linear stability of the laminar solutionBondarenko et al. (1979) . This external effect may be removed using immiscible multilayer fluidsSuri et al. (2014) or by driven soap filmsBurgess et al. (1999). We also mention the fact that, to mimic and study the stability of zonal jets along the tropopause, the Kolmogorov flow, in a laboratory experiment, has been induced on a spherical surface Batchaev (2012).

The stratified counterpart of the Kolmogorov flow, which is the subject of our analysis, has been reproduced in laboratory experiments in the limit of weakBatchaev and Kurgansky (1986) as well strongBatchaev et al. (1984) stratifications. In the former case, experiments show the critical Reynolds number for the linear instability of the laminar flow to increase with the Richardson number; in the limit of $Ri \ll 1$, and accounting for the wall friction effects, the prediction of theory match with experimental observations. In the latter case of strong stratification, the wall friction is irrelevant for the linear stability of the laminar solution. This has been observed also by solving the eigenvalue problem of the stratified Kolmogorov model affected by a linear dragPonetti et al. (2014); Caillol (2005).

Concerning the non-stratified Kolmogorov flow, different parameters set-up have been considered: the domain aspect ratioLucas and Kerswell (2014); the inclination of the forceFranceschini et al. (1984); and its periodicityThess (1992). In the space of π-rotation invariant solutions the effect of the aspect ratio ($\alpha < 1$) on the bifurcations cascade has been studiedOkamoto and Shoji (1993). Without this symmetry restriction, in the low Reynolds number range ($Re < 30$), and fixing $\alpha = 1$ and $n = 2$, the bifurcations diagram has been constructed via symmetry group analysis, while chaotic states have been analyzed via Karhunen-Loève expansionsArmbruster et al. (1996). For fluids affected by external forcing inclined with respect to the axes and period $n > 1$, the appearance of time dependent solutions was also described in terms of finite dimensional dynamical systemsFranceschini et al. (1984). For fully developed turbulence, recurrent unstable solutions are extracted from the fluid motion in order to mimic the possible turbulent trajectories of the flowChandler and

Kerswell (2013).

On the other hand, in the density stratified Kolmogorov flow, the bifurcations leading to chaotic states have not been studied. In this chapter we shall be interested in the bifurcations that occur at low Reynolds numbers ($Re/Re_c < 21$), when the Kolmogorov flow is induced in a fluid where the stratification has a stabilizing effect: the density decreases with height. Therefore the main topic of this chapter is the set of bifurcations leading from laminar solutions toward weakly chaotic states.

We shall describe the base density profile as a linear function decreasing from the bottom to the top of the fluid. More specifically we shall fix our model to the configurationArmbruster et al. (1996) $\alpha = 1$ and $n = 2$. This model has geophysical application related to the stability of internal gravity waves with finite amplitudeKurganskii (1980) and vertical shear flowsDavis and Peltier (1976). We recall the fact that the primary bifurcation, in the limit of very weak density gradients, has been investigated using linear stability analysisBalmforth and Young (2002). Weakly non-linear theory leads to the Cahn-Hilliard equation and show the effect of the stratification as regulator of the inverse energy cascade.

The first part of the chapter is devoted to a review of the bifurcations diagram of the non-stratified flow. In the second part of the chapter we shall consider the range of Richardson numbers $Ri < 5 \cdot 10^{-3}$. Concerning the non-stratified problem we will show the presence of a period-tripling bifurcation that went unnoticed in previous works and use the Lyapunov exponents analysis to prove the chaotic nature of a further bifurcation departing from the period-tripled state. This bifurcation is a rare transition toward chaotic states in fluid dynamical systems, even though it can be found in other fields. It is a common feature in directly modulated diode lasersLamela et al. (1998); Goswami (1995) and the process of period n-tupling is a feature of the Toda oscillatorGoswami (1998). In the field of fluid dynamics it has been observed (together with period-doubling and quintupling) in Rayleigh-Bénard convectionLibchaber and Maurer (1982) and in sinusoidally varying volumetric flow induced in curved tubesHamakiotes and Berger (1990). Moreover non-linear mode interactions produce period-tripling flutters in transonic flowsBendiksen (2004). It is not clear whether a route to chaos could be driven by a period-tripling cascade as in the period-doubling *Feigenbaum* scenario. However period tripling has been observed as a 'window' in the Feigenbaum route to chaos where, for a range of the control parameters, the system reaches a periodic motion from a more chaotic stateLamela et al. (1998). Concerning

the stratified Kolmogorov flow, we shall compare the bifurcations to the non-stratified fluid scenario and analyze the new transitions allowed by introducing the temperature gradient. Beside the obvious observation that higher Reynolds numbers are required to trigger the instabilities, we shall see that, increasing the temperature gradient, a richer variety of states leads eventually to the chaotic attractors.

The outline of the chapter is as follows. In Section 2.2 we state the problem under investigation. The 2D incompressible Navier-Stokes equations and the energy conservation equation are presented; the Boussinesq approximation is introduced leading to the PDE system (2.2)-(2.3); finally the numerical algorithm we use to solve it is briefly described. In Section 2.3 we give a detailed review of the non-stratified Kolmogorov flow, elucidating the states corresponding to each bifurcation in the low Reynolds number range $Re \leq 30$ and presenting a newly observed period-tripling bifurcation. In Section 2.4 we present our numerical results and show that besides, an overall stabilizing effect, some states are stable in smaller regions of the parameters and instabilities can lead to new states as non-chaotic bursting and cascades of period-doublings and triplings.

2.2 Formulation

In this problem the background shear velocity is of sinusoidal form and is produced by the external force $\mathscr{F} = \gamma n^3 \cos(2\pi n y^*/L_y)$ which points towards the horizontal direction. Here γ is the force magnitude and n its vertical periodicity. The shear streamfunction is

$$\bar{\boldsymbol{U}}^* = \left(\frac{\gamma L_y^3}{8\pi^3}\right) \sin \frac{2\pi\, n}{L_y} y^* \tag{2.1}$$

which is usually called the Kolmogorov flow. The scalar fields are defined on the doubly periodic domain $(x^*, y^*) \in [0, L_x] \times [0, L_y]$ where $\alpha = L_y/L_x$ defines the aspect ratio. We consider the effects of a stabilizing temperature gradient: the fluid is cold (T_b) at the bottom and warm at the top (T_t), thus $\Delta_T = T_t - T_b > 0$. We assume that the basic temperature gradient over the length L_y is given by the linear interpolation $T_0^*(y) = T_b + \Delta T\, y/L_y$ and perturbations from the basic state are $T^*(x, y, t) = T_0^*(y) + \Delta T\, \theta(x, y, t)/2\pi$.

Equations (1.5)-(1.7) are nondimensionalized using $L_y/2\pi$ as lengthscale, $2\pi\nu/\gamma L_y$ as

timescale, $\gamma L_y^3/8\pi^3\nu$ as reference streamfunction and $\Delta T/2\pi$ as scale temperature, giving

$$\frac{\partial \zeta}{\partial t} + Re\,(\Psi_x Z_y - \Psi_y Z_x) = \Delta\zeta + RiRe\,\theta_x, \zeta = \Delta\psi, \tag{2.2}$$

$$\frac{\partial \theta}{\partial t} + Re\,(\Psi_x \theta_y + \Psi_y \theta_x) = \frac{\Delta\theta}{Pr} + Re\,\psi_x, \tag{2.3}$$

where $\Psi(x,y,t) = \sin ny + \psi(x,y,t)$, being $\psi(x,y,t)$ the deviation of the streamfunction from the laminar state and $\theta(x,y,t)$ the deviation of the temperature from the stabilizing profile. The nondimensional parameters

$$Re = \frac{\nu}{\gamma}\left(\frac{L_y}{2\pi}\right)^2, \quad Ri = \frac{g\beta\Delta T}{2\pi}\left(\frac{\nu}{\gamma}\right)^2\left(\frac{2\pi}{L_y}\right)^3, \quad Pr = \frac{\nu}{\kappa_T}, \tag{2.4}$$

are respectively the Reynolds number, the Richardson number and the Prandtl number. Here we followArmbruster et al. (1996) and fix the period of the external force $n = 2$ and choose the aspect ratio $\alpha = 1$. To avoid formation of thermal boundary layerBalmforth and Young (2002), we state the Prandtl number to be 1.

The above system is characterized by the symmetry

$$\mathscr{S} : (x, y, \psi, \theta) \to (-x, -y + \pi/n, \psi, -\theta), \tag{2.5}$$

which represents the combination of a reflection in the (x,y)-plane with the vertical shift of half of the wavelength of the forcing function. Other symmetries are a rotation of π in the (y,ψ,θ)-plane

$$\mathscr{R} : (x, y, \psi, \theta) \to (x, -y, -\psi, -\theta), \tag{2.6}$$

a discrete shift of $2\pi/n$ along y

$$t_n : (x, y, \psi, \theta) \to (x, y + 2\pi/n, \psi, \theta), \tag{2.7}$$

and the continuous horizontal shift:

$$\mathscr{T}_l : (x, y, \psi, \theta) \to (x + l, y, \psi, \theta). \tag{2.8}$$

The set of bifurcations of the non-stratified Kolmogorov flow has been shownArmbruster et al. (1996) to be the breaking of these symmetries.

2.2.1 Numerical methods

In this section we present the numerical methods used throughout this work to solve our model system.The core of these algorithms lies in the computation of (8)-(9) with a dealiased

Fourier-Fourier pseudospectral code. In this work the bifurcation parameter is the Reynolds number, whilst the Richardson number is kept fixed to some particular values ($Ri = 0$, 10^{-4}, 0.001, 0.005). For relatively high Re (typical Re larger that 21) chaotic solutions will arise 1,19 and we shall detect transitions to chaos by computing the Lyapunov exponents. In the next paragraph we present the pseudospectral code that solves the governing equations and in the consecutive one we present the algorithm that extracts the Lyapunov exponents.

Pseudospectral Algorithm

We solve numerically Eqs.(2.2)-(2.3) with a fully dealiased pseudospectral code with a second-order semi-implicit time integrator. The spatial discretization is based on a Fourier-Galerkin spectral expansion

$$\psi(x,y,t) = \sum_{j=-N_x/2+1}^{N_x/2} \sum_{l=-N_y/2+1}^{N_y/2} \widehat{\psi}_{j,l}(t) e^{i(\alpha j x + l y)} \tag{2.9}$$

$$\theta(x,y,t) = \sum_{j=-N_x/2+1}^{N_x/2} \sum_{l=-N_y/2+1}^{N_y/2} \widehat{\theta}_{j,l}(t) e^{i(\alpha j x/ + l y)} \tag{2.10}$$

with resolution $N_x \times N_y$ which is dealiased via the two-thirds rule. Time-integration is based on a second-order Runge-Kutta algorithm where the discretization of the linear part is of the Crank-Nicolson type:

$$\widehat{\psi}^1_{j,l} = -\left[-\boldsymbol{k}^2 \widehat{\psi}^n_{j,l} + dt\left(\frac{\boldsymbol{k}^4}{2}\widehat{\psi}^n_{j,l} + Re\,\widehat{J}^n_{j,l}(\Psi,\Delta\Psi) - i\alpha j Ri Re \widehat{\theta}^n_{j,l}\right)\right] \Big/ \left(1 + \frac{dt}{2}\boldsymbol{k}^2\right)\boldsymbol{k}^2, \tag{2.11}$$

$$\widehat{\theta}^1_{j,l} = \left[\widehat{\theta}^n_{j,l} + dt\left(-\frac{\boldsymbol{k}^2}{2Pr}\widehat{\theta}^n_{j,l} + Re\,\widehat{J}^n_{j,l}(\Psi,\theta) + i\alpha j Re \widehat{\psi}^n_{j,l}\right)\right] \Big/ \left(1 + \frac{dt}{2Pr}\boldsymbol{k}^2\right)\boldsymbol{k}^2, \tag{2.12}$$

$$\begin{aligned}\widehat{\psi}^{n+1}_{j,l} = -\Bigg[&-\boldsymbol{k}^2\widehat{\psi}^n_{j,l} + \frac{dt}{2}\Big(\boldsymbol{k}^4\widehat{\psi}^n_{j,l} + Re\,\widehat{J}^n_{j,l}(\Psi,\Delta\Psi) + Re\,\widehat{J}^1_{j,l}(\Psi,\Delta\Psi) \\ &-i\alpha j Ri Re\widehat{\theta}^n_{j,l} - i\alpha j Ri Re\widehat{\theta}^1_{j,l}\Big)\Bigg] \Big/ \left(1 + \frac{dt}{2}\boldsymbol{k}^2\right)\boldsymbol{k}^2,\end{aligned} \tag{2.13}$$

$$\begin{aligned}\widehat{\theta}^{n+1}_{j,l} = \Bigg[&\widehat{\theta}^n_{j,l} + \frac{dt}{2}\left(-\frac{\boldsymbol{k}^2}{Pr}\widehat{\theta}^n_{j,l} + Re\,\widehat{J}^n_{j,l}(\Psi,\theta) + Re\,\widehat{J}^1_{j,l}(\Psi,\theta)\right. \\ &\left. + i\alpha j Re\widehat{\psi}^n_{j,l} + i\alpha j Re\widehat{\psi}^1_{j,l}\right)\Bigg] \Big/ \left(1 + \frac{dt}{2Pr}\boldsymbol{k}^2\right)\boldsymbol{k}^2,\end{aligned} \tag{2.14}$$

where $\widehat{J}_{j,l}(a,b) = \texttt{fft}\left[J(a,b)\right]_{j,l}$ and the superscript indicate the nth time-step. The wave-vector is $\boldsymbol{k} = (\alpha j, l)$ and the Fourier modes are such that $\widehat{\psi}_{0,0} = 0$ and the Hermitian

condition $\widehat{\psi}_{-j,-l} = \widehat{\psi}^*_{j,l}$ holds true. The number of effective degree of freedom is therefore $N_y(2N_x - 1) + 2$. Typically the grid is $N_x = N_y = 64$. We have checked that our results are grid independent.

We shall construct the bifurcation diagram using the L^2-norm of the streamfunction ψ and temperature θ which are given by

$$\|\psi\|_2^2 = \sum_{j=-N_x/2+1}^{N_x/2} \sum_{l=-N_y/2+1}^{N_y/2} |\widehat{\psi}_{j,l}|^2, \qquad \|\theta\|_2^2 = \sum_{j=-N_x/2+1}^{N_x/2} \sum_{l=-N_y/2+1}^{N_y/2} |\widehat{\theta}_{j,l}|^2. \tag{2.15}$$

Defining X as

$$\boldsymbol{X} = \begin{bmatrix} \widehat{\psi} \\ \widehat{\theta} \end{bmatrix} \tag{2.16}$$

its L^2-norm is given by $\|X\|_2^2 = \|\psi\|_2^2 + \|\theta\|_2^2$.

Chaos diagnostic

When we study chaotic motions it is useful to find quantities that can measure it, and an effective diagnostic for chaotic systems is the study of the sign of Lyapunov exponents. The idea is to consider a trajectory of the solution of a dynamical system, perturb it of an infinitesimal amount and measure in time how this perturbation evolve. It is in the definition of chaotic states that infinitely near trajectories diverge eventually, therefore we measure the growth or decay of these small perturbations. Given an initial value X_0 in the phase space its evolution is given by $X_{n+1} = f(X_n)$. If the vector $\delta X_n^{(j)}$ is a small perturbation from X_n in the j-th direction we find that

$$\delta X_n^{(j)} = Df_{X_{n-1}} \delta X_{n-1}^{(j)} = Df_{X_0}^n \delta X_0^{(j)}. \tag{2.17}$$

This is the vector we keep measure of and defines the Lyapunov exponents spectrum $\{\lambda_1, \lambda_2, \ldots, \lambda_m\}$, where $\lambda_1 \geq \lambda_2 \geq \cdots \geq \lambda_m$ and

$$\pm\lambda_j = \lim_{n\to\pm\infty} \frac{1}{|n|} \log \|Df_{X_0}^n \delta X_0^{(j)}\|. \tag{2.18}$$

The associated perturbation vector in X_n, $\delta X_n^{(j)}$, is the Lyapunov vector which point towards the direction j where the perturbation grows at a λ_j rate.

The algorithm to extract these valuesWolf et al. (1985) takes a post-transient initial condition X_0 and a ball of initial perturbations $\delta X_0^{(j)}$ and evolves the former by using the pseudospectral code we presented in the previous paragraph and the latter using their linearized instance.

2.3 Kolmogorov Flow

The non-stratified Kolmogorov flow is an important model that has been used to investigate transition and turbulent phenomena in the Navier-Stokes equations. In this Section, following the work of Armbruster et al.Armbruster et al. (1996), we shall characterize the sequence of bifurcations that, starting from the destabilization of the equilibrium, leads to weak turbulence.

2.3.1 Main states and routes to chaos

The solutions of the Kolmogorov flow for $Re \leq 30$ are schematically reported in Fig.2.1 where we show their bifurcation diagram. We control the solutions by the Reynolds number and track them by $\|\psi\|_2$. For graphical purposes, when ψ is time dependent, we report a suitable time average of $\|\psi\|_2$. In Fig. 2.1 one can recognize the following main states:

1. for $Re < 5/\sqrt{6}$ a sinusoidal shear velocity profile, commonly referred to as the *Kolmogorov flow*, with the same shape of the external force;

2. above this threshold it appears a stationary pattern (denoted, in Fig.2.1, with a solid black line) consisting of dipoles, i.e. two couples of counter-rotating vortices;

3. this state bifurcates to dipoles drifting along the horizontal direction denoted, in Fig.2.1, with ■;

4. then a hysteretic bifurcation leads to steady states denoted, in Fig.2.1, with the solid black line between the points S1 and S2; the oscillatory states that follows, are denoted with ∘. For higher Re two branches develop:

5. the upper branch is characterized by a drifting and oscillating solution (denoted, in panel c) of Fig.2.1, with the ■ between the points D3 and D4) that eventually becomes chaotic;

6. the lower branch begins with solutions (denoted, in panel c) of Fig.2.1, with the ▽ between the points S4 and S5) that translate vertically while pulsating, and that, for high Reynolds numbers, become chaotic.

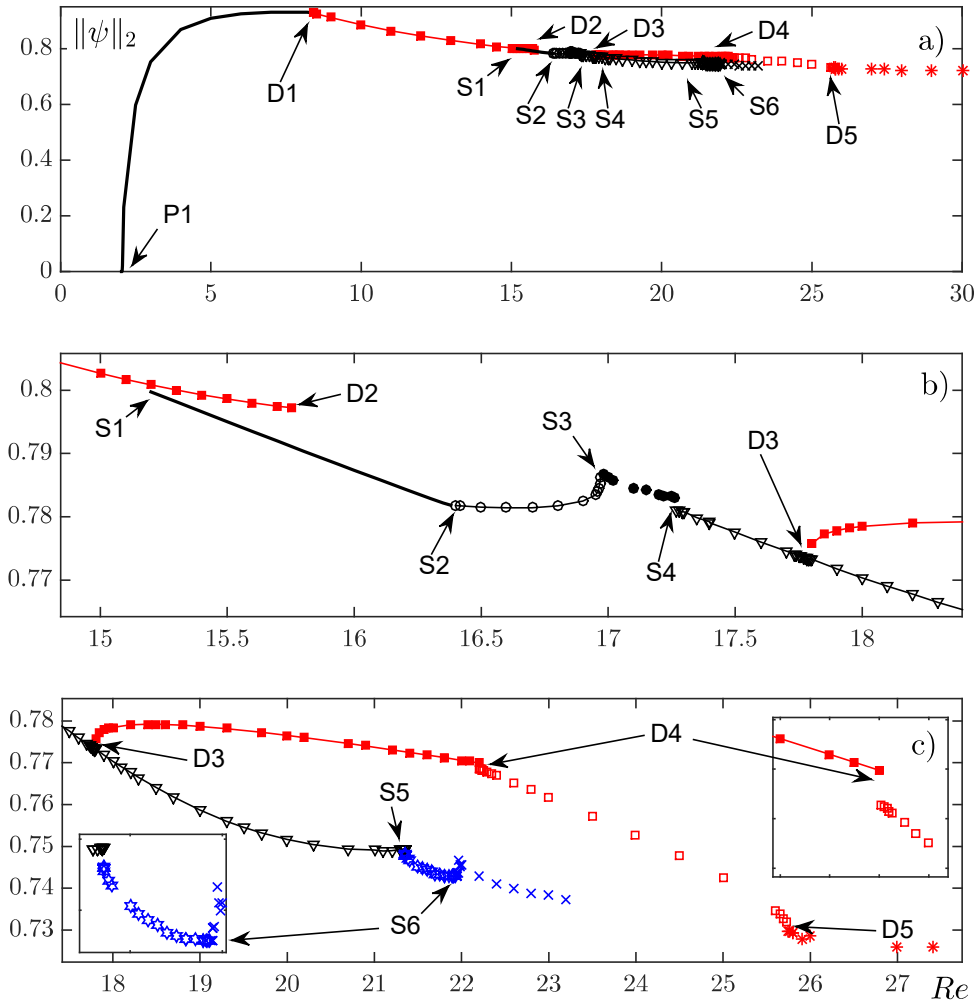

Figure 2.1: In panel a) the full bifurcation diagram for the non-stratified Kolmogorov. In the horizontal axes the Reynolds number while in the vertical axes we report the L^2-norm of the stream function. Panels b) and c) are magnification of relevant parts of the bifurcation diagram. The solid black line is the steady state solution departing from the primary bifurcation of the laminar state and for the solution appearing through hysteresis from the drifting state in $S1$. (■) is for the first and second drifting state and (□) is an oscillatory drifting state which become chaotic through intermittency ($*$). ($\circ$) is for the Hopf bifurcation of the steady state and ($\bullet$) for the gluing process of the Hopf solutions. ($\triangledown$) stands for stable glued states. ($\star$) is the period-tripled state and ($\times$) is its chaotic bifurcation.

Here we also mention that we have found one of the oscillatory states to undergo a period-tripling bifurcation. This is a transition which went unnoticed in previous works and that will be analyzed in more detail in the next subsection.

The fluid reaches chaotic regimes following two different routes: The first departs from steady state solutions (in panel b of Fig.2.1 these states correspond to the points between $S1$ and $S2$). The second departs from the horizontally drifting states that, in Fig.2.1, are denoted with ■. The latter route is characterized by the features typical of the *Pomeau-Manneville* scenario, where transition to chaos is due to intermittency. In this case the final chaotic states have been analyzedInubushi et al. (2012) through the computation of the Lyapunov exponents.

The route to chaos departing from the steady states, on the other hand, has not been extensively studied. A previous workArmbruster et al. (1996) shows that symmetries in the governing equation allow four steady state solutions. These undergo four simultaneous Hopf bifurcations (the point S2 in Fig.2.1) and the resulting oscillatory solution has null mean velocity, in both vertical and horizontal directions. At larger Re this limit cycles merge through the so called *gluing bifurcation*, that occurs between S3 and S4. The physical behavior of the fluid during this process is a vertical and horizontal motion which switches randomly its direction (see Fig. 2.2). Raising the Re, this random switching disappears and the system stabilizes to a periodic oscillation with a bulk vertical drift (both upward and downward motions solutions are allowed) and null horizontal mean velocity. Finally, this state loses its stability. The further dynamics for higher Re has not been investigated in literature. In this work we shall refine the analysis of this branch and we shall see how limit cycles undergo a *period-tripling* bifurcation after which the system becomes chaotic. This will be seen via the Lyapunov exponents analysis.

2.3.2 Details on the transitions

This subsection is devoted to a more detailed explanation of the set of transitions presented in Fig.2.1. On a horizontally unbounded domain ($\alpha = 0$), the Kolmogorov flow loses its stability at $Re_c^{unb} = \sqrt{2}$ which is a result proved by continued fractionsMeshalkin and Sinai (1961). In this chapter we focus our attention to the aspect ratio $\alpha = 1$ and forcing period $n = 2$. In this case, through Galerkin projection, a 5-dimensional dynamical system has been derivedArmbruster et al. (1996), whose linear stability analysis shows the bifurcation

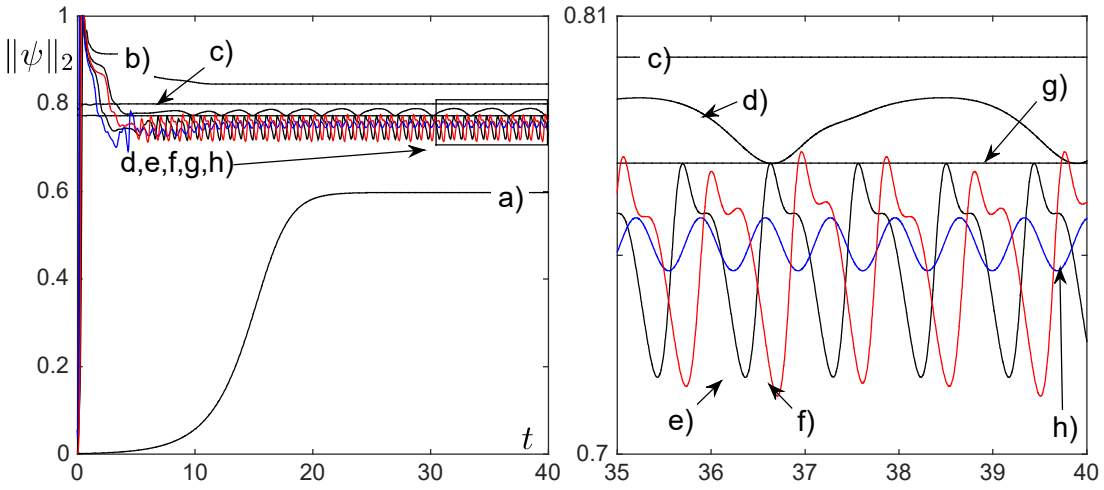

Figure 2.2: Time evolution of $\|\psi\|_2$ for any stable state of the Kolmogorov flow when $Re < 30$. The labels are associated to: a) first steady state at $Re = 2.5$; b) first drifting state $Re = 12$; c) second steady state $Re = 15.4$; d) periodic orbit $Re = 16.95$; e) glued periodic orbit $Re = 21$; f) period-tripled state $Re = 21.3557$; g) second drifting state $Re = 21.2$; h) oscillating drifting state $Re = 24$.

parameter to rise to $Re_c = 5/\sqrt{6}$. We name this point $P1$ (not shown in the Figure) and indicate its corresponding parameter value by $Re(P1, Ri = 0) = 5/\sqrt{6}$. Above this value the laminar state $\Psi_0 = \sin ny$ bifurcates towards a steady pattern of vortices (see Fig.2.3): along the horizontal direction there is a couple of vortices with positive and negative vorticity, a *dipole*; along the vertical direction there are two dipoles (we recall that the external forcing is doubly-periodic). Curve a) of Fig.2.2 shows the time evolution of the L^2-norm $\|\psi\|_2$ of a random perturbation of Ψ_0 when $Re = 2.5$. Solutions belonging to this branch have the $\mathscr{T}_\pi \mathscr{S}\psi(x, y, t) := \psi(-x + \pi, -y + \pi/n, t) = \psi(x, y, t)$, $\mathscr{T}_\pi \mathscr{R}\psi(x, y, t) := -\psi(x + \pi, -y, t) = \psi(x, y, t)$ and $t_2\psi(x, y, t) := -\psi(x, y + \pi, t) = \psi(x, y, t)$ symmetries. When the Reynolds number increases, the dipoles lose their broad horizontal structure and in $D1$, at a parameter value of $Re(D1, 0) = 8.3$, they bifurcate to a stable drifting state. The solution loses its symmetries $\mathscr{S}$ and t_2, allowing four horizontal drifting statesArmbruster et al. (1996), which involve modes with time-depending amplitude as shown in panel d) of Fig.2.4. Two waves come from the action of $\mathscr{S}$ and two from t_2. In panels a)-c) we see three snapshots of the solution, taken during a period of translation. In panel e) we keep track of the horizontal position of the extrema of the vorticity, and one can see how they drift to the left as time

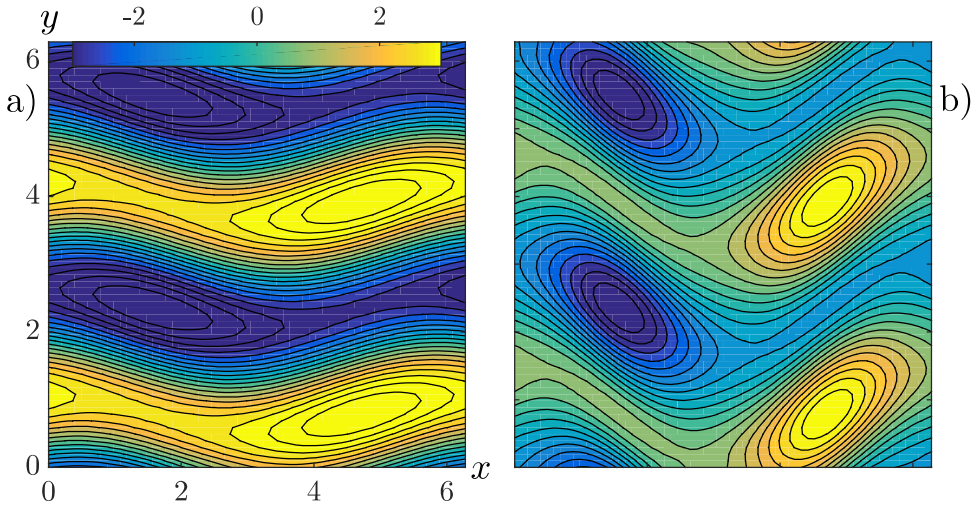

Figure 2.3: Vorticity field $\zeta(x, y)$ of the stable steady state when $5/\sqrt{6} < Re < 8.3$: in a) $Re = 2.5$ and in b) $Re = 8.2$.

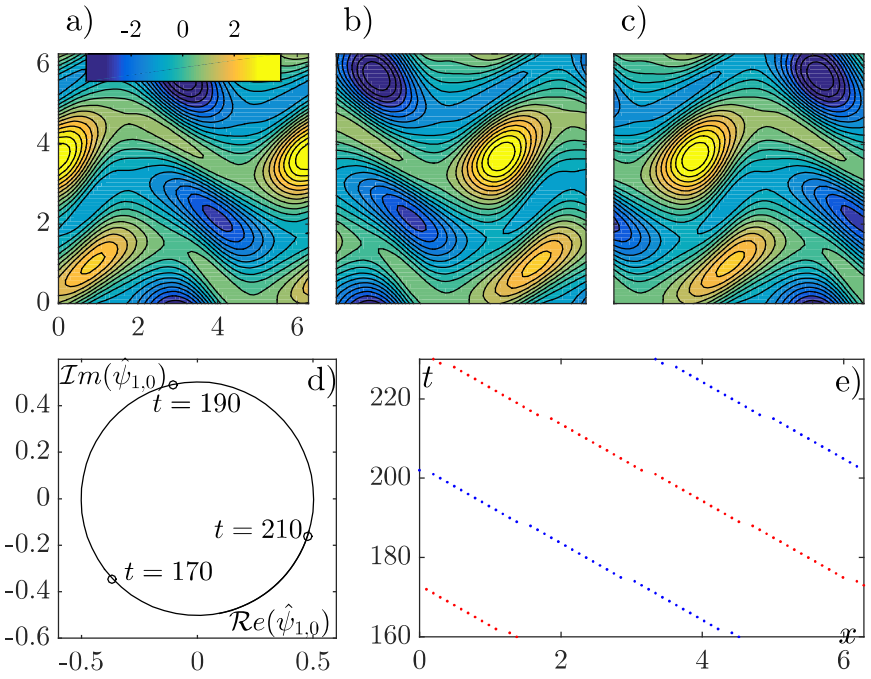

Figure 2.4: Drifting solution at $Re = 12$. In the three top panels there are snapshots taken over a drifting period of the vorticity: $t = 170$, 190, 210. Phase portrait of mode $\boldsymbol{k} = (1, 0)$ is in d) where the axes are the real and imaginary component. In e) there is the time-evolution of the horizontal maximum (red dots) and minimum (blue dots) of the vorticity. In this solution vortices move from right to left.

increases. In panel d) we can see the phase portrait of the horizontal mode (1,0) together with the points where the snapshots have been taken. From curve b) of Fig.2.2 we observe the L^2-norm of ψ to be, after a transient, constant in time (the curve refers to $Re = 12$). The time dependent behavior of the modes is not observed in the norm since the modulus of the real and imaginary part of each mode sum up to a constant.

The drifting state loses its stability at $Re(D2, 0) = 15.8$, and the system shows a hysteretic transition toward a steady solution. This state becomes stable at $Re(S1, 0) = 15.2$ where the shift-and0reflect symmetry has been restored and the rotation symmetry $\mathscr{R}$ has been broken allowing four stationary solutions to coexistArmbruster et al. (1996) (coming from the action of $\mathscr{R}$ and t_2). These states, at $Re(S2, 0) = 16.4$, show a simultaneous Hopf bifurcation toward periodic orbits which are shown in panel a) of Fig.2.5. These oscillations corresponds, in the physical space, to localized oscillations of the dipoles with a null mean drift velocity; also in d) of Fig.2.2 one can see periodic oscillations of the L^2-norm of ψ.

When $16.96 < Re < 17.3$ (in Fig.2.1, between $S3$ and $S4$), the solution switches randomly between these orbits as shown in Fig.2.6. The merging of the orbits has not stabilized (as for $Re > 17.3$), thus in the physical space we observe vortices drifting back and forth in the vertical direction, as we can infer from the trajectories in panel a) and d) of Fig.2.6. The phase portrait of the horizontal mode $(1, 0)$ is shown in panel d) and the oscillating horizontal drifting motion of the physical solution can be inferred by the position of the extrema in panel f).

When, after $S4$, the merging becomes stable, the Kolmogorov flow keeps only the vortex oscillations and loses the horizontal drift. This state is stable until $Re(S5, 0) = 21.35$, but in $D3$, at $Re(D3, 0) = 17.8$, one can observe the appearance of coexisting stable drifting states.

These states preserve the same symmetries and properties as before $D2$. Afterwards, at $Re(D4, 0) = 22$, the four traveling solutions bifurcate simultaneously to a drift-and-oscillate state. In Fig.2.2 we plot the L^2-norm of the streamfunction for the drifting and drift-and-oscillate solutions when $Re = 21.2$ and 24, labelled as g) and h) respectively. When $Re > 25.7$, after $D5$, the flow becomes chaotic via intermittent bursts between unstable recurrent motions. In this regime the intermittent bursts shown in Fig.2.7 are trajectories passing nearby four unstable limit cycles. This regime has been proved to be chaoticInubushi et al. (2012) via Lyapunov exponents analysis.

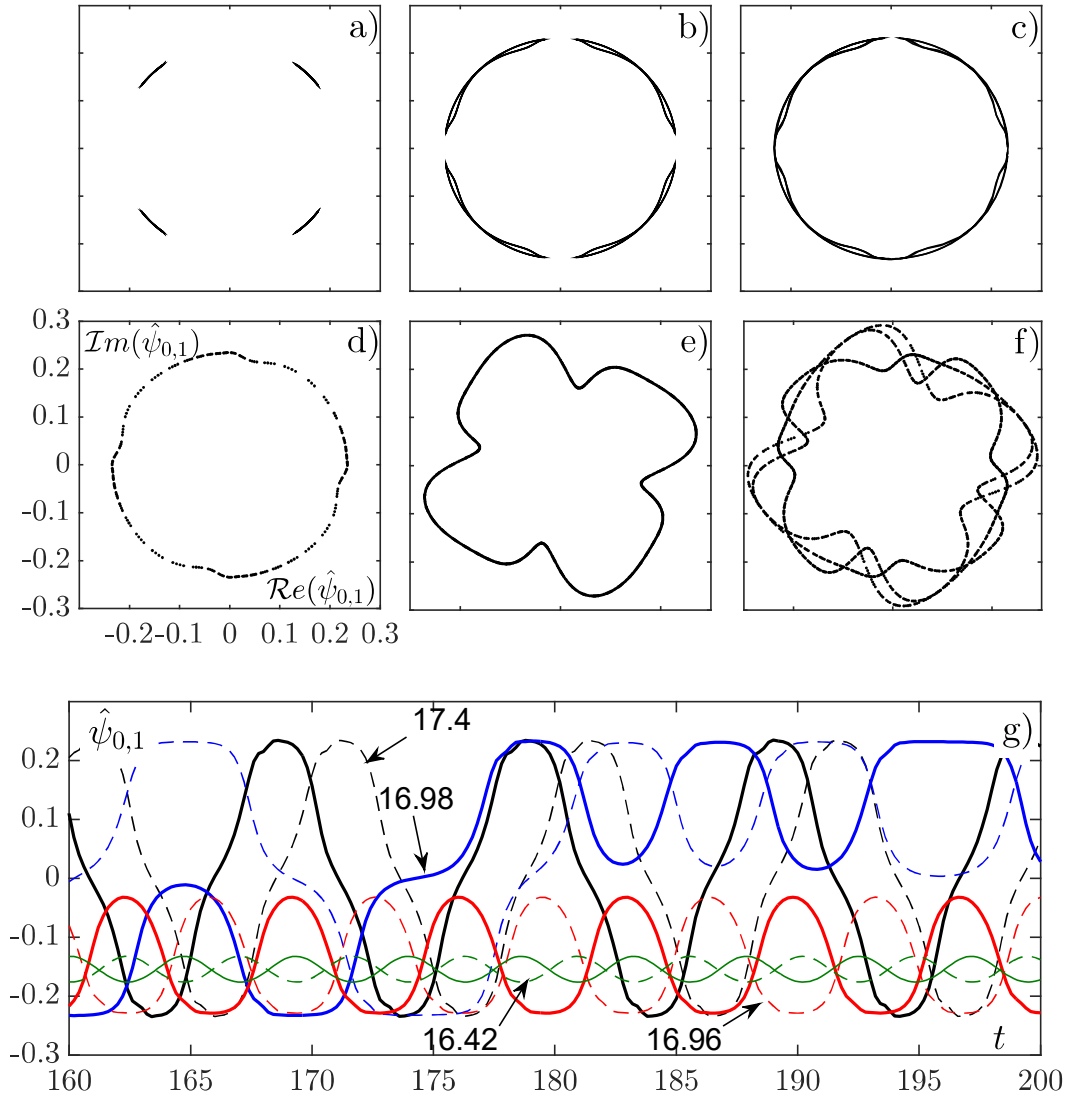

Figure 2.5: Phase portraits and trajectories of $\left(\mathcal{R}e(\widehat{\psi}_{0,1}), \mathcal{I}m(\widehat{\psi}_{0,1})\right)$ on the branch with horizontally steady solutions. From (a) to (f) the Reynolds number is Re=16.42, 16.96, 16.98, 17.4, 21.3, 21.8. The panel (g) represents the time evolutions of the same modes when Re=16.42, 16.96, 16.98, 17.4.

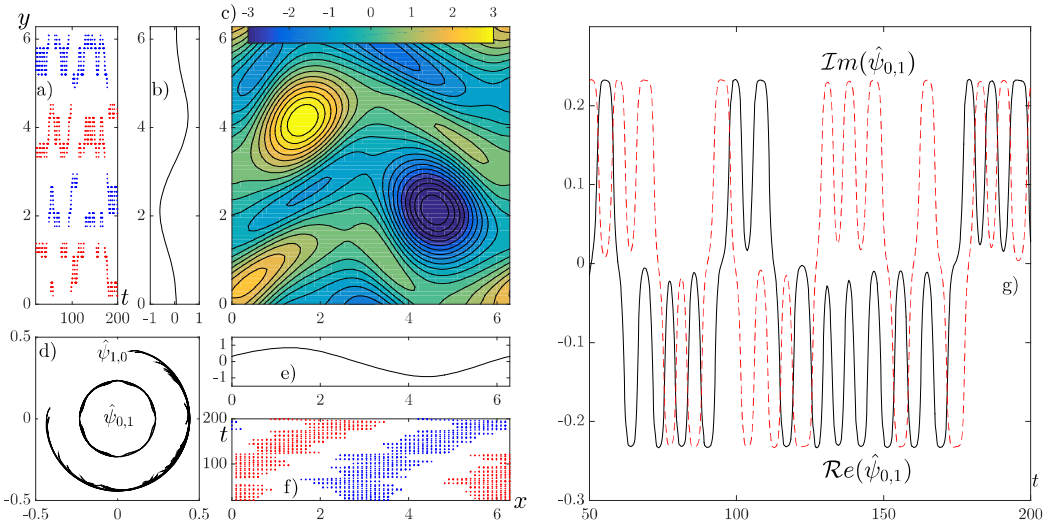

Figure 2.6: Snapshot of the vorticity when $Re = 16.98$ and $t = 50$ in panel c). Horizontal and vertical average of the vorticity are in e) and b) and the position of their extrema as function of time (red dots for the maximum and blue dots for the minimum) are in f) and a). The phase plot in panel d) is given by the real and imaginary part of $\widehat{\psi}_{(0,1)}$ and in panel g) there are the trajectories of the real (black) and imaginary (red) part of $\widehat{\psi}_{(0,1)}$.

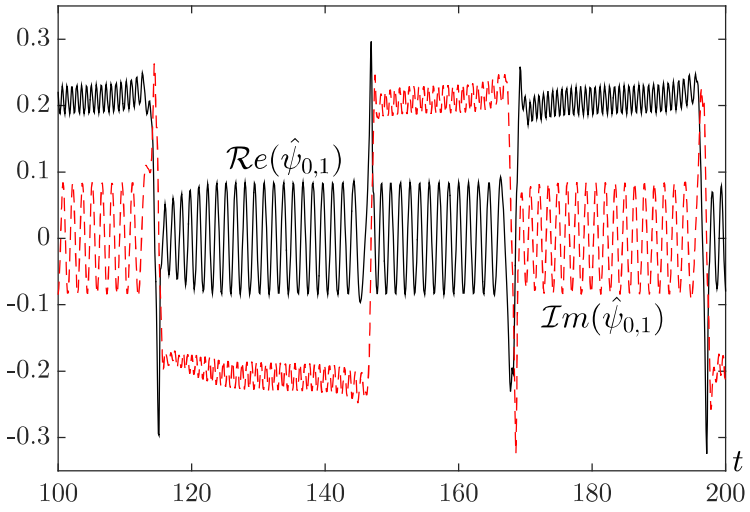

Figure 2.7: Time evolution of the real (black) and imaginary (red) part of $\widehat{\psi}_{0,1}$ during the intermittent bursts at $Re = 25.8$.

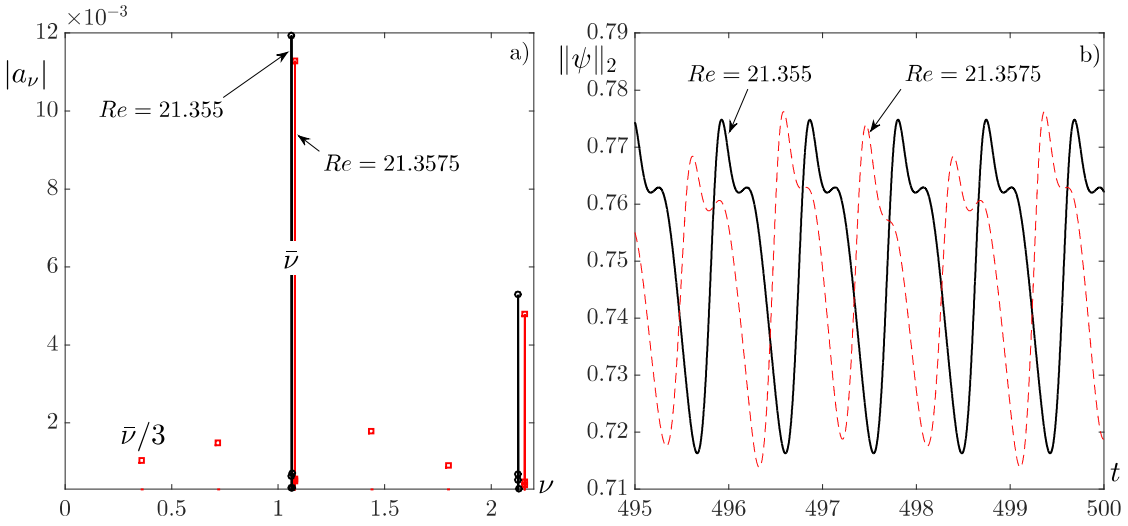

Figure 2.8: In panel a) is shown the modulus of Fourier coefficients a_ν for $\|\psi\|_2$. Black circles are for $Re = 21.355$ and red squares for $Re = 21.3575$ which are slightly before and after the period-tripling bifurcation. In panel b) there are the L^2-norms for the two Re as function of time.

When the glued state loses its stability in $S5$ a bifurcation, which was left unnoticed in the previous literature, appears: it is a period-tripling of the earlier glued state. In panel f) of Fig.2.5 the period-tripling of the phase portrait is evident. In Fig.2.8, panel b), we can see $\|\psi\|_2$ for $Re = 21.355$, and its period-tripled state for $Re = 21.3575$. The period-tripling is also evident by the time-frequency analysis of the norm reported in panel a) of Fig.2.8. The black circles are for $Re < Re(S5, 0)$ and they show the fundamental frequency to be $\bar{\nu} = 1.063$. Above $Re(S5, 0)$ the time spectrum is denoted by red squares: the presence of the frequency $\bar{\nu}/3$ implies the appearance of a period-tripled trajectory.

On the right of Fig.2.9 we report the oscillation period T of all the periodic states. Notice the presence of a gap in the region between $S3$ and $S4$ (i.e. for $16.96 \leq Re \leq 17.3$) because of the random switching related to the gluing bifurcation. Moreover, at $Re(S5, 0) = 21.35$, one can see the jump related to period-tripling.

Finally when the period-tripled state loses its stability, the system settles to a chaotic regime. We have used standard techniquesInubushi et al. (2012); Wolf et al. (1985) to compute the Lyapunov exponents on this branch and in panel a) of Fig.2.9 we show the three largest exponents for Re across S6. We see that after $Re = 15.53\sqrt{2}$ one of the exponents becomes positive indicating the solution to be chaotic.

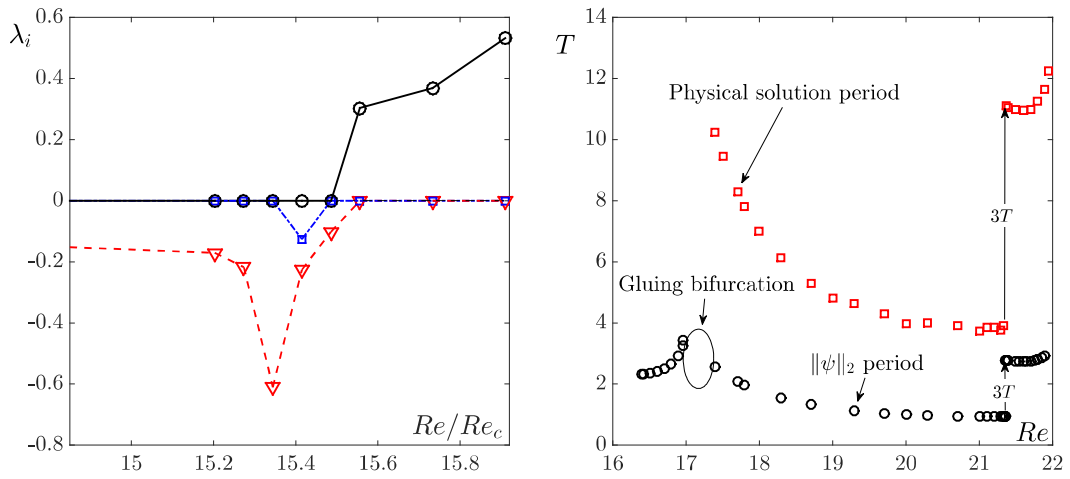

Figure 2.9: Left panel reports the evolution of the Lyapunov exponents $\lambda_1 > \lambda_2 > \lambda_3 > \dots$ as function of Re/Re_c, where $Re_c = \sqrt{2}$. In right panel there is the oscillation period $T(Re)$ for horizontally steady solutions. We compute it from $\|\psi\|_2$ ($\circ$) and from the physical solution ($\square$).

In the next section we shall introduce the stabilizing linear temperature stratification and compare the scenario presented in this Section to the new phenomenologies triggered (or dumped) by temperature variation.

2.4 Weakly stratified Kolmogorov flow

In the previous Section we have reviewed the set of transitions leading the Kolmogorov flow to chaotic states. In the present Section we shall introduce a temperature gradient across the vertical y direction. We shall see that the introduction of stratification leads to the appearance of a variety of states not present in the non-stratified fluid. We shall present our results, first fixing the value of Ri and then investigating the dynamics of the transitions for $0 < Re < 30$. In this chapter we shall give a detailed account only for values of $0 < Ri \leq 5 \cdot 10^{-3}$. In fact, for $Ri = 10^{-2}$ or higher, a preliminary investigation has revealed the emergence of completely new dynamic behaviors with characteristics that makes it difficult the comparison with the non-stratified Kolmogorov flow. We believe that the case when $Ri > 0.005$ deserves a separate analysis that will appear elsewhere.

When the stratification values are $Ri \leq 10^{-4}$, our analysis has revealed no significant change with respect to the case $Ri = 0$. In fact, when $Ri \leq 10^{-4}$, the presence of the

temperature gradient does not change neither the bifurcation points nor the qualitative characteristics of the states that we have seen for the non-stratified fluid; the effect of the stratification reveals itself only from the fact that some of the bifurcation points are slightly shifted in the Reynolds number. To be more precise: the bifurcation points $P1$, $D1$, $D2$ and $S1$, appearing in the bifurcation diagram at low Re, remain the same (or at least is not easily detectable) while the bifurcation points appearing for larger Re are slightly shifted. In Table 2.1 the bifurcation points of the non-stratified and the stratified flows are compared. For $Ri \leq 10^{-4}$ one can see that the bifurcation points are very similar: the most relevant

Table 2.1: Bifurcation points of the non-stratified and stratified ($Ri = 10^{-4}$, 10^{-3} and $5 \cdot 10^{-3}$) Kolmogorov flow.

	$Ri = 0$	$Ri = 10^{-4}$	$Ri = 10^{-3}$	$Ri = 5 \cdot 10^{-3}$
P1	$5/\sqrt{6}$	=	2.055 ± 0.005	2.058 ± 0.005
D1	8.3	=	8.43 ± 0.03	8.85 ± 0.05
D2	15.8	=	15.35 ± 0.05	13.65 ± 0.05
D3	17.8	17.87 ± 0.02	18.45 ± 0.05	21.1915 ± 0.0005
D4	22	21.9 ± 0.1	22.03 ± 0.03	23.85 ± 0.05
D5	25.7	25.68 ± 0.01	25.055 ± 0.005	25.155 ± 0.005
S1	15.2	=	14.7 ± 0.1	13.55 ± 0.05
S2	16.4	16.32 ± 0.02	15.95 ± 0.05	14.15 ± 0.05
S3	16.96	16.91 ± 0.01	16.49 ± 0.01	//
S4	17.3	17.25 ± 0.05	17.31 ± 0.01	14.743 ± 0.003
$S4_c$	//	//	//	15.33 ± 0.01
$S4_c'$	//	//	//	19.13 ± 0.03
$S4'$	//	//	22.3995 ± 0.0005	21.67 ± 0.03
$S4''$	//	//	//	23.71 ± 0.01
S5	21.35	21.43 ± 0.01	21.9555 ± 0.0005	24.4045 ± 0.0005
$S6'$	//	//	22.2835 ± 0.0005	24.623 ± 0.003
$S6''$	//	//	22.3245 ± 0.0005	24.658 ± 0.002
$S6'''$	//	//	22.3335 ± 0.0005	24.6665 ± 0.0005
S6	21.925	21.985 ± 0.005	22.3365 ± 0.0005	24.6685 ± 0.0005

feature is the overall tendency of the temperature gradient to reduce the range of values in which the horizontal drift solutions exist and to broaden the parameter region where the non-horizontal drifting solutions (steady, oscillating, gluing-oscillating and period-tripled states) exist.

On the contrary, when $Ri = 10^{-3}$, we shall observe new transitions and new interesting phenomena; this will be the subject of the next Subsection.

2.4.1 $Ri = 0.001$

When we induce a temperature stratification such that $Ri = 10^{-3}$, the route to chaos is modified by the appearance of new states. From Fig.2.10 we see that the overall structure of the bifurcations and the states typical of the non-stratified Kolmogorov flow are left unchanged; however we shall see how the route to chaos departing from the steady solution has now a more complex structure. In Table 2.1 we report the bifurcation points we have found solving the Kolmogorov flow at different Ri, including $Ri = 0$ which is the non-stratified case. As we expect from the stabilizing nature of the temperature gradient, the laminar state bifurcates for Re larger than $5/\sqrt{6}$ and the newly formed steady state (see Fig.2.11) has the same structure that we have seen at the right of Fig.2.3 for the non-stratified fluid: two superposed dipoles along the vertical direction. The right panel of Fig.2.11 shows the temperature variations from the linear temperature gradient. The highest and lowest temperature deviations appear to be concentrated in the circulating region between the vortices.

2.4.2 The drifting states for $Ri = 0.001$

The steady state loses its stability for a Re which is higher compared to the non-stratified fluid (i.e. $Re(D1, 10^{-3}) > Re(D1, 0)$). From $D1$ the drifting state branch departs. As for the non-stratified fluid, the drifting solution loses its symmetries $\mathscr{S}$ and t_2 allowing four states. The main structure of the horizontal drift is due to the modes $\boldsymbol{k} = (1, 0)$ and $(-1, 0)$. In panel a) of Fig.2.12 we show the phase portrait of $\widehat{\psi}_{(1,0)}$ and $\widehat{\theta}_{(1,0)}$ with their real and imaginary part on the axes. We can see the circular motion of the components around the origin which allows the drifting behavior. This motion is confirmed by panel b) and c) where, for $Re = 12$, we show the position in time of the extrema of the vorticity and of the temperature scalar field. We recall that the non-stratified fluid had the drifting state

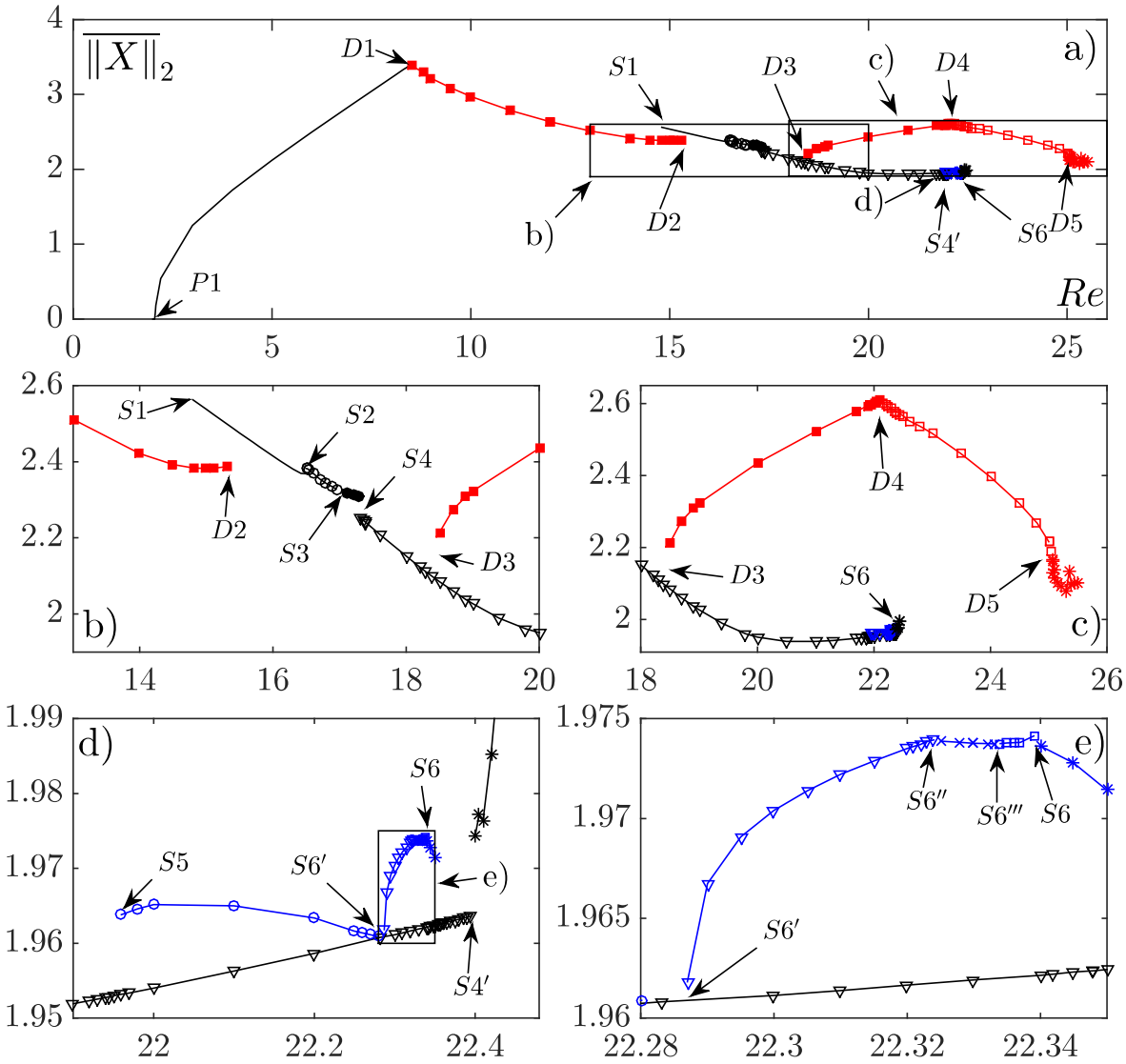

Figure 2.10: Bifurcation diagram of the stratified Kolmogorov flow when $Ri = 10^{-3}$ and $Pr = 1$. The panels are progressive magnifications of the diagram. The points are the temporal mean of $\|X\|_2$ for each numerical solution. Refer to Fig.2.1 for symbols legend. Here $(-*)$ is the chaotic transition of the glued state. The subcritical period-tripling bifurcation is (-o). $(-\triangledown)$, $(-\times)$ and $(-\square)$ are the period-doubling bifurcations and $(-*)$ is its chaotic bifurcation.

branch to become unstable in the window $Re(D2, 0) < Re < Re(D3, 0)$; for $Ri = 10^{-3}$ this region becomes significantly broader, see Table 2.1. From $Re(D3, 10^{-3})$ the drifting state regains its stability. It maintains the same symmetries as before the bifurcation $D2$, and in $D4$ undergoes a Hopf bifurcation. In Fig.2.13 we can see how the oscillatory behavior

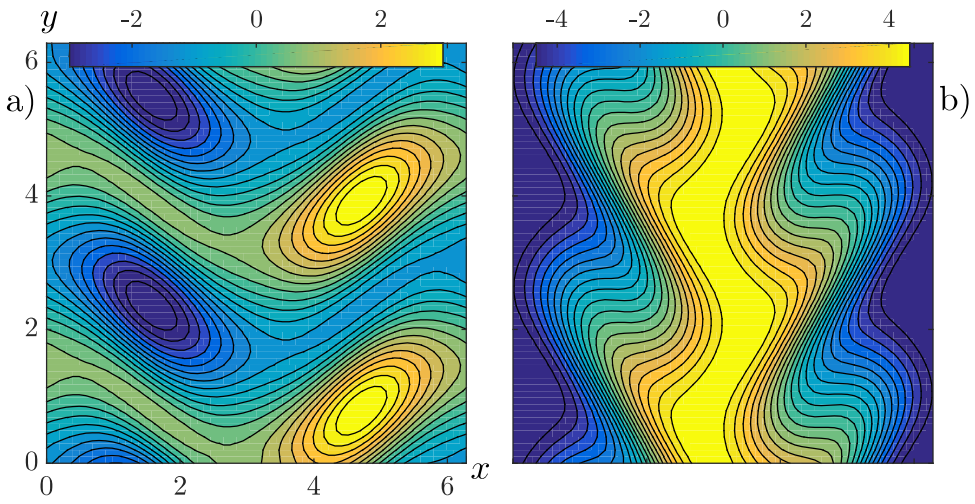

Figure 2.11: Steady state solution when $Re = 8.4$, $Ri = 10^{-3}$ and $Pr = 1$. Vorticity is in the left panel and temperature variations on the right.

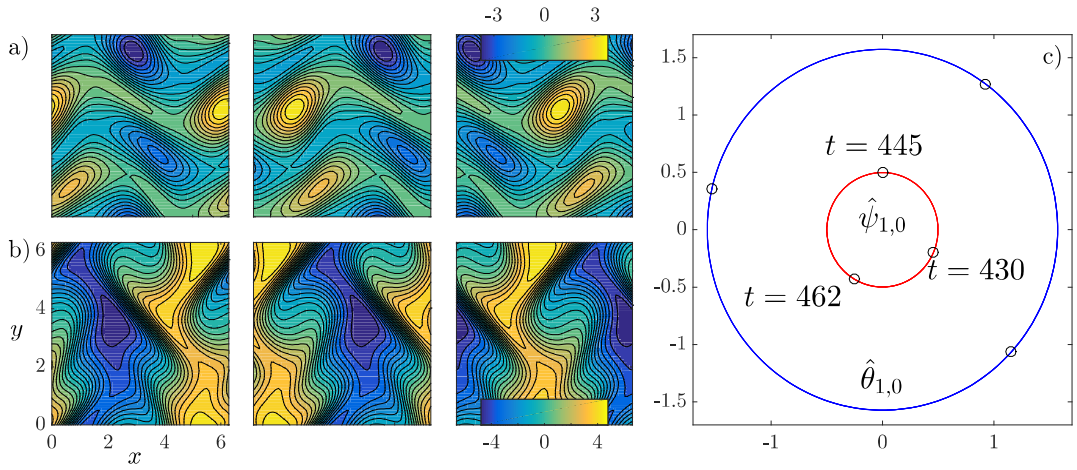

Figure 2.12: Time evolution of the drifting state where $Re = 12$, $Ri = 10^{-3}$ and $Pr = 1$. Top and middle panels are for vorticity and temperature respectively. Over a period length these are snapshots taken at $t = 430, 445, 462$. The bottom panels show the horizontal position of the maximum (red dots) and minimum (blue dots) as function of time. The motion of the vorticity and of the temperature extrema are shown in panels b) and in c) respectively. Real and imaginary part of the mode $(1, 0)$ are shown in panel a) for both stream function and temperature.

mixes with the drifting behavior: there is a vertical oscillation due to mode $(0, 1)$; the horizontal drift behaves as for the purely drifting solution; while mode $(1, 1)$ oscillates while

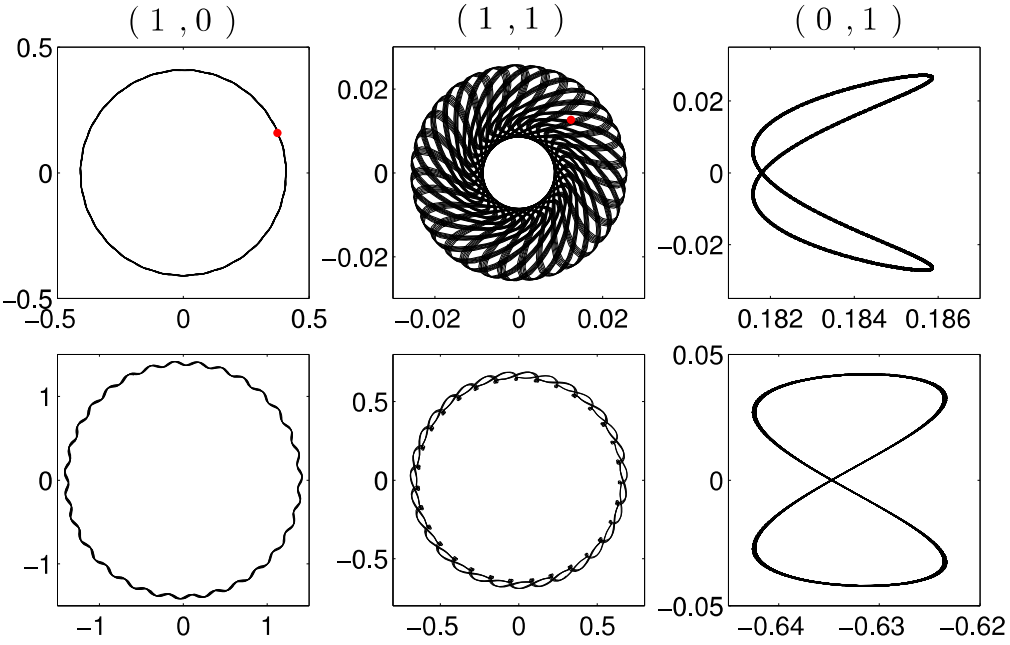

Figure 2.13: Oscillating drifting solution when $Re = 22.35$, $Ri = 10^{-3}$ and $Pr = 1$. Phase portraits of modes $\boldsymbol{k} = (1,0)$, $(1,1)$ and $(0,1)$: the axes are the real and imaginary part of $\widehat{\psi}_{\boldsymbol{k}}$ for the top panels and $\widehat{\theta}_{\boldsymbol{k}}$ for the bottom panels.

drifting. We recall that for purely drifting solutions the mode $(0,1)$ has a constant value while the phase portrait of $(1,0)$ is a circle. The final bifurcation we observe on this branch is towards a chaotic attractor in $D5$, where the drifting-and-oscillating state is destabilized earlier because of the temperature gradient: $Re(D5, 10^{-3}) < Re(D5, 0)$. The chaotic state presents the intermittent feature typical of the non-stratified Kolmogorov flow.

2.4.3 Hopf bifurcation, glued states and period-tripling for $Ri = 0.001$

Now we consider the steady state that becomes stable in $S1$. The main differences introduced by stratification are on this branch and on its transitions. For this increased Richardson number, as mentioned above, the stability region of the drifting branch shrinks. On the other hand, the stability region of the steady branch becomes larger. The steady state bifurcates for $Re(S1, 10^{-3}) < Re(S1, 0)$. After this, it follows the series of periodic orbit bifurcations similar to what we have seen for the non-stratified fluid; in Fig.2.14 we present the phase portraits of the real and imaginary part of modes $\widehat{\psi}_{0,1}$ and $\widehat{\theta}_{0,1}$. From left to right we see: First, at $Re = 16.3$, the states that had been generated by the Hopf

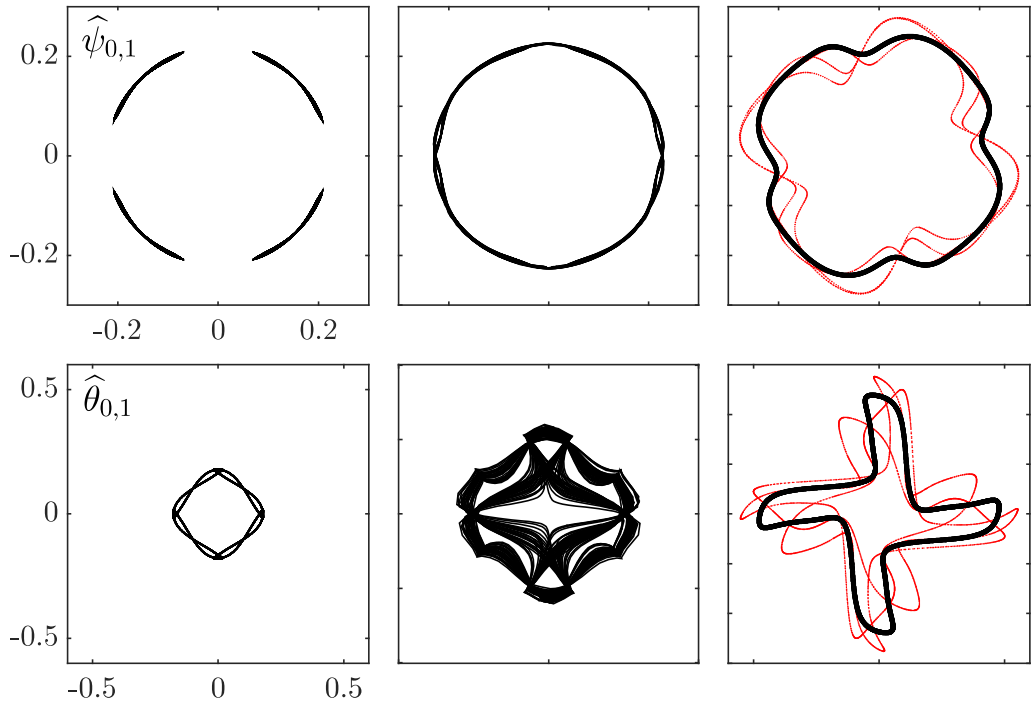

Figure 2.14: Phase portraits of the mode $\boldsymbol{k} = (0,1)$ when $Ri = 10^{-3}$, $Pr = 1$ and $Re = 16.3, 16.9, 21.96$ (left to right) along the branch with horizontally steady solutions. The axes are the real and imaginary part of $\widehat{\psi}_{0,1}$ for the top panels and $\widehat{\theta}_{0,1}$ for the bottom panels. When $Re = 21.96$ the glued periodic orbit (black curve) coexists with its period-tripled state (red curve).

bifurcation at $S2$ for $Re(S2, 10^{-3}) \approx 15.95$. Second the gluing bifurcation at $Re = 16.9$ and then for $Re = 21.96$ we show a glued periodic orbit (black line) together with its period-tripled state (red line). The Hopf states presents localized oscillations which are shown in Fig.2.15. Panels f) and l) show the horizontal position of the extrema as function of time for vorticity and temperature respectively, panels a) and g) are for the vertical positions. We see the extrema to oscillate around a position which is constant in time. This behavior is also evident from the phase plots of Fig.2.15. In fact the modes $(1,0)$ and $(0,1)$ are localized in the phase plane for both vorticity and temperature, and follow trajectories that do not embed the origin, and no drift is present. When the Hopf state loses its stability, and the gluing-bifurcation occurs, we observe global drifts in both horizontal and vertical directions: this is evident from panels a), f), g) and l) in Fig.2.16. One can recognize the same features observed in Fig.2.6. The fluid now drift horizontally at a constant velocity

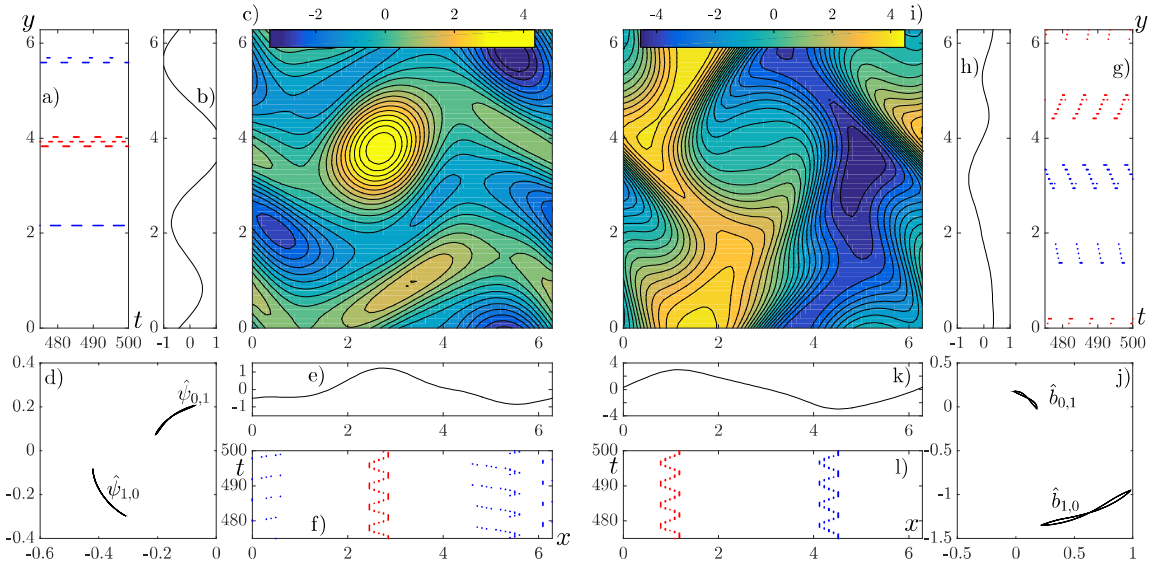

Figure 2.15: Time evolution of the Hopf state when $Re = 16.3$, $Ri = 10^{-3}$ and $Pr = 1$. Contour plots in panels c) and i) are the vorticity and temperature. Panels e) and b) show the horizontal and vertical averages of the vorticity solution and panels k) and h) are for temperature. Panels a) and f) report the temporal position of the vorticity extrema while panels l) and g) are for temperature: red dots are maxima and blue minima positions. The phase portrait of the real and imaginary part of $\widehat{\psi}_{\boldsymbol{k}}$ and $\widehat{\theta}_{\boldsymbol{k}}$ for $\boldsymbol{k} = (1, 0)$, $(0, 1)$ are shown respectively in panels d) and j).

and, at the same time, vortices oscillate. We can infer this behavior from panel f) and l) also. On the other side, along the vertical direction, the fluid inverts it direction of motion randomly, see panel a) and g). For the non-stratified fluid, after $S4$, the gluing process reaches a stable limit cycle which bifurcates supercritically in $S5$ towards the period-tripled state. On the contrary, in the stratified case, the bifurcation in $S5$ is subcritical and the glued state coexists with the period-tripled state branch until $S4'$. In Fig.2.17 we show solutions for $Re = 21.96$, slightly after the period-tripling bifurcation $S5$, but still on the branch of the glued state. The horizontal drift stopped, but the vertical is still present, as we can infer from the phase plots and the extrema time evolution. The glued state persists until $Re(S4', 10^{-3}) = 22.38$, where it reaches a chaotic state. When at $S5$ the period-tripled state appears, the overall dynamics of the solution is similar to the glued solution, except that the cycle repeats itself after three times of the original period: the panels on the right side of Fig.2.14 compare the phase portraits of mode $\boldsymbol{k} = (0, 1)$ for the glued state and its period-tripled counterpart.

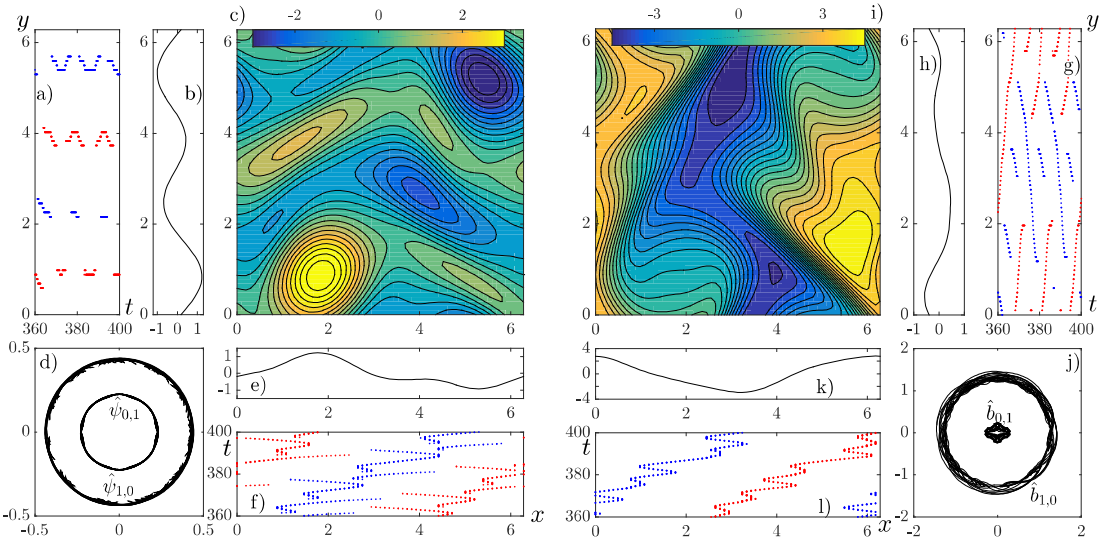

Figure 2.16: Time evolution of the gluing periodic orbit when $Re = 16.9$, $Ri = 10^{-3}$ and $Pr = 1$. Contour plots represents vorticity solutions in panel c) and temperature in panel i). Horizontal and vertical averages of the vorticity solution are in panels e) and b) and in k) and h) for temperature. The temporal position of the extrema of the mean fields are reported in f) and a) for vorticity and l) and g) for temperature. Red dots for maxima and blue for minima. The phase portrait of the real and imaginary part of $\widehat{\psi}_{\boldsymbol{k}}$ and $\widehat{\theta}_{\boldsymbol{k}}$ for $\boldsymbol{k} = (1,0)$, $(0,1)$ are shown respectively in d) and j).

2.4.4 Transition to chaos for $Ri = 0.001$

The bifurcations departing from the period-tripled state branch (shown in panel e) of Fig.2.10) are what makes the main difference from the non-stratified fluid: the transition towards the chaotic regime (which occurs between S5 and chaotic bifurcation in S6) is now more complicated. In fact the period-tripled state undergoes, in $S6'$, a period-doubling bifurcation which is followed by two subsequent period-doubling bifurcations (in $S6''$ and $S6'''$). After this bifurcation, finally, the branch reaches the chaotic regime, which sets-in at $Re(S6, 10^{-3}) \approx 22.33 > Re(S6, 0) \approx 21.92$. As we can see in panel d) and j) of Fig.2.18 the vertical wave vector $(0,1)$ keeps the dynamics of the period-tripled state: it encloses the origin three times before repeating itself. Before the bifurcation $S6'$, the horizontal mode $(1,0)$ has a localized oscillation as one can see in the middle column of Fig.2.17. After the bifurcation in $S6'$ a horizontal drift superposes to the oscillation, indeed the resulting phase portrait is a periodic oscillation around a circle centered in the origin - see panel d) and j) of Fig.2.18. This produces the oscillating horizontal drift as we can infer from the extrema

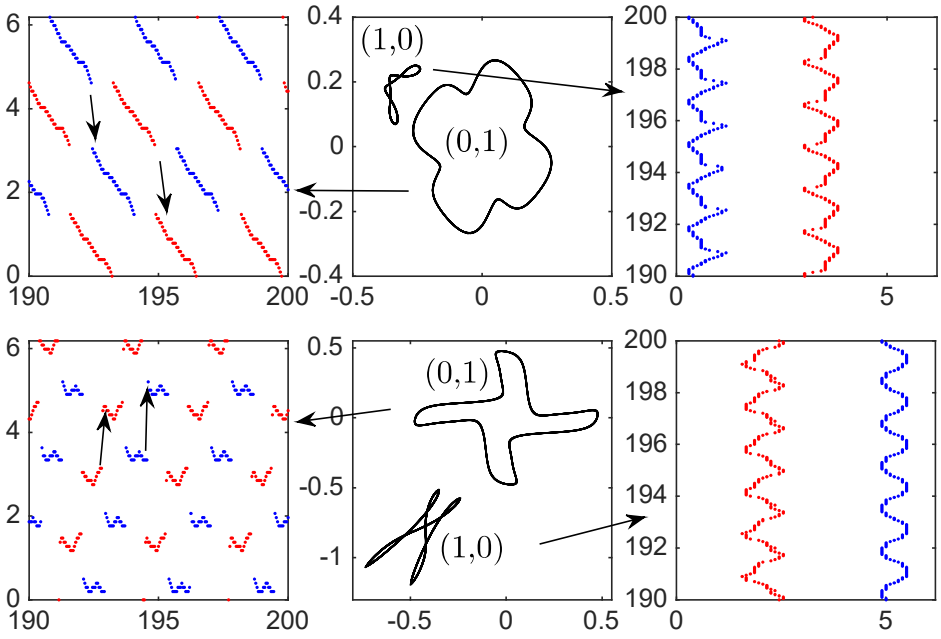

Figure 2.17: Glued-state solution when $Re = 21.96$, $Ri = 10^{-3}$ and $Pr = 1$. Top panels are for vorticity and temperature is in the bottom panels. On the left there are time-evolution for the vertical extrema and on the right for the horizontal ones. Middle panels are the phase portraits for modes $\boldsymbol{k} = (1, 0), (0, 1)$.

time evolution in panels f) and l). The horizontal drift has a long time periodicity which is not evident from the $L^2 - norm$ of the system. In Fig.2.19 we show the oscillation period T of the norm for periodic orbits belonging to the steady branch as function of Re. We can clearly see the broadening of the steady state branch due to the stabilizing temperature stratification. As pointed out by the arrows we see also the chain of period-tripling and three period-doubling bifurcations.

2.4.5 Ri=0.005

We step further and consider a higher Richardson number which is the highest value we study in this work. Surveying simulations at $Ri = 0.01$ show a number of states not ascribable to the common Kolmogorov route to chaos so we picked $Ri = 0.005$ which possesses the main structure of the non-stratified case, but also introduces important variations to the route to chaos. Compared to the non-stratified fluid the set of transitions has relevant

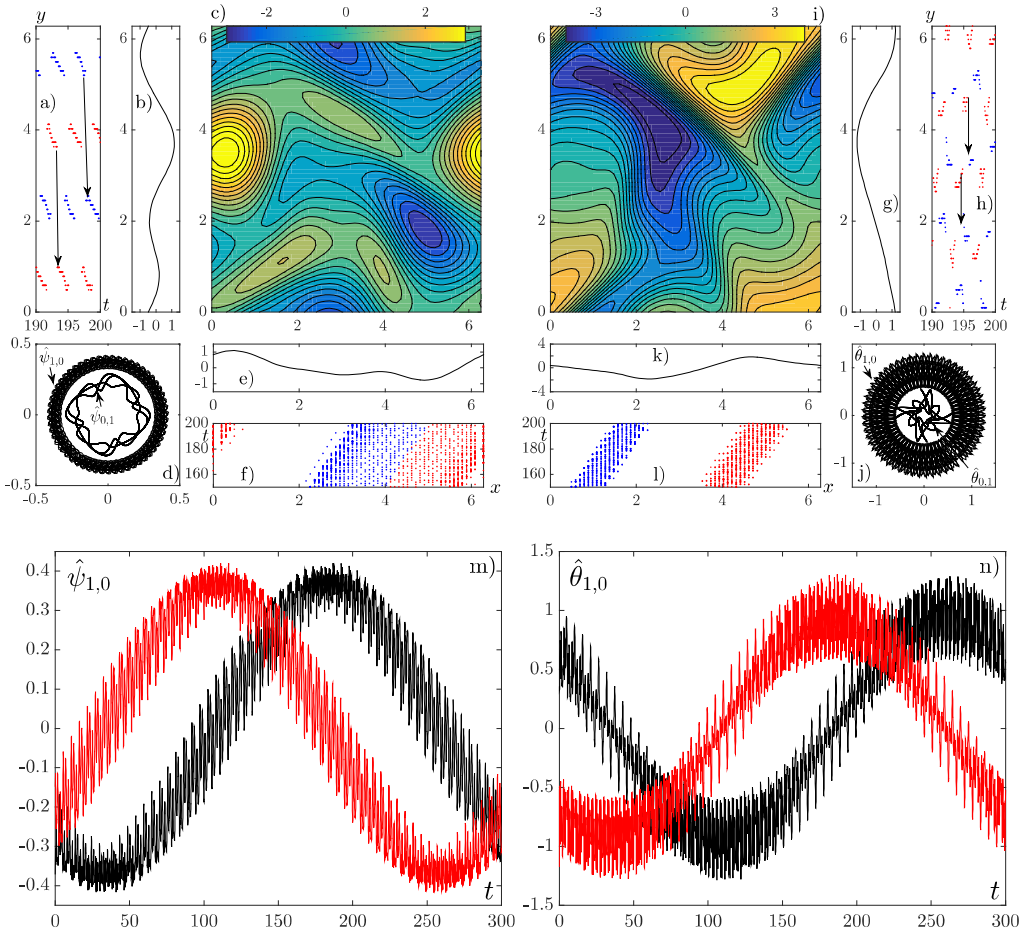

Figure 2.18: Drift-and-oscillating solution when $Re = 22.287$, $Ri = 10^{-3}$ and $Pr = 1$. Contour plots are c) vorticity and i) temperature. Horizontal and vertical averages of the vorticity solution are in panels e) and b) and in k) and g) for temperature. The temporal position of the extrema of the means are reported in f) and a) for vorticity and l) and h) for temperature. Red dots for maxima and blue for minima. The phase portrait of the real and imaginary part of $\widehat{\psi}_{\boldsymbol{k}}$ and $\widehat{\theta}_{\boldsymbol{k}}$ for $\boldsymbol{k} = (1,0)$, $(0,1)$ are shown respectively in d) and j). Panels m) and n) show the trajectories of the real and imaginary part of mode $(1,0)$ for the vorticity and temperature over a drifting period.

differences, but these mostly affect the branch departing from the steady states. In Fig.2.20 we show the bifurcation diagram where we find bifurcations $P1$, $D1$, $D2$, $S1$, $S2$ to be still present, but shifted in Reynolds number. The main differences lie in the gluing process, in the stability of the resulting glued state, in its bifurcation and subsequent route to chaos and in the bifurcation point D3 of the horizontal drifting states branch.

As we may infer from Tab.2.1 and Fig.2.20, the first transitions are slightly shifted

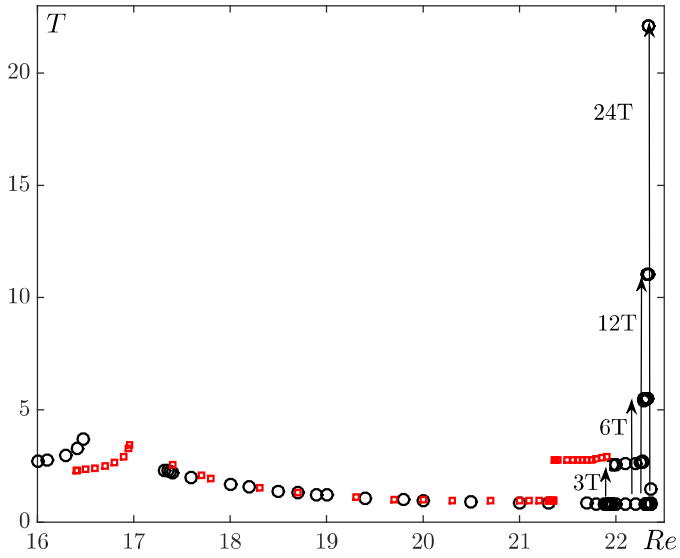

Figure 2.19: Oscillation period (T) of the horizontally steady solutions versus the Reynolds number. (□) is for $Ri = 0$ and (○) for $Ri = 10^{-3}$.

by stratification - larger Re are required to destabilize the laminar solution. The drifting state branch, lying between D1 and D2, has been shifted to higher Re and shortened in length while the steady state branch departing from S1 appears at lower Re. As observed when Ri is smaller, the four steady state solutions undergo a Hopf bifurcation in S2 and a gluing bifurcation in S3 which settles to a periodic orbit in S4. When $Ri = 0.005$ the gluing process between S3 and S4 is suppressed (see panel b) of Fig. 2.20) - the four Hopf solutions abruptly merge to two glued states. From the same panel we observe a completely new bifurcation in $S4_c$. The glued state loses its stability, the solution becomes chaotic, and then the flow recovers its stability in $S4'_c$. We show in panel a) of Fig. 2.21 the Lyapunov exponents of this chaotic window along this branch. We show the three largest exponents as function of the Reynolds number and observe that $\lambda_i \leq 0$ everywhere except inside the window, where the largest exponent (λ_1) becomes positive, proving these states are chaotic. In panel b) and c) we show the norm $\|\psi\|_2$ versus $\|\theta\|_2$ near the boundaries of the chaotic window where we observe the stable solution is the green thick line and the chaotic solution is the black line.

When the glued state regains its stability in $S4'_c$ it persists until $S4'$ where it shows another difference to the less stratified counterparts. Instead of bifurcating through a period-tripling, as in the previous cases, it suffers a period-doubling bifurcation as we see in the

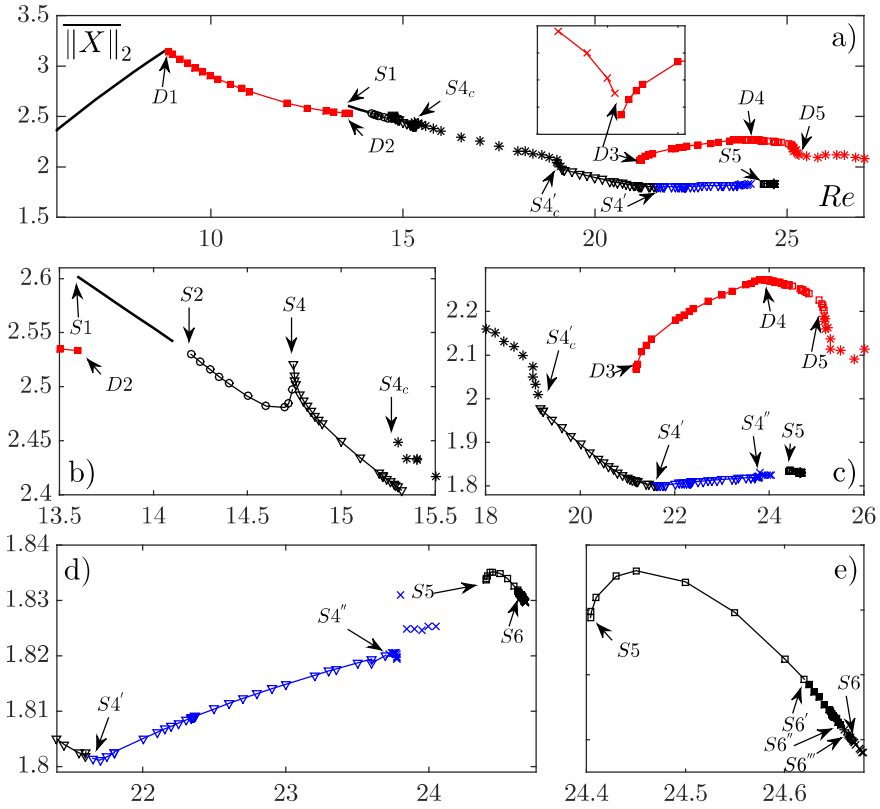

Figure 2.20: Bifurcation diagram of the stratified Kolmogorov flow when $Ri = 5 \cdot 10^{-3}$ and $Pr = 1$. The insets are progressive magnifications of the diagram. The points are the temporal mean of $\|X\|_2$ for each numerical solution. Refer to 2.1 for symbols legend. The blue branch contains period-tripled and period-doubled states.

inset of panel a) in Fig. 2.22. This state persist until S4″ where it becomes chaotic as we can see in panels b, c, d) on the same figure. Together with the phase portraits we show the time spectra of $\|X\|_2$ highlighting the enrichment of frequencies as Re grows. The black lines in panels b,c,d) mark the case of the stable period-doubled solution. As we see in panel b), more subharmonics appear and when we look at c) we see that the spectra has lot of noise with the main frequencies of the stable solution still present. In the final case d) the noise become predominant and most of the characteristic frequencies have been suppressed.

In Fig.2.20, especially in panel d), we see that the chaotic solutions coming from the period-doubled state disappear until a period-tripled state becomes stable in $S5$. This branch is shown in Fig.2.20e and is characterized by three subsequent period-doubling bifurcations in $S6'$, $S6''$ and $S6'''$. The last stable solution is a period 24th-tupling and is

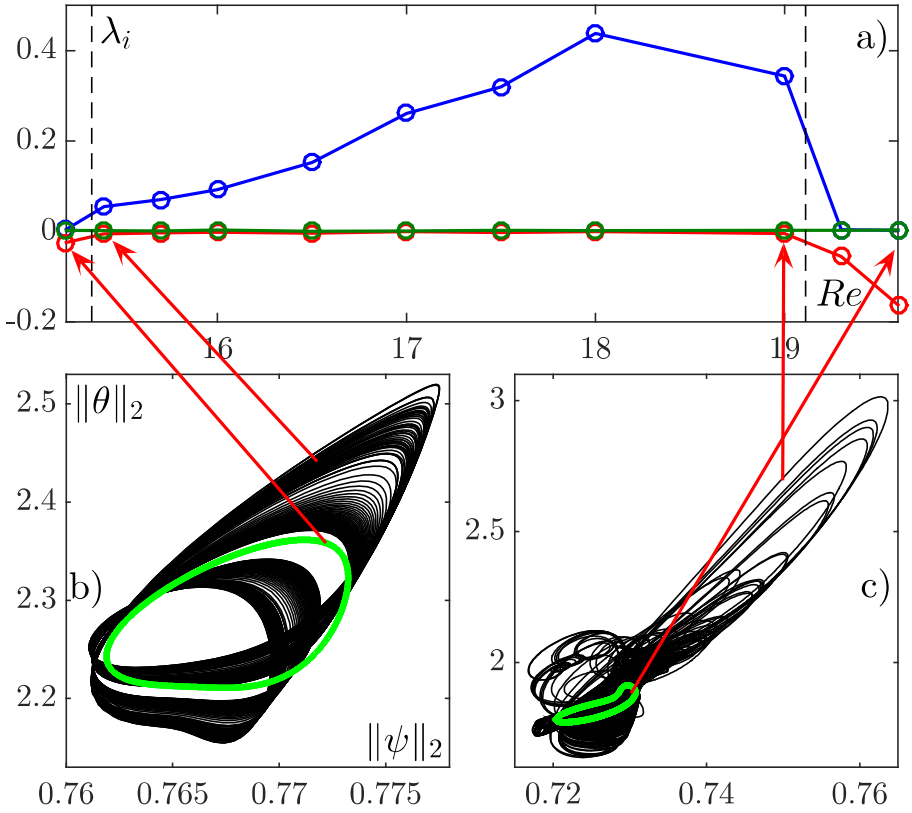

Figure 2.21: Chaotic window inside the glued-state branch when $Ri = 0.005$. In panel a) there are the three largest Lyapunov exponents λ_1, λ_2, λ_3 for solutions before and after the boundaries (marked as vertical dashed lines) of the chaotic window. In panels b) and c) we show the phase portrait in the plane of the streamfunction and temperature's L^2-norm. The black lines are for the solutions inside the chaotic window and the green thick lines are the stable solutions outside this region. In b) we show norms for $Re = 15.2$ and 15.4. In c) there are $Re = 19$ and 19.6.

shown in the inset of Fig.2.23 as a green line. In $S6$ this state lose its stability and becomes chaotic, as is proved by the Lyapunov exponents in the same figure.

Now we consider the branch of the horizontal drifting solutions. The density stratification is finally strong enough to affect the bifurcation points of this branch, in particular a new state before the bifurcation point $D3$ becomes accessible. The bifurcation of the four traveling solutions (that from $D3$ lead to the intermittent bursting states) are shifted by the increase of the stratification as we can see from Tab. 2.1. The difference lies in the appearance, before $D3$, of a stable branch of bursting solutions, whose L^2-norm is shown in panel a) of Fig. 2.24. This branch, that we have been unable to detect for lower Ri, is

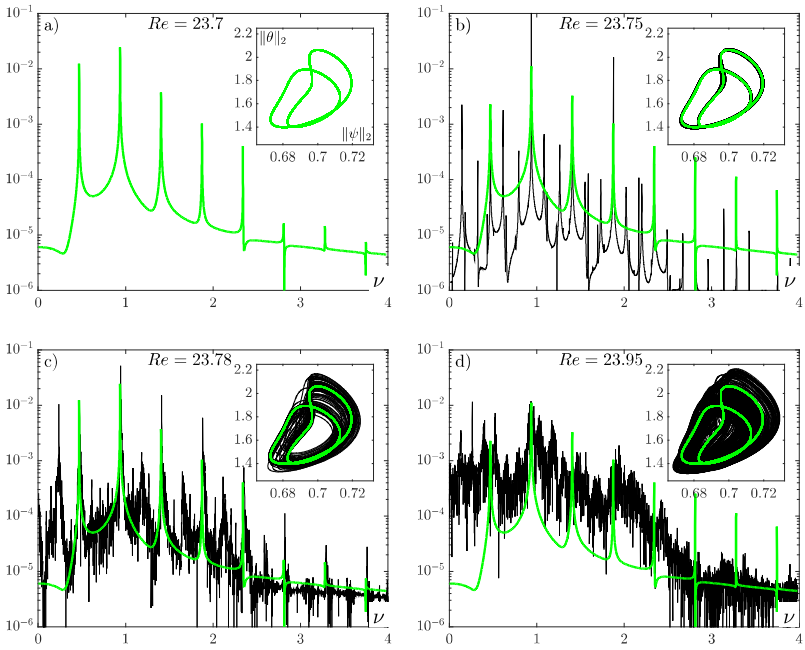

Figure 2.22: Time spectra and phase portraits of solutions near the bifurcation to chaos S4″ of the period-doubling solution. In the four panels we show solutions at $Re = 23.7$, 23.75, 23.78 and 23.95. In the panels we superpose the period-doubled solution of panel a) as a reference.

made of solutions that periodically jump between the four drifting states. For higher Re the switching between these states is prevented, see panel b) and in $D4$ they transition to a periodic orbit solution as we can see in panel c). Their further transition to the bursting solution, which was present also in less stratified fluid and we confirm it is chaotic by the Lyapunov exponents analysis. In panel e) in figure 2.24 we show the three larger Lyapunov exponents where one of them becomes positive after $D5$ (marked as a dashed vertical line).

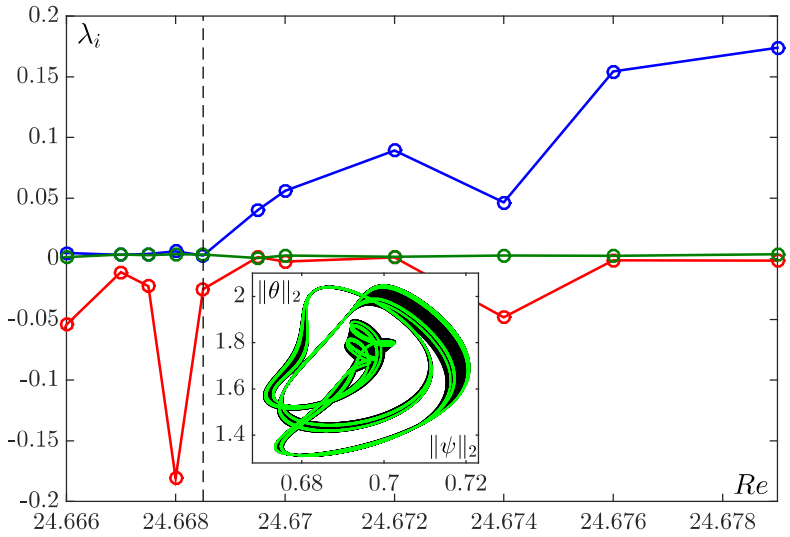

Figure 2.23: Lyapunov exponents across the transition to chaos in $S6$ which is marked as a vertical dashed line. In the figure are shown the three strongest exponents and in the inset we show the phase portrait in the $(\|\psi\|_2, \|\theta\|_2)$-plane of the solution before ($Re = 24.6675$) and after ($Re = 24.6695$) $S6$.

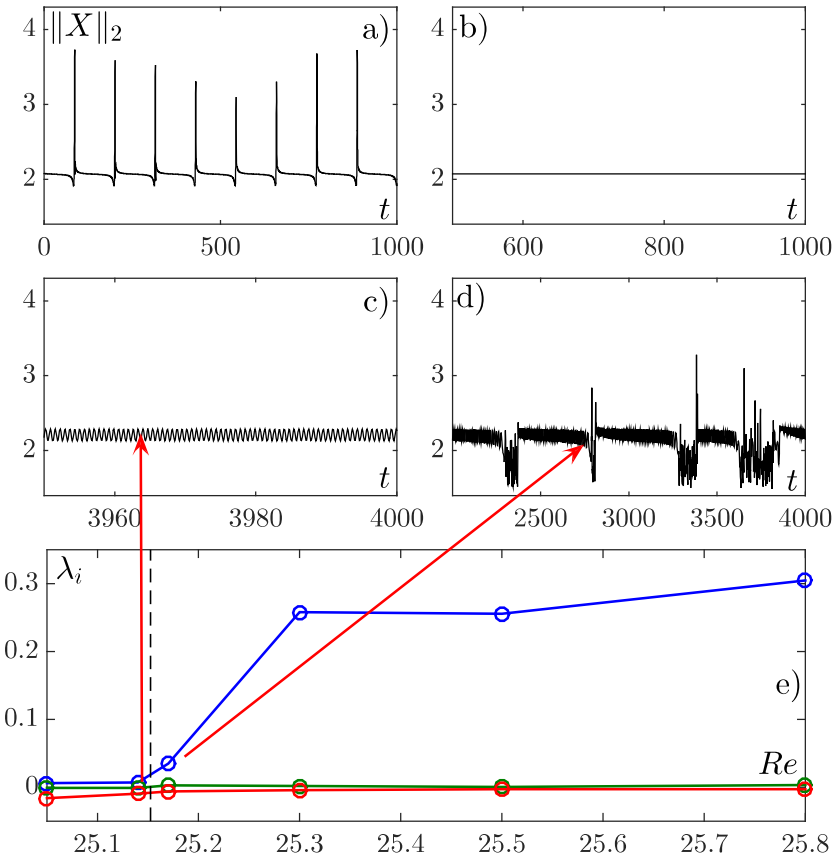

Figure 2.24: Time evolution of $\|X\|_2$ is shown for solutions on the drifting branch. Solutions refer to: a) $Re = 21.187$; b) $Re = 21.194$; c) $Re = 25.14$; d) $Re = 25.18$. In b) there is the drifting solution and in a) its bursting precursor. In c) there is the oscillating drift solution and in d) the intermittent bursting solution.

Chapter 3

Part II: Multi-layered Fluids

3.1 Introduction

Here we explore a different aspect in stratified shear flows. We want to study the interplay between internal gravity waves and a background sharing velocity in a multilayered fluid. Internal gravity waves separates neighboring fluid layers of different density, riding the interface between the two layers where the density gradient abruptly changes - see Sutherland (2010). The phase velocity of these free waves depends on the density difference between the layers and is Doppler shifted when a background shear is present. Here we consider a number of interfaces separating uniform density layers in a statically stable fluid with an inflection-free shear velocity. Each interface carries two waves propagating in opposite directions from the background shear at the interface - i.e. there is a fast and a slow propagating wave per interface. By tuning the Richardson number, that means tuning the shear rate and/or the density difference between the layers, the phase velocity varies and when two waves have equal phase velocity, the so called Taylor-Caulfield Instability (TCI), arises. Its finite amplitude state is an elliptical billow of nearly constant intermediate density embedded by vorticity filaments which moves at the critical layer velocity. The number of interfaces we consider here ($M \geq 2$) allows multiple resonances at different levels and different distances. The study of linear stability and subsequent nonlinear evolution of such interactions is the subject of this chapter.

Resonating waves are key elements for instabilities in stratified shear flows, which can be explained via the *waves interaction approach*. It has been introduced by Taylor (1931) and allows to interpret instabilities in steps-shaped vorticity and density profiles in parallel

flows - see Cairns (1979), Sutherland (2010), Carpenter et al. (2011) and Guha and Lawrence (2014). Such flows allow the growth of three instabilities according to the waves to interact: *i*) vorticity-vorticity waves; *ii*) a vorticity wave and an internal gravity wave; *iii*) two internal gravity waves - see Caulfield (1994), Baines and Mitsudera (1994) and Carpenter et al. (2010a) for a detailed review of these instabilities.

The first case is the classical Kelvin-Helmholtz Instability (KHI) from the works of Helmholtz (1868) and Kelvin (1871) and it is the most studied and observed variety of stratified shear instability. Its nonlinear evolution develops a pattern of overturning billows: e.g. in Thorpe (1968) a train of billows has been realized in laboratory experiments and by numerical simulations in Scinocca and Ford (2000) as well, whilst in field measurements it has been reported in Smyth and Moum (2012). The second most studied instability (*ii*) arises when a wave on a vorticity interface resonantly interacts with an internal gravity wave lying on a density interface - see Holmboe (1962) and Alexakis (2005) - and is usually referred as the Holmboe Wave Instability (HWI). It has been observed in numerical simulations Carpenter et al. (2010b) and Balmforth et al. (2012), and have been reproduced in laboratory experiments, Thorpe (1971) and Tedford et al. (2009). This instability nonlinearly settles to a finite amplitude state of propagating vortices scouring the density interface which develops cusp-like waves - see Smyth et al. (1988) and Thorpe (1968) for numerical and experimental observations of the finite amplitude state. KHI and HWI are considered robust instabilities in the sense that they have been observed in natural systems, experiments and numerical simulations to persist for long timescales for a broad range of different initial conditions and the "zoo" of secondary instabilities they suffer - see Caulfield and Peltier (2000), Mashayek and Peltier (2012a,b), Balmforth et al. (2012) and Arratia et al. (2013).

Taylor (1931) also pointed out the possibility of a third instability to develop in a stratified shear flow. Waves riding density interfaces can resonantly interact when their phase speed become locked thanks to the Doppler-shifting effect of a background shear flow. This instability has been more elusive to observe, with the scientific community more concerned with why one might find basic states with layered density profiles in the first place. Taylor's instability was quantified and studied in more detail by Caulfield (1994), in parallel with some first laboratory experiments Caulfield et al. (1995) and nonlinear simulations Lee and Caulfield (2001). Balmforth et al. (2012) provided a comprehensive study of TCI in the

long-wave limit that two density interfaces were considered as a stratified "defect" in the shear flow. These works, together with last remarks on laboratory experiments in Taylor (1931), showed the elusive nature of this instability. In spite of its theoretical feasibility, TCI is difficult to be observed in laboratory experiments as well as in natural phenomena. In Caulfield et al. (1995) it has been shown that in laboratory frameworks the middle layer shrinks progressively, while the vorticity filaments embedding the billows of the finite amplitude solution promote the onset of secondary instabilities (see Lee and Caulfield (2001) and Balmforth et al. (2012)) - these phenomenologies make the finite amplitude state short living and difficult to be observed.

Here we explore the linear stability and nonlinear evolution of multiple TCI growing on a multilayered density profile. We consider a density staircase with a number M of equally spaced steps of equal size with a background linear shear flow extending to infinite. This fluid geometry is free of vorticity gradients, thus no KHI and HWI are supported, providing a framework where we can focus on TCI. We study the stability of horizontal normal mode solutions of the incompressible 2D Navier-Stokes and energy conservation equations under the Boussinesq approximation. In the inviscid and non-diffusive limit, our results show a predominance of near-neighbor interfaces TCI which are particularly strong when the bulk Richardson numbers and wavenumbers are small. This result suggests to set up an asymptotic expansion which allows to reduce the equation to a simplified model. Assuming any strong gradient to be embedded inside a thin layer (a *defect*) of vertical dimension much smaller than the horizontal domain, Gill (1965) exploited a matched asymptotic expansion to describe the dynamics inside a vorticity defect - see also Balmforth et al. (1997) and Balmforth (1998) which studied unstratified shear flows. In Balmforth et al. (2012) this approach have been extended to the stratified counterpart and we take advantage of their expansion to study our multilayered fluid. The expansion reduces the governing equations to a Vlasov-like problem giving a simplified model where to study the nonlinear evolution of large-scale internal gravity waves.

We also tackle two side aspects of the stability analysis of multilayered fluids: *i*) the effect of viscosity and *ii*) the effect of thickening the interfaces. Firstly we account for viscosity effects on the linear stability of these horizontal waves. It is not clear whether or not the wave interaction approach (Carpenter et al. (2011)) may give physical insight in the stability properties of viscous modes. Therefore, following the approach of Balmforth et al. (1997)

and Balmforth (1998) adopted for unstratified viscous shear flows, we solve numerically the linear stability problem of the stratified counterpart showing an enriched spectrum of unstable waves. Secondly we deepen the linear stability analysis in the full framework of the Boussinesq equations considering interfaces of finite thickness. Alexakis (2005) showed that smoothing out vorticity and density interfaces preserves KHI and HWI while introducing new instability domains. Unstable modes belonging to the newly formed instability bands appear for larger Richardson numbers and show finer structures due to higher harmonics of the spectrum. Here we consider a three layers fluid where the two interfaces are piecewise-linear profiles and observe analogous results for the TCI and compare them to the classical results of sharp interfaces.

This chapter is structured as follows. In §3.2 we formalize the fluid geometry, variables rescales, non-dimensionalizations and the defect theory approximations where we expand the equations in terms of the parameter ε to promote the leading order terms inside the density defect. In §3.4 we study the linear stability of the multilayered shear flow. This analysis reduces to the study of the Taylor-Goldstein eigenvalue problem, that is inviscid and non-diffusive modes are accounted. In the first instance we briefly review the Taylor-Caulfield instability, then we generalize to the case of $M > 2$ sharp interfaces. Under the defect approximations we refine the analysis near the stability boundary of the most unstable waves. In this limit we also consider two more phenomenologies: *i*) the effect of smoothing the interfaces and *ii*) the effect of viscosity in the stability problem. The detailed linear analysis we performed in the defect limit inspired numerical computations for which, in §3.6, we show the results of computing the defect equations when the fluid presents four interfaces of finite thickness and small viscosity. In the Appendix we report few satellite results of the linear stability analysis. In studying the linear stability of a multilayered flow we assume equally spaced sharp interfaces. We thus test the robustness of these results by assuming randomly displaced interfaces and compare the results of 100 realizations to the evenly spaced case in §A.1.1. Moreover we investigate the effect of thickening the interfaces in the full set of equations. To attack the problem, as we show in §A.1.2, we consider a three layers fluid where the interfaces are piecewise-linear.

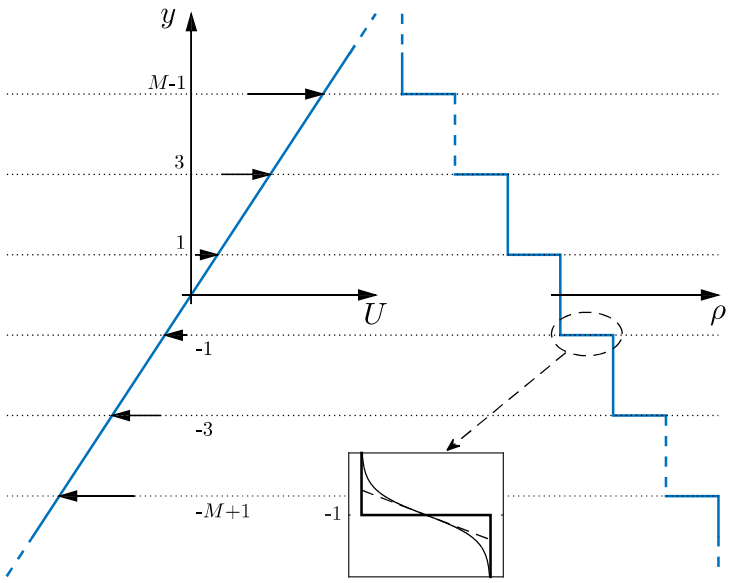

Figure 3.1: Here we show the basic density profile for a M interfaces fluid where the density decreases of $\Delta\rho$ with hight at any step. The thickness of the middle layers is $H = 2$ while the bounding layers extend to infinity. In the bottom panel we show the three interfaces profile that we use throughout the chapter: the thick line is a piecewise-constant interface; the dashed line represent a piecewise-linear interface; and the thin curve is the hyperbolic tangent interface.

3.2 Formulation

We consider a two-dimensional viscous and conductive incompressible vertical fluid under the effect of gravity g. Governing equations are given in (1.5)-(1.7) in the vorticity-streamfunction formulation and by introducing the buoyancy field $b^* = g\rho/\rho_r$ we get

$$\zeta^*_{t^*} + \psi^*_{x^*}\zeta^*_{y^*} - \psi^*_{y^*}\zeta^*_{x^*} = b^*_{x^*} + \nu^*\left(\zeta^*_{x^*x^*} + \zeta^*_{y^*y^*}\right), \tag{3.1}$$

$$\zeta^* = \psi^*_{x^*x^*} + \psi^*_{y^*y^*}, \tag{3.2}$$

$$b^*_{t^*} + \psi^*_{x^*}b^*_{y^*} - \psi^*_{y^*}b^*_{x^*} = \kappa^*\left(b^*_{x^*x^*} + b^*_{y^*y^*}\right), \tag{3.3}$$

where ζ^* is the vorticity, ψ^* the streamfunction and b^* the buoyancy fields. Here * denotes physical quantities. In terms of the velocity field (u^*, v^*), the vorticity is defined by $\zeta^* = v^*_{x^*} - u^*_{y^*}$ and the streamfunction is defined as $(u^*, v^*) = (-\psi^*_{y^*}, \psi^*_{x^*})$. The physical parameters are ν^*, κ^* the kinematic viscosity and the diffusivity respectively. The domain is an

infinitely deep channel of finite horizontal length scale L, i.e. $(x^*, y^*) \in [0, 2\pi L] \times [-\infty, +\infty]$. We assume the tree scalar fields to decay exponentially at $y^* \to \pm\infty$ and to be periodic in $x^* = 0$ and $2\pi L$. The basic velocity profile we consider here is a linear shear $(\bar{U}, \bar{V}) = (sy^*, 0)$ where s is the shear rate. The basic density profile $\bar{\rho}$ is given by a group of stacked layers of constant density which increases of $\Delta\rho$ at each layer with depth. The layers have thickness $2L$ except for the bounding layers which extend to infinity. We indicate with M the number of interfaces separating the layers, assume M to be even and the middle layer to be centered at $y^* = 0$. In figure 3.1 the basic density profile is shown together with a magnification of a single interface to show the three different kinds of interfaces we will consider throughout this work. Most of the attention is on the piecewise-constant density interfaces, but we consider also a piecewise-linear interface and a hyperbolic tangent interface.

To make the equations dimensionless we take L as characteristic lengthscale, $U = sL$ for the velocity, L/U as timescale and U^2/L for the buoyancy. We also explicit the variations from the basic state defining

$$\psi^* = -\frac{1}{2}ULy^2 + UL\psi, \qquad \zeta^* = \frac{U}{L} + \frac{U}{L}\zeta, \qquad b^* = \frac{U^2}{L}G(y) + \frac{U^2}{L}b \tag{3.4}$$

thus the nondimensionalized equations for the perturbations are

$$\zeta_t + \psi_x\zeta_y - \psi_y\zeta_x + y\zeta_x = b_x + \nu\big(\zeta_{xx} + \zeta_{yy}\big), \tag{3.5}$$

$$b_t + \psi_x b_y - \psi_y b_x + y b_x + G_y\psi_x = \kappa\big(b_{xx} + b_{yy}\big), \tag{3.6}$$

$$\zeta = \psi_{xx} + \psi_{yy}, \tag{3.7}$$

where the nondimensional parameters are the inverse Reynolds and Péclet numbers $\nu = \nu^*/UL$ and $\kappa = \kappa^*/UL$.

We consider the following interfaces profiles, as vertical derivative of the density field. The piecewise-constant profile

$$\Theta(y) = \delta(y), \tag{3.8}$$

the piecewise-linear profile

$$\Theta(y) = \frac{1}{4d}(1 - \mathrm{sgn}(|y|/d - 1)), \tag{3.9}$$

and the hyperbolic tangent profile

$$\Theta(y) = \frac{1}{2d}\mathrm{sech}^2(y/d), \tag{3.10}$$

Where d tunes the thickness of the last two profiles. Given a particular profile $\Theta(y)$ for every interface the vertical derivative of the density field is

$$G_y = J \sum_{j=0}^{M/2-1} \Big(\Theta(y-2j-1) + \Theta(y+2j+1)\Big), \tag{3.11}$$

where J is the bulk Richardson number that measures the strength of the density jump between the layers.

3.3 Defect theory approximation

In this section we introduce a simplified instance of equations (3.5)-(3.7). We consider a staircase of vertical dimension much smaller than the horizontal scale L and define $\varepsilon \ll 1$ their ratio. In this limit the staircase can be seen as an interface - the *defect* - in the density field where the strong gradients, the steps of the staircase, are flattened inside. Introducing appropriate rescales in ε allows to tune the magnitude of each term of the equations and build a matched asymptotic expansion. This method have been tailored to ease differential equations where a small parameter multiplies the highest derivatives. For this reason these terms are generally negligible except where the gradients are strong enough to balance the small parameter. Such expansions have been widely used to study boundary layers but in this work it describes a defect layer embedded inside an infinitely deep channel. Outside the defect the vertical variable y is of order one and we expect the main contribution to come from the advection of vorticity and buoyancy by the background shear. Inside the defect we resolve the domain defining the rescaled variable $\eta = y/\varepsilon$ which is of order one inside the defect where more terms interplay with the background shear.

To couch the expansion we rescale the perturbation fields ψ, ζ and b in terms of ε^2, for that the background shear is not affected by the perturbations and we rescale the time as t/ε. In this way we obtain the following set of equations that focus on weakly nonlinear and long timescales effects

$$\varepsilon\zeta_t + \varepsilon^2\psi_x\zeta_y - \varepsilon^2\psi_y\zeta_x + y\zeta_x = b_x + \varepsilon^3\nu\big(\zeta_{xx} + \zeta_{yy}\big), \tag{3.12}$$

$$\varepsilon b_t + \varepsilon^2 \psi_x b_y - \varepsilon^2 \psi_y b_x + y b_x + \varepsilon^2 \psi_x G_y = \varepsilon^3 \kappa \big(b_{xx} + b_{yy} \big), \tag{3.13}$$

$$\zeta = \psi_{xx} + \psi_{yy}, \tag{3.14}$$

where the rescaled inverse Reynolds and Péclet numbers are

$$\nu = \frac{\widehat{\nu}}{\varepsilon^3 U L} \quad \text{and} \quad \kappa = \frac{\widehat{\kappa}}{\varepsilon^3 U L}. \tag{3.15}$$

Outside the defect $y = O(1)$ and the leading order terms of (3.12) and (3.13) are

$$y(\psi_{xx} + \psi_{yy}) \sim b_x \text{ and } y b_x \sim 0, \tag{3.16}$$

where higher order terms in ε have been discarded. Since the vertical variable is of order one, to satisfy $y b_x \sim 0$, we take $b_x \sim O(\varepsilon)$. Thus we solve the Laplace equation $y(\psi_{xx} + \psi_{yy}) \sim 0$ of the streamfunction using Fourier series, for that the solution is

$$\psi = \sum_{n=-\infty}^{\infty} \Phi_n(t) e^{inx - |n|y} + \bar{\psi}(y,t), \tag{3.17}$$

and $\bar{\psi}(y,t) = \int_0^{2\pi} \psi(x,y,t) dx / 2\pi$ is the horizontal average of the streamfunction. In the solution appears $\Phi(x,t)$ which is the leading order streamfunction

$$\Phi(x,t) = \sum_{n=-\infty}^{\infty} \Phi_n(t) e^{inx}. \tag{3.18}$$

At the defect boundaries the derivative difference is

$$[\psi_y]_{y=0^-}^{y=0^+} = -2 \sum_{n=-\infty}^{\infty} |n| \Phi_n(t) e^{inx} + \big[\bar{\psi}_y\big]_{y=0^-}^{y=0^+}, \tag{3.19}$$

and this will be matched with the boundaries conditions on the inner equation.

Inside the defect we consider the rescaled vertical variable $\eta = y/\varepsilon = O(1)$ and the fields

$$\psi = \phi_0(x,t) + \varepsilon \phi_1(x,\eta,t), \qquad \zeta = Z(x,\eta,t)/\varepsilon, \qquad b = B(x,\eta,t), \tag{3.20}$$

which promote weakly nonlinear terms to the leading order and demote fully nonlinear terms to higher orders. From (3.14) we have $Z = \varepsilon \phi_{0xx} + \varepsilon^2 \phi_{1xx} + \phi_{1\eta\eta} \sim \phi_{1\eta\eta}$, whose derivative difference over the rescaled domain is

$$[\phi_{1\eta}]_{\eta=-\infty}^{\eta=+\infty} = \int_{-\infty}^{+\infty} Z \, d\eta. \tag{3.21}$$

Equating the inner and outer jumps across the defect we get

$$\int_{-\infty}^{+\infty} Z\, d\eta - < Z >= -2 \sum_{n=-\infty}^{\infty} |n| \Phi_n(t) e^{inx} := \mathscr{L}\Phi, \tag{3.22}$$

where $< \cdots >$ is the average over the domain of the inner equation. Injecting the rescaled variables and fields in equations (3.12) and (3.13) we get finally the defect theory equations

$$Z_t + \eta Z_x + \Phi_x Z_\eta - \nu Z_{\eta\eta} = B_x, \tag{3.23}$$

$$B_t + \eta B_x + \Phi_x B_\eta + \Phi_x G_\eta - \kappa B_{\eta\eta} = 0, \tag{3.24}$$

where to guarantee the matching with the outer solution, we get from (3.16) that Z_x and B_x vanish as $\eta \to \pm\infty$. Assuming $Pr = \nu/\kappa = 1$ we may further simplify the equations introducing $\mathscr{Z} = Z + B_\eta$ which gives

$$\mathscr{Z}_t + \eta \mathscr{Z}_x + \Phi_x \mathscr{Z}_\eta + \Phi_x G_{\eta\eta} - \nu \mathscr{Z}_{\eta\eta} = 0, \tag{3.25}$$

$$\mathscr{L}\Phi = \int_{-\infty}^{+\infty} \mathscr{Z}\, d\eta - < \mathscr{Z} >= -2 \sum_{n=-\infty}^{\infty} |n| \Phi_n(t) e^{inx}. \tag{3.26}$$

3.3.1 Numerical algorithm

Equations (3.25) and (3.26) are solved on the truncated domain $(x, y) \in [0, 2\pi] \times [-y_{max}, y_{max}]$, where y_{max} is sufficiently far from the interfaces - this is to prevent any interference with the dynamics. We solve an initial value problem by perturbing the equilibrium solution $\bar{\mathscr{Z}}(\eta) = G_\eta(\eta)$. The perturbations, of small amplitude A_0, are introduced in §3.3.2 and are: *i*) a transient forcing of particular modes of the leading order streamfunction $\Phi(x, t)$ as in (3.29) or *ii*) the leading order solution (3.30) and (3.31) of the weakly non linear expansion presented in §A.2. The defect equations are then time stepped by using the operator-splitting algorithm of Cheng and Knorr (1976) - tailored for this specific problem in Balmforth et al. (2012) - which provides $O(\Delta t^2)$ accuracy.

The scheme splits the equation into two advection equations and explicitly adds the diffusion of $\mathscr{Z}$. The first is a horizontal advection equation where $\mathscr{Z}(x, \eta)$ is advected by the background shear and the second is a vertical advection equation where to advect is the leading order streamfunction over the defect $\Phi(x)$. These equations are

$$\mathscr{Z}_t + \eta \mathscr{Z}_x = 0, \quad \mathscr{Z}_t + \Phi_x \mathscr{Z}_\eta = 0, \tag{3.27}$$

and are solved at different stages. The field $\mathscr{Z}^n(x,\eta)$ at the beginning of the integration step Δt is time stepped by advecting $\mathscr{Z}$ for the first half step $(\Delta t/2)$. The explicit solution is the horizontal shift $\mathscr{Z}_*(x,\eta) = \mathscr{Z}^n(x - \eta\Delta t/2, \eta)$ and is performed by a Fourier series interpolation on each horizontal grid level. Then $\Phi(x)$ is computed from an approximation of (3.26) and plugged into the vertical advection equation. The explicit solution is $\mathscr{Z}_{**}(x,\eta) = \mathscr{Z}_*(x, \eta - \Phi_x\Delta t)$ and the vertical shift is entrusted to a spline interpolation of $\mathscr{Z}_*(x,\eta)$ at any vertical grid line. At this stage the diffusion term is accounted explicitly by a central-difference differentiation in η and the last horizontal shift of $\Delta/2$ is computed giving $\mathscr{Z}^{n+1}(x,\eta)$ with $O(\Delta t^2)$ accuracy.

In our simulations we choose y_{max} to be placed at $M+2$ which guarantees the boundaries to have small influences on the flow dynamics. The domain is discretized using a grid subdivision X for the horizontal direction and $2Y+1$ for the vertical direction which are choosen according to the purpose of the simulation. Time step Δt in our simulations is such that $|v_{max}|\Delta t \leq \Delta\eta$, where v_{max} is the maximum vertical velocity and $\Delta\eta$ the vertical grid step. The condition means that the vertical advection is smaller than the grid interval and we take as time step $\min\left(\frac{\Delta\eta}{v_{max}}, 0.005\right)$. As a measure of the growth of the instabilities we compute the L^2-norm

$$a(t) = \left| \sum_{n=-N/2+1}^{N/2} |\Phi_n(t)|^2 \right|^{\frac{1}{2}} \tag{3.28}$$

of the leading order streamfunction (3.19).

3.3.2 Initial conditions

In our numerical simulations we run a series of initial values problems perturbing the basic state with three different initial conditions. We can kick a particular Fourier mode for a small amount of time

$$i_k = A_0\delta_{nk}\, t\, e^{-10t^2}, \quad \text{with}, k = 1, 2, \ldots, \tag{3.29}$$

where A_0 is usually 0.01. This initial condition cannot provide a specific phase velocity, which we will show in §3.4 that is a crucial mark for unstable waves. Thus, to probe the instability of these waves we need initial conditions that can provide a specific wavenumber and phase velocity at once. By using the leading order solution (A.18) from the weakly nonlinear theory (see section §A.2) we obtain an initial condition that perturb $k = 1$. By

providing $c = 0 + ic_0$ we get

$$I_0 = -\frac{A_0\, G_{\eta\eta}}{y^2 + c_0^2}\,(y \cos\, x - c_0 \sin\, x)\,, \tag{3.30}$$

and when $c = 2 + ic_2$

$$I_2 = -\frac{A_0\, G_{\eta\eta}}{(y-2)^2 + c_2^2}\Big((y-2) \cos\, x - c_2 \sin\, x\Big). \tag{3.31}$$

We use i_k mainly when we don't need to distinguish between different phase velocities, and I_0 or I_2 when this refinement is required. It is straightforward to extend these initial conditions to higher wavenumbers or different phase velocities, but the two shown here are the ones we use throughout this work.

3.4 Linear stability analysis

As shown in previous works (Sutherland (2010) and Carpenter et al. (2011)), TCI can be interpreted as a resonance between gravity waves supported by different density interfaces that arises when the Doppler-shifting effect of the background flow allows their horizontal phase speeds to lock together. This resonance requires a suitable choice for the bulk Richardson number which controls the natural phase speed of the waves in the absence of flow. For M interfaces, there are $\binom{M}{2}$ possible resonances that may lead to TCI when J is properly tuned.

3.4.1 Inviscid and non-diffusive fluids

We consider the inviscid and non-diffusive instance of (3.5) and (3.6), thus $\nu = \kappa = 0$. The equilibrium solution of these equations is function of the vertical direction and is given by (3.11). Our goal is to analyze the stability of the equilibrium profile to linear perturbations of normal mode form

$$[\psi, \zeta, b](x, y, t) = [\widehat{\psi}, \widehat{\zeta}, \widehat{b}](y)\, e^{ik(x-ct)}, \tag{3.32}$$

where k is the horizontal wavenumber and $c = c_r + ic_i$ is the complex phase velocity: positive c_i gives an exponentially growing mode whilst a negative c_i gives an exponentially decaying one. Because the horizontal domain is periodic, the wavenumber assumes integer values. Injecting (3.32) into (3.5) and (3.6) and discarding the nonlinear terms the system reduces

to the Taylor-Goldstein's equation

$$\left(\frac{d^2}{dy^2} - k^2\right)\widehat{\psi} = -\frac{G_y}{(y-c)^2}\widehat{\psi}. \tag{3.33}$$

The main purpose of this work is to study resonances between internal waves in a highly layered fluid ($M > 2$). For this reason we ease the linear analysis considering the broken line profile (3.8). To investigate the possible effects on waves instability due to interfaces thickness d, we study the case $M = 2$ (see A.1.2) assuming the piecewise-linear profile (3.9). By the matched asymptotic expansion we simplify the governing equations to (3.22)-(3.24) and in §3.4.1 we obtain an explicit dispersion relation that predicts the stability of wave perturbations in the defect theory limit. We use this integral equation to predict the formation of instabilities in our numerical simulations where we consider $M = 4$ smooth interfaces (3.10).

We can turn the Taylor-Goldstein equation into an integral equation by using the Green's function of the left-hand side of (3.33). We may rewrite the Taylor-Goldstein equation as $\mathcal{L}\widehat{\psi}(y) = \mathcal{G}$ for that the associated homogeneous problem $\mathcal{L}\widehat{\psi} = \delta(y-\xi)$ has solution

$$g(y,\xi) = -\frac{1}{2k}e^{-k|y-\xi|}. \tag{3.34}$$

The general solution is then given by Green's function

$$\widehat{\psi}(y) = \int_{-\infty}^{+\infty} \mathcal{G}(\xi)g(y,\xi)d\xi = \frac{1}{2k}\int_{-\infty}^{+\infty} \frac{G_y(\xi)\widehat{\psi}(\xi)}{(\xi-c)^2}e^{-k|y-\xi|}d\xi, \tag{3.35}$$

where the integrand depends on the equilibrium buoyancy profile and the vertical stream-function itself. Assuming the interfaces being sharp (3.8) we can turn the equation to a matrix eigenvalue problem in c where the eigenvector is the set of M values of $\widehat{\psi}(y)$ on each interface. We define $K = 2k/J$, $l = 2j+1$, $\epsilon = e^{-2k}$, $\Psi_y = \widehat{\psi}(y)/(y-c)^2$ and in order to find the unknowns Ψ_l we compute (3.35) on every interface l' obtaining the following set of M linear equations in Ψ_l

$$K(l'-c)^2\Psi_{l'} = \sum_{l=1,\text{odd}}^{M-1}\left(\Psi_l\epsilon^{\frac{|l'-l|}{2}} + \Psi_{-l}\epsilon^{\frac{|l'+l|}{2}}\right), \tag{3.36}$$

$$l' = -M+1, \text{ odd}, M-1.$$

If we denote the matrix of coefficients of the Ψ_j's by $\mathscr{G}_M$, the dispersion relation is given by $D_M(c,J,k) = \det(\mathscr{G}_M) = 0$, which is a polynomial of order $2M$ in c.

Defect theory

Under the approximations of the defect theory we may reduce the linear stability problem to a simplified and explicit dispersion relation. We consider the wave perturbations of the basic states

$$Z = z(\eta)e^{ik(x-ct)},\ B = b(\eta)e^{ik(x-ct)},\ \Phi = a\,e^{ik(x-ct)} \tag{3.37}$$

and injecting them in the linear instance of (3.23) and (3.24), we obtain

$$z = -\frac{aG_\eta}{(\eta-c)^2}, \qquad b = -\frac{aG_\eta}{\eta-c}. \tag{3.38}$$

By substituting them into (3.22) we get the dispersion relation

$$2k - \int_{-\infty}^{+\infty} \frac{G_\eta}{(\eta-c)^2}\,d\eta = 0, \tag{3.39}$$

for that, provided a particular staircase $G_\eta(\eta)$, it is possible to solve algebraically (as in the case of sharp interfaces) or numerically (as in the case of smooth interfaces) the dispersion relation.

3.4.2 Taylor-Caulfield instability: a review

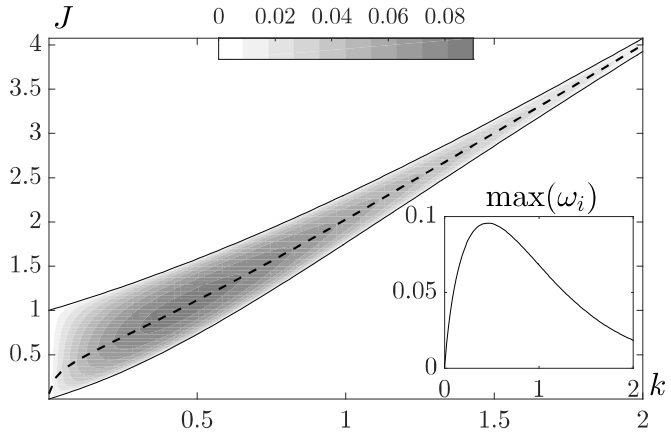

Figure 3.2: Dispersion relation $\omega(k, J)$ for $M = 2$ sharp density interfaces. The grey region shows levels of growth rate ω. The solid lines are the marginal stability curves for TCI and the dashed line shows the position of maximum growth. In the inset it is shown the growth rate ω along the dashed line.

When $M = 2$ the linear system of equations (3.36) reduces to

$$\begin{Vmatrix} K(1-c)^2-1 & -\epsilon \\ -\epsilon & K(1+c)^2-1 \end{Vmatrix} \begin{Vmatrix} \Psi_1 \\ \Psi_{-1} \end{Vmatrix} = \begin{Vmatrix} 0 \\ 0 \end{Vmatrix} \tag{3.40}$$

and its characteristic polynomial provides the dispersion relation we seek

$$D_2(c,J,k) = c^4 - \left(\frac{J}{k}+2\right)c^2 + \frac{J^2}{4k^2}\left(1-\epsilon^2\right) - \left(\frac{J}{k}-1\right) = 0. \tag{3.41}$$

For $c_r = 0$ we find the marginal stability curves

$$J_{\mp} = \frac{2k}{1 \mp \epsilon}, \tag{3.42}$$

that are showed in figure 3.2 as solid lines. For $k \gg 1$, we find that the asymptotic behavior of the boundaries is $J \sim 2k$. The implicit function theorem let us to find the set of points (J,k) in which c_i is maximum

$$\frac{\partial c}{\partial J} = -\frac{D_J}{D_c} = 0, \tag{3.43}$$

that is

$$c^2 = \frac{J}{2k}\left(1-\epsilon^2\right) - 1. \tag{3.44}$$

Substituting this into (3.41) we find the set of points in which c_i is maximum

$$J = 4k\frac{\sqrt{1-\epsilon^2} - (1-\epsilon^2)}{\epsilon^2(1-\epsilon^2)}, \tag{3.45}$$

showed as a dashed line in figure 3.2 while the inset shows the growth rate along this line.

3.4.3 Multiple interfaces

From (3.36) we can write the linear equations system as $\mathscr{G}_M \mathbf{X}^T = \mathbf{0}$, where $\mathscr{G}_M$ is the coefficients matrix for M interfaces - e.g.

$$\mathscr{G}_4 = \left\| \begin{array}{cccc} K(3-c)^2-1 & -\epsilon & -\epsilon^2 & -\epsilon^3 \\ -\epsilon & K(1-c)^2-1 & -\epsilon & -\epsilon^2 \\ -\epsilon^2 & -\epsilon & K(1+c)^2-1 & -\epsilon \\ -\epsilon^3 & -\epsilon^2 & -\epsilon & K(3+c)^2-1 \end{array} \right\| \tag{3.46}$$

is the matrix of a system with $M = 4$ interfaces. The vector of unknown values of the stream-function at the interfaces position is $\mathbf{X} = \|\Psi_{M-1}\, \Psi_{M-3}\, \ldots\, \Psi_1\, \Psi_{-1}\, \ldots\, \Psi_{-M+3}\, \Psi_{-M+1}\|$.

In the limit of large wave numbers the off-diagonal elements of $\mathscr{G}_M$ are negligible, which means that the vorticity of internal gravity waves fades quickly away from any interface and thus the waves weakly overlap. This reduces the matrix problem to a product of the diagonal terms,

$$\prod_{j=-M/2}^{M/2-1}\left[\frac{2k}{J}\Big(2j+1-c\Big)^2 - 1\right] = 0, \tag{3.47}$$

which implies phase velocities $c_r = 2j + 1 \pm \sqrt{J/2k}$. We now look for waves with equal phase speed after being doppler shifted in opposite directions: when $J = 2k$ we find the first phase-locking which occurs for nearest-neighbor interfaces; the associated phase speeds are $c_r = 0, \pm 2, \pm 4, \ldots, \pm(M-2)$. A larger J unlocks the next-nearest-neighbor resonances when $J = 8k$ giving $c_r = \pm 1, \pm 3, \ldots, \pm(M-3)$. Third-nearest-neighbor resonances are activated when $J = 18k$, where waves drifting at $c_r = 0, \pm 2, \pm 4, \ldots, \pm(M-4)$ become unstable. The repeating structure of the resonances is now evidenced and indicates how to relate the Richardson number to the "order" r of the interaction, defined such that $r = 1$ signifies nearest-neighbor interactions, next-nearest-neighbor interactions have $r = 2$, and so on. Evidently, $J = 2r^2k$, which provides the $k \gg 1$ asymptotes of the instability bands.

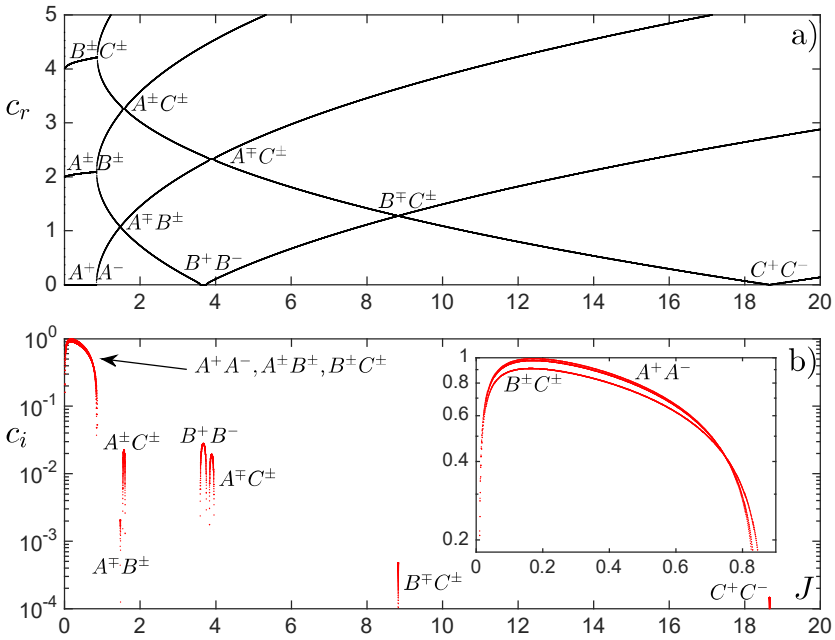

Figure 3.3: Eigenvalues $c = c_r + i\,c_i$ of the Taylor-Goldstein equation. Here $M = 6$ sharp interfaces are perturbed with a fundamental mode of $k = 0.01$. Panel a) shows the real and b) the imaginary part of c as function of the Richardson number J. The markers $A^{\pm}$, $B^{\pm}$ and $C^{\pm}$ names the interfaces at $y = \pm 1$, ± 3 and ± 5 respectively. The resonance between two interfaces is given by a couple of letters, thus $A^{-}B^{+}$ is the interaction between waves in $y = -1$ and $y = 3$.

For lower wavenumber, the vertical decay of the internal gravity waves is slower and the off-diagonal elements of $\mathscr{G}_M$ become important. In figure 3.3 we cut the plane (J, k) at $k = 0.01$ and show the dependence of c on J. We mark by $A^{\pm}$ the interfaces in $y = \pm 1$,

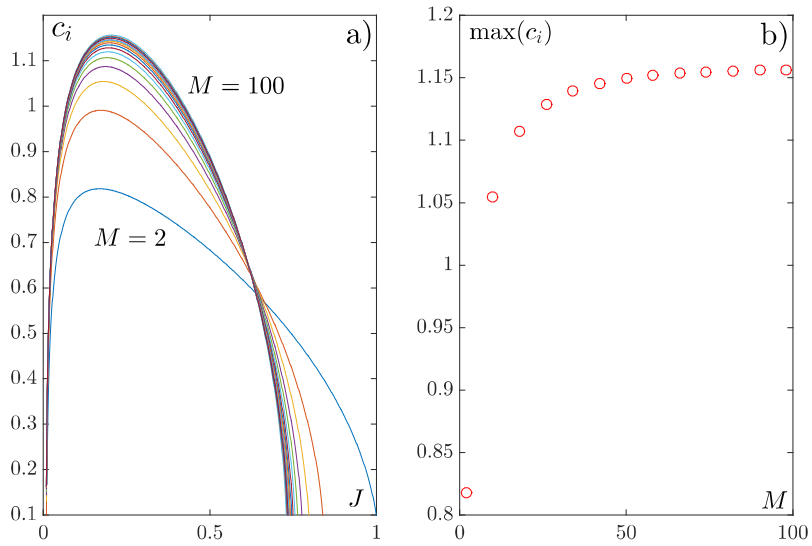

Figure 3.4: In panel a) we show $c_i = \omega_i/k$, where $k = 0.01$, of the most unstable phase velocity $c_r = 0$ for increasing number of interfaces M and in panel b) we show $\max(c_i)$ as function of M.

$B^{\pm}$ in $y = \pm 3$ and $C^{\pm}$ the ones in $y = \pm 5$ - we made this figure assuming the flow to have six interfaces. As we observed in the limit $k \gg 1$, the first waves to interact are the adjacent ones, and then stronger stratifications allow resonances between interfaces more and more distant. In panel a) we see that the unstable velocities are not strictly the mean shear velocities of the resonating interfaces, but vary with J. In panel b) we show the growth rates $c_i = \omega_i/k$ for the 15 unstable resonances. The most unstable waves comes from nearest-neighbor interfaces interactions. Among these the most effective instabilities are related to core layers interactions - see inset of panel b) - and the strongest one is due to the interaction A^+A^-, for which $c_r = 0$. In figure 3.4a we show how the growth rate of this instability is affected by the total number of interfaces. As M increases the instability band become small, but the fastest growing mode reach a saturation in its possible growth - as it is shown in panel b).

A clearer idea upon the dependence of the unstable bands on M and k comes from figure 3.5. Here we compare the case of $M = 2$ to $M = 4$ and 6. As we see, and already pointed out from the $k \gg 1$ limit, these bands follow the asymptotes $J = 2r^2k$. The more interfaces in the fluid the more unstable bands we get: 6 for $M = 4$, and 15 when $M = 6$. In the latter case, we show in the right panel of figure 3.5 the maximum growth rate inside each of these 15 bands. Every different symbol, marks a different r, going from the most unstable

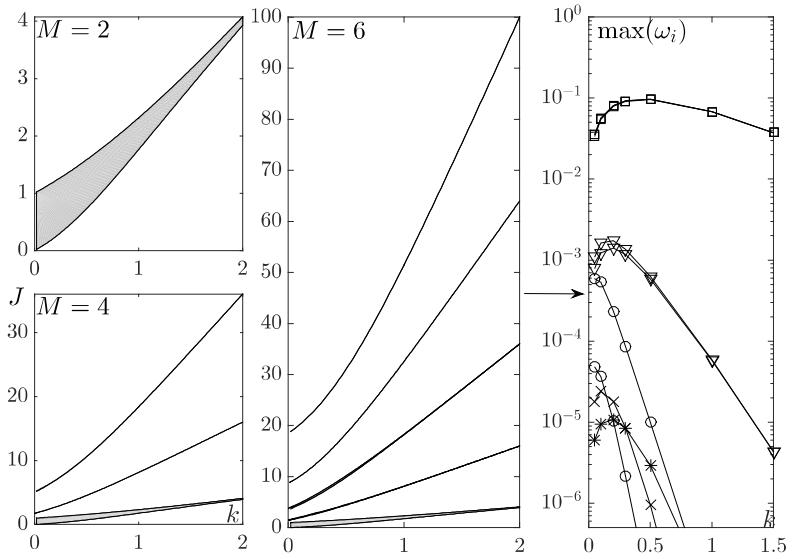

Figure 3.5: Dispersion relation $\omega_M(k, J)$ for M =2, 4 and 6 sharp interfaces. The solid lines are the marginal stability boundaries for Taylor-Caulfield instabilities and the gray shaded regions are where the unstable modes lies. The right panel shows the maximum growth rate of unstable waves when $M = 6$. Growth rates are labelled as follow: ($\square$) is the resonance A^+A^-, $A^\pm B^\pm$ and $B^\pm C^\pm$; ($\bigcirc$) is $A^\pm C^\pm$ and $A^\mp B^\pm$; ($\bigtriangledown$) is B^+B^- and $A^\mp C^\pm$; ($\times$) is $B^\mp C^\pm$; ($*$) is C^+C^-.

($r = 1$) waves to the slowest ($r = 5$). We would like remark that equal phase velocities arising from different interfaces are related to different unstable bands, e.g. interfaces at $y = \pm 1$ or $y = \pm 3$ have the same resonant velocity ($c_r = 0$), but having different r place them on different portions of the (J, k) plane.

Long-wavelength approximation

We consider the limits $k, J << 1$ with $J = O(k)$, for which the Taylor-Goldstein equation becomes

$$\psi'' = -\frac{G_y}{(y-c)^2}\psi, \tag{3.48}$$

where $G_y = kG_1(y)$. From the dispersion relation (3.39) and assuming a number M of sharp interfaces $G_y = J\sum_{j=0}^{M/2-1}[\delta(y-2j-1)+\delta(y+2j+1)]$ we obtain

$$\frac{k}{J} = \sum_{j=0}^{M/2-1} \frac{l^2+c^2}{(l^2-c^2)^2}, \tag{3.49}$$

where $l = 2j+1$. In figure 3.6a we can see the graph of the right hand side of (3.49), as function of c^2, in the case of four density interface. There are three different regions of k/J:

one over the intercept $k/J = 10/9$, one below the local minimum near $c_r = 2$ and the region between these two points. Above the intercept, k/J has four distinct real roots, thus c has

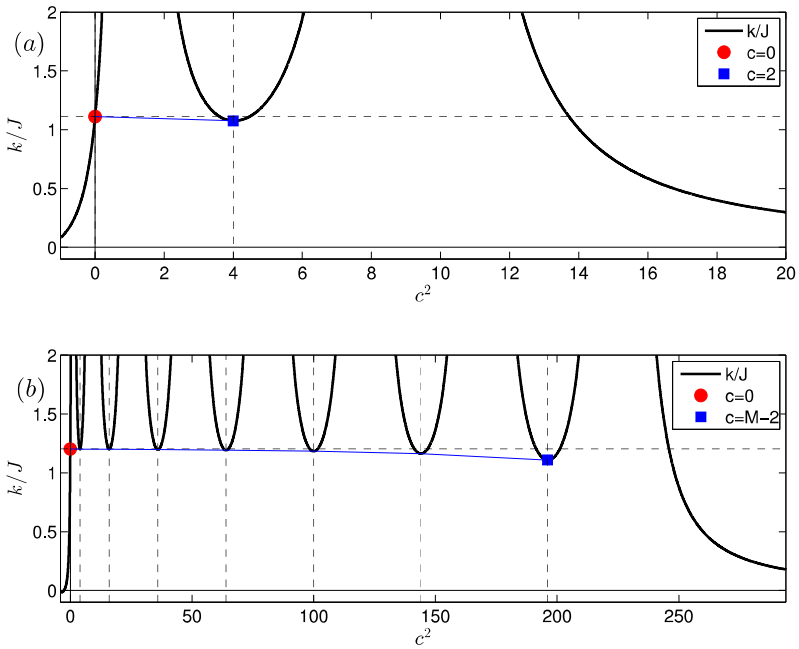

Figure 3.6: Representation of the dispersion relation (3.49). In panel a) we show the case of $M = 4$ and $M = 16$ is in panel b). Solid lines shows $k/J(c^2)$, the red solid dot shows the first mode to become unstable, and blue solid square the last. The thin solid line connects these two points and go through the local minima in $c^2 = (2j)^2$, $j = 0, 1, 2, \ldots, M-2$.

four positive and four negative roots. Increasing the Richardson number - thus lowering k/J - the innermost root get closer to zero and when it crosses this value, two phase velocities become imaginary. Those roots represent two standing waves that exponentially grow and decay. The other real roots are drifting waves that neither grow nor decay. Moving to larger J the next modes to lose their stability are the four nearby $c_r^2 = 4$ - they lose their marginal stability. Two of them are unstable while two are stable.

What happens if we increase the number of interfaces? First of all we analyze how the intercept point varies according to M. Equation 3.49 for $c_r = 0$ becomes

$$\frac{k}{J} = \sum_{j=0}^{M/2-1} \frac{1}{l^2}, \tag{3.50}$$

For $M = 2$ we have $J = k$ that is the limit $k \ll 1$ in equation (3.42). When $M = 4$ the value for which the first modes destabilize lowers to $J = 9k/10$. We can calculate by hand the intercept for each M, but we show that the critical value for which J destabilize the

waves reach a lower bound for $M \to \infty$, see figure 3.7. We use the Dilogarithm function to evaluate the sum. We begin from the Taylor expansions

$$-\log(1-x) = x + \frac{x^2}{2} + \frac{x^3}{3} + O(x^4),$$

$$-\log(1+x) = -x + \frac{x^2}{2} - \frac{x^3}{3} + O(x^4)$$

and dividing both expansion by x, subtracting the second from the first and integrating this equation, we get

$$-\int_0^x \frac{\log(1-x')}{x'}dx' + \int_0^x \frac{\log(1+x')}{x'}dx' = 2\sum_{j=0}^{\infty}\frac{x^l}{l^2}, \tag{3.51}$$

where $l = 2j+1$. On the left hand side there are the Dilogarithm functions, $Li_2(x)$ and $-Li_2(-x)$ respectively. If we evaluate these functions in $x = 1$ we find that $Li_2(1) = \pi^2/6$ and $-Li_2(-1) = \pi^2/12$. Combining these results with (3.51) we find

$$\frac{k}{J} = \sum_{j=0}^{\infty}\frac{1}{l^2} = \frac{\pi^2}{8}, \tag{3.52}$$

or $J = 8k/\pi^2$, thus as M increases no waves could become unstable as soon as the Richardson number is below this value.

Now let's see what happens for the others minima. There is one of them between every interval $[(2j+1)^2, (2j+3)^2]$. We suppose that the position of the minimum c^2_{min} is mainly given by the terms $2j-1$ and $2j+1$ in the series. Taking the derivative in c^2 of these two terms end equating to zero, we still find a full 4th order polynomial. For the moment we assume that the number of interfaces is large, then if $j \gg 1$ we find the polynomial

$$(12j^2 + c^2)(4j^2 - c^2)^3 = 0 \tag{3.53}$$

with real roots in $c^2 = 4j^2$, which means that the minima are the mean velocities between two adjacent interfaces as we saw in (3.36) taking the limit $k \gg 1$. This result is valid for large j, but from figure 3.6 it seems to be good for small j also, the error is less than 1%.

In figure 3.7 we can see, for increasing number of interfaces, the slope of the marginal stability line departing from $k = 0$ of first and last unstable mode. We already know that the limit value for $c_r = 0$ is $8/\pi^2$. For the last unstable mode we evaluated numerically the value in $c_r = M - 2$ finding that $J/k = 0.8954$. This means that also for $M \to \infty$ the last marginal stability curve has a finite slope.

To summarize the informations given by the defect theory about discontinuous interfaces, we could say that whatever M is, the Richardson number should be bigger that $8/\pi^2$ to allow $c_r = 0$, the most unstable mode, to become unstable. On the other hand, the last unstable mode has a threshold to become unstable that is found numerically and is $J/k = 0.8954$.

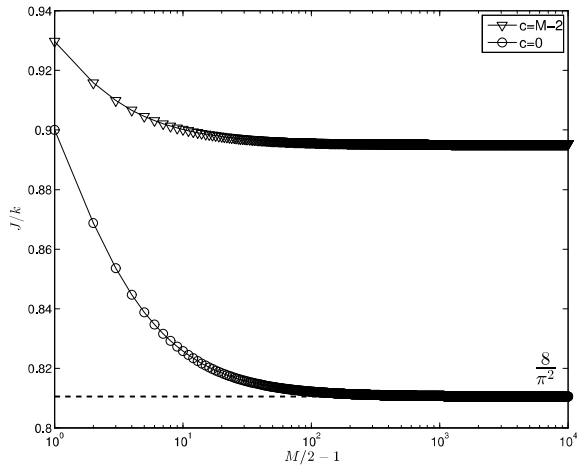

Figure 3.7: Position, in terms of J/k, for the most and least unstable mode as a function of M. Circles represent the intercept value of J/k for $c^2 = 0$ and triangles are the local minimum values for $c^2 = (M-2)^2$. The dashed line shows the asymptote for $M \to \infty$, see (3.52).

Smooth interfaces

Here we analyze the dispersion relation (3.39) when the staircase is characterized by the series of smooth interfaces (3.10). The thickness d regulates the onset of instabilities and their growth rate as we can see in figure 3.8. We report the growth rate of unstable perturbation together with the marginal stable Richardson number $\bar{J}(c, d)$. The case of $M = 2$ interfaces which supports the formation of TCI have been widely studied under the defect approximation in Balmforth et al. (2012) and here we focus on the dependence of the critical Richardson number on c_i and d. From figure 3.8a we observe the growth rate to be smaller for increasing d, while $\bar{J}(0, d)$ is a non-monotonous function of d. Indeed it decreases until $d < 0.38$ and then grows again becoming bigger than $\bar{J}(0, 0)$ eventually (see 3.8c, red line). If we consider two more interfaces in $\eta = \pm 3$ more instabilities may arise. In this case the possible unstable waves are $c_r = 0$ and $c_r = \pm 2$. As we can see in figure 3.8b they don't really affect the linear growth and the dependence on d, except from the

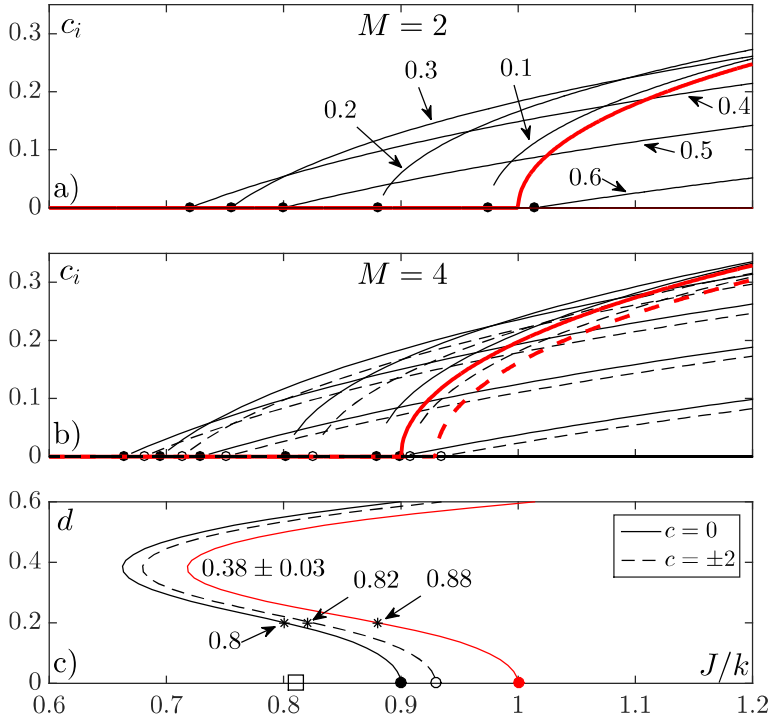

Figure 3.8: Dispersion relation for a staircase density profile of smooth (3.10) interfaces placed in $\eta = \pm 1, \pm 3, \ldots, M-1$. In panel a) and b) we show the growth rate $c_i = \omega/k$ as a function of J/k for different values of the interfaces thickness d, where $M = 2$ is in a) and $M = 4$ in b). The solid lines refers to modes with phase velocity $c_r = 0$ and the dashed lines to $c_r = \pm 2$. The two thick lines refer to the broken-line profile while (d) marks the critical values $\bar{J}(0, d)$ and $(\circ)$ marks $\bar{J}(2, d)$. In panel c) we show these two functions for $M = 4$, black lines, and $M = 2$ (red line). The square is the asymptote $J/k = 8/\pi^2$, see (3.52).

fact that they become unstable at a smaller $\bar{J}(c, d)$. Moreover we notice that we have a growth rate and a marginal stable Richardson number for each phase with $c_r = 0$ being more unstable than the outer phase velocities. We remark the fact that when $c_r = \pm 2$ the results of the linear analysis overlap because of symmetry properties of the problem.

3.4.4 The viscous and diffusive problem

Viscosity can alter the instability of normal mode perturbations of the basic state and here we address this problem by considering $\nu, \kappa > 0$. We consider the perturbations in (3.37), i.e. $[Z, B, \Phi] = [z(\eta), b(\eta), a] \exp ik(x - ct)$, and inject them into (3.22), (3.23) and (3.24)

and by keeping the linear, viscous and diffusive terms we get

$$\nu z_{\eta\eta} - ik(\eta - c)z = -ikb, \tag{3.54}$$

$$\kappa b_{\eta\eta} - ik(\eta - c)b = -\frac{iG_\eta}{2}\int_{-\infty}^{+\infty} z(\eta')d\eta', \tag{3.55}$$

where

$$a = -\frac{1}{2k}\int_{-\infty}^{+\infty} z(\eta')\,d\eta'. \tag{3.56}$$

Fourier transforming these equations allows to reduce this second order ODE problem to the first order ODE system

$$\frac{d\widehat{z}}{dq} - \left(\frac{q^2\nu}{k} - ic\right)\widehat{z} = -i\widehat{b}, \tag{3.57}$$

$$\frac{d\widehat{b}}{dq} - \left(\frac{q^2\kappa}{k} - ic\right)\widehat{b} = \frac{\pi q}{k}\widehat{z}(0)\widehat{G}. \tag{3.58}$$

The equation in $\widehat{b}(q)$ do not depend on $\widehat{z}(q)$ and has solution

$$\widehat{b}(q) = -\frac{\pi}{k}\widehat{z}(0)e^{\frac{q^3\kappa}{3k} - icq}\int_q^{+\infty} d\widetilde{q}\ \widetilde{q}\,\widehat{G}(\widetilde{q})\,e^{-\frac{\widetilde{q}^3\kappa}{3k} + ic\widetilde{q}}, \tag{3.59}$$

whilst (3.57) depends on $\widehat{b}$ and has solution

$$\widehat{z}(q) = -i\frac{\pi}{k}\widehat{z}(0)e^{\frac{q^3\nu}{3k} - icq}\int_q^{+\infty} d\widetilde{q}\ e^{-\frac{\widetilde{q}^3(\nu-\kappa)}{3k}}\int_{\widetilde{q}}^{+\infty} d\breve{q}\ \breve{q}\widehat{G}(\breve{q})\,e^{-\frac{\breve{q}^3\kappa}{3k} + ic\breve{q}} \tag{3.60}$$

where we injected solution (3.59) into it. The dispersion relation is found by fixing $q = 0$ in the last equation, that is

$$0 = D_{\nu,\kappa}(c,k,J) = 1 + i\frac{\pi}{k}\int_0^{+\infty} d\widetilde{q}\ e^{-\frac{\widetilde{q}^3(\nu-\kappa)}{3k}}\int_{\widetilde{q}}^{+\infty} d\breve{q}\ \breve{q}\widehat{G}(\breve{q})\,e^{-\frac{\breve{q}^3\kappa}{3k} + ic\breve{q}}. \tag{3.61}$$

which gives us informations on the dependence of the eigenvalue c upon k and J for some fixed ν and κ. Throughout this work we focus on the case $\nu = \kappa$, for that the dispersion relations reduces to

$$0 = D_\nu(c,k,J) = 1 + \frac{\pi}{k}\int_0^{+\infty} d\widetilde{q}\ \widetilde{q}\,\widehat{G_\eta}(\widetilde{q})\,e^{-\frac{\widetilde{q}^3\nu}{3k} + ic\widetilde{q}}, \tag{3.62}$$

which we solve numerically using a Newton roots finder algorithm. We fix k and J and expand with a Taylor series $0 = D(c) \approx D(c_g) + D'(c_g)\delta c$ from an initial phase velocity

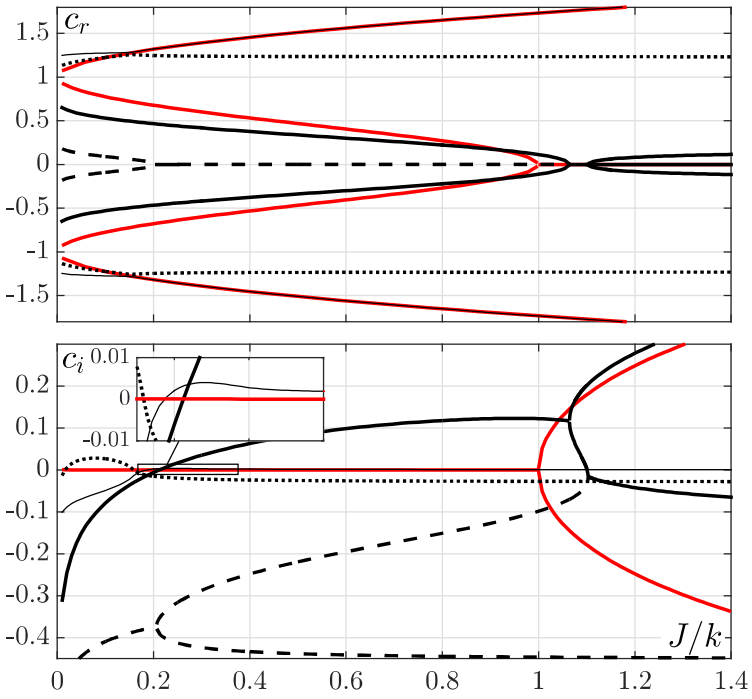

Figure 3.9: Linear stability of viscous modes in a three layers fluid. We consider two configurations where the interfaces have thickness $d = 0$ and fluid viscosity $\nu = 0$(red lines) $\nu = 0.005$(black lines). In the top panel we show the phase velocity c_r and in the bottom panel the imaginary part. The different stiles of the black lines serve only to mark together the lines in the two panels: e.g. the dashed line in the top panel is a phase velocity with the imaginary component given by the dashed line in the lower panel.

c_g. From the expansion we refine the guess by $c_g^{new} = c_g + \delta c$ and than by iterating this algorithm until $|\delta c|$ is bigger than some error gives us the eigenvalue c.

To avoid complications due to waves interactions among a multilayer system, we consider a piecewise-constant three layers stratified fluid. From our computations we observe that when $\nu < 0.001$, viscosity has a negligible impact on the eigenvalues, which are given by the red lines in figure 3.9. In this case what happen is that when J/k is small, four waves propagates at $c_r \approx \pm 1$. These waves are marginally stable and for increasing J/k propagate at velocities diverging from ± 1. When we increase k two waves move at $|c_r| > 1$, while the other two are slower ($|c_r| < 1$) until, for a big enough J/k, both reach the common velocity $c_r = 0$. At this point, while the fast moving waves are stil marginally stable, the resonating waves become one stable and one unstable. This is the scenario we already explained in

§3.4.2.

Having a viscous fluid add some significative variations to the eigenvalues structure: more phase velocities are available, more unstable waves appear. Some of them become unstable without resonating with other waves. When $\nu = 0.005$ we observe eight modes which are symmetric in c_r. The modes at $|c_r| > 1$ that are always marginally stable when $\nu = 0$, become four (thin solid and bold dotted lines in figure 3.9). The dotted lines modes can be unstable for small J/k, while the thin solid line modes become unstable for slightly higher J/k (see inset in figure 3.9). As we may see from the figure, these four modes never resonates with other modes. The two modes that in the inviscid case counter-propagate until they resonate, are now stable for small J/k and become unstable for big enough values of the parameter. When they phase lock, produce two unstable waves, one of which persists for bigger J/k, whilst the other resonates with the wave shown as dashed line in figure 3.9. This are two viscosity induced modes which are always stable. One of the two eventually decays at a rate so small that resonate with another mode (bold solid line) producing two stable modes.

3.5 Weakly nonlinear analysis

This section is devoted to the analytical study of the region nearby the onset of instabilities in the density staircase when internal gravity waves are Doppler-shifted by a background linear shear. The onset of instabilities is inside the domain of the defect approximation, thus we take advantage of the approximations that led the governing equations to the simplified system (3.25) and (3.26) and assume the fluid to be inviscid and non-diffusive. We focus on slow timescales $T = \varepsilon t$, which allows the time derivative of $\mathscr{Z}(x, \eta, t)$ to be of the same order of the vertical advection term $\Phi_x \mathscr{Z}_\eta$, and redefine the equations in the moving frame of reference $\widetilde{x} = x - ct$. Expanding $\mathscr{Z}(x, \eta, t)$, $G_\eta(\eta)$, $\Phi(x, t)$ and J to a pawer series in ε, we obtain a set of equations for each order in ε. By solving them subsequently (see Appendix A.2 for a detailed computation) we eventually obtain the amplitude equation

$$A_{TT} = \frac{I}{I_3} A + \frac{I_3^2 + 2I_5}{4I_3} |A|^2 A, \tag{3.63}$$

being $A(T)$ the amplitude of the leading order streamfunction inside the defect $\Phi(\tilde{x}, t) = A(T)e^{i\tilde{x}} + c.c.$. The quantities I_3, I_5 and I depend on the shape of the staircase. As an example we consider the case of four sharp interfaces for which these coefficients are

$I_3/\bar{J}(c) = 164/27$, $I_5/\bar{J}(c) = 7300/729$ and $I = 20J_2/9$. The quantities $\bar{J}(c)$ and J_2 are respectively the bifurcation point relative to one of the unstable phase velocities $c_r = 0$ or ± 2 and the $O(\varepsilon^2)$ term in the expansion of J. The secular solution of (3.63) is

$$|A| = \sqrt{-\frac{I}{I_3^2 + 2I_5}}, \tag{3.64}$$

which simultaneously provides a condition on J_2: to keep the solution real, J_2 must be negative. This means that the bifurcation is subcritical as is shown with dashed lines in the top panel of figure 3.13 and confirmed by numerical simulations of a nearly inviscid fluid.

3.6 Numerical analysis

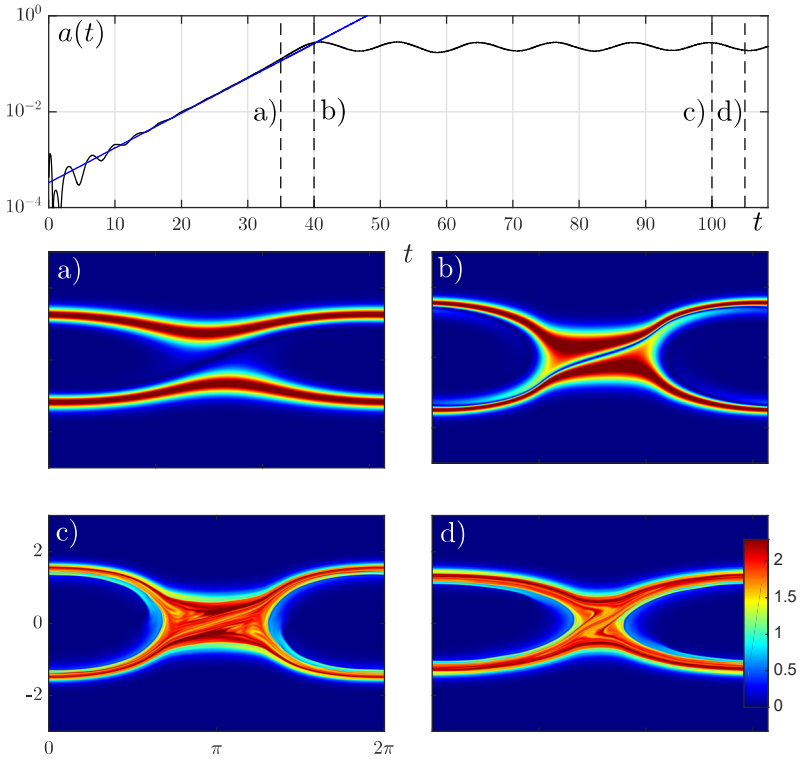

Figure 3.10: Numerical solution of (3.25)-(3.26) for smooth interfaces placed in $\eta = \pm 1$. Here $Pr = 1$, $J = 1$, $\nu = 10^{-6}$ and $c = i\,0.167$. In the top panel we report $a(t)$ and compare it to the linear growth of the unstable mode $k = 1$. The dashed lines mark the times at which the snapshots below have been taken

In this section we present the numerical simulations of the multiple density layers fluid with a linear background shear. Although most of our results relates to the linear analysis

of the full equation system (3.5) and (3.6), we solve numerically the flow under the defect approximation introduced in §3.3, therefore the layers are confined into a horizontal defect such that it is possible to simplify the governing equations to the system (3.25) and (3.26). This assumption prevents the fluid to develop long distance instabilities ($r > 1$), indeed assuming $k \ll 1$ only nearest-neighbor waves are unstable as we found in 3.4.3. Assuming these simplifications is a good starting point in our numerical studies since the linear stability analysis shows that among all these possible instabilities these are the strongest.

We briefly show the development of a Taylor-Caulfield billow to show which are the main phases of its nonlinear formation. For this purpose we consider the case of TCI ($M = 2$) which have been studied numerically in Lee and Caulfield (2001) for the full equations setup and in Balmforth et al. (2012) under the long wave approximation we consider here. In the limit of inviscid and piecewise-constant layers the bifurcation from the basic state is subcritical, while big enough d or ν can shift the bifurcation point and make it supercritical. As it has been shown in Balmforth et al. (2012), when the viscosity and interface thickness are $\nu = 10^{-6}$ and $d = 0.2$ the subcritical nature of the bifurcation is still preserved. In figure 3.10 we show a numerical simulation of such configuration, where the Richardson number is big enough to make the mode $k = 1$ unstable. We choose $J = 1$ which is larger than the critical value $\bar{J}(0, 0.2) = 0.88$, see figure 3.8c at the level $d = 0.2$. When $J = 1$ the relative growth rate is $\omega_i = 0.167$. We perturb the basic profile using i_1 with $A_0 = 0.01$ - see (3.29) - and if we compare the expected exponential growth to the temporal evolution of $a(t)$ we see in the top panel of figure 3.10 that the two lines match during initial phase of growth of the TCI. In this phase the interfaces twist and move towards each other (see figure 3.10a). Than the nonlinear growth makes the two interfaces to merge in a localized region (see figure 3.10b) producing an elliptical billow which is embedded by vorticity filaments - see panel c) and d). The second-stage evolution of the billow is then regulated by viscosity that can prevent the formation of secondary instabilities and eventually slowly decays the nonlinear state.

Now we want to study the interplaying influence of a multi-layered fluid where $M > 2$. For this purpose we add two interfaces in $\eta = \pm 3$. We remind to the reader that the defect approximation allows the interaction between nearest-neighbor interfaces only, as have been discussed in §3.4.3. The available phase velocities are $c_r = 0$ and ± 2, which are due to interactions A^+A^- and $A^\pm B^\pm$, whilst interactions $A^\pm B^\mp$ and B^+B^- ($r > 1$) are

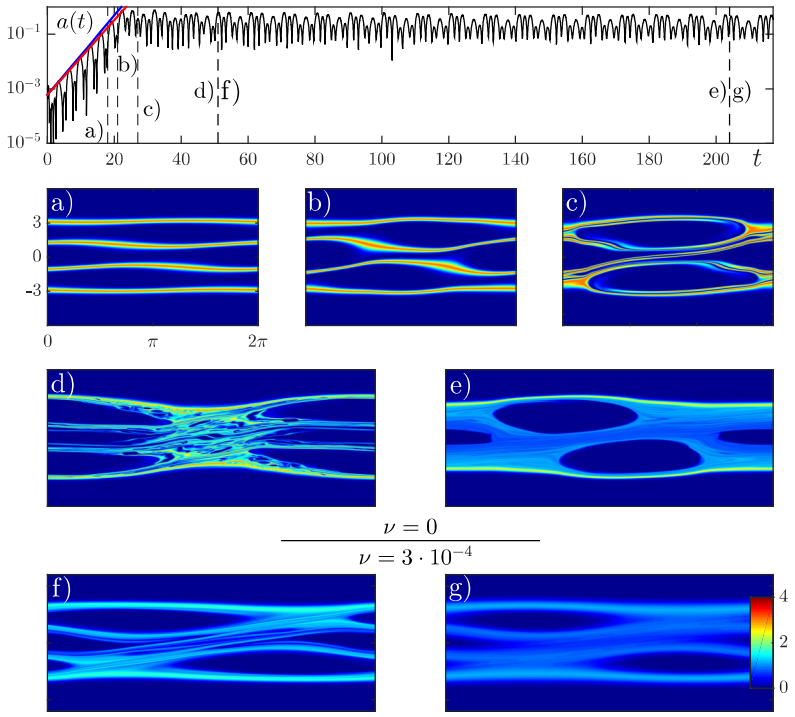

Figure 3.11: We show the nonlinear evolution of a perturbed $M = 4$ interfaces fluid. Each interface is smooth with $d = 0.2$. The cases of inviscid fluid is shown in panels a)-e). The Richardson number is $J = 1.2$ which allow internal gravity waves with $c_r = -2$, 0 and 2 to be unstable. In the top panel we report $a(t)$, the linear growth of $c_r = 0$ (blue) and $c_r = \pm 2$ (red) and the dashed lines are where the snapshots in the panels below have been taken. In panel f) and g) we show the effect of $\nu = 3 \cdot 10^{-4}$ on the long-time behaviour of the solution.

forbidden. As well as for the case $M = 2$, we show in figure 3.11 numerical simulations for $M = 4$ interfaces of thickness $d = 0.2$ for an inviscid fluid. We perturb the basic state with i_1 where $A_0 = 0.01$. This initial perturbation excites $k = 1$ but do not provide any specific phase velocity. Indeed we pick $J = 1.2$ where, from figure 3.8b, we know that both $c_r = 0$ and ± 2 are unstable with growth rates $\omega_0 = 0.3353$ and $\omega_{\pm 2} = 0.3156$. These are compared to $a(t)$ in the top panel of figure 3.11. The two growth rates are similar and because of the oscillations of $a(t)$ it is difficult to understand which one dominates. As we have seen for $M = 2$, the interfaces twist toward each other (see figure 3.11b) and form three billows: a stationary one in the middle layer and two in the outer layers that counter propagate at $c_r = \pm 2$ (see figure 3.11c). In the second stage evolution the vorticity filaments that embeds the three billows suffer secondary instabilities (see figure 3.11d). Turbulent parasitic billows

forms and have the effect of mixing evenly the defect layer leaving three sharp "holes" in the mixing layer (see figure 3.11e). In contrast to the inviscid case, in figure 3.11f and 3.11g we show two snapshots of the numerical solution when the fluid has viscosity $\nu = 3 \cdot 10^{-4}$. The early stage evolution is not affected by the viscosity, but eventually vorticity filaments are diffused before they undergo secondary instabilities. Over long timescales diffusion affects first the central billow, which is diffused in the mixing layer and then the whole nonlinear state decays slowly to a single mixing layer of nearly constant density stratification.

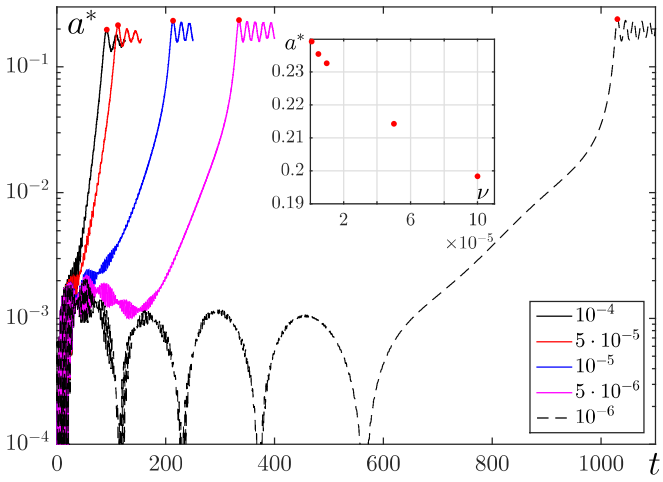

Figure 3.12: We show $a(t)$ for the initial value problem (3.29) for $M = 4$ smooth interfaces of thickness $\delta = 0.2$. The Richardson number is $J = 0.8$ and we consider the viscosities reported in the legend. In the inset we see how ν controls the saturation maximum a^*.

We want to numerically unveil the region near the bifurcation points of a wave with $k = 1$ and phase velocity $c_r = 0$ and ± 2. In §3.4.3 we assumed the fluid to be inviscid and find out - see figure 3.8 - that the critical Richardson numbers relative to the available unstable phase velocities are $\bar{J}(0, 0.2) = 0.8$ and $\bar{J}(\pm 2, 0.2) = 0.82$. We also observed in §3.4.4 the triggering effect of viscosity on the stability problem. In that section we considered sharp interfaces and observed that viscosity has negligible effects on the stability of internal gravity waves until $\nu \leq 10^{-3}$. After this threshold it abruptly changes the linear stability scenario allowing wave-resonant instabilities as well as unstable resonant-free waves. For numerical purposes we consider $d = 0.2$, therefore we must be careful on the choice of ν in order to guarantee the bifurcation to remain subcritical. For this reason we do a qualitative survey on the effect of ν on the critical Richardson numbers found in the inviscid fluid stability analysis, see §3.4.3. These points have been found assuming the fluid to be inviscid and,

as it has been pointed out in Balmforth et al. (2012), ν can shift their position and make them subcritical or supercritical. For this reason we fix the Richardson number close to $\bar{J}(0, 0.2)$ and vary ν in the range $10^{-6} < \nu < 10^{-4}$. In figure 3.12 we see that when $\nu = 10^{-6}$ the solution is subcritical, but a viscosity five times bigger makes it supercritical. Thus we choose $\nu = 10^{-6}$ as a big enough viscosity that still preserves the subcritical nature of the inviscid bifurcation, such that we can rely on the analysis we did in §3.4.3.

Linear stability analysis in 3.4 gave us many informations about the critical points of bifurcation. We studied how are affected by the number of interfaces and physical parameters such as viscosity and interface thickness. To uncover the nature of such points we consider a weakly nonlinear analysis, that we have illustrated in §3.5. This analysis allows to find an evolution equation for the amplitude of the secondary instabilities growing nearby the bifurcation point. As we observed in §3.5, the two bifurcation points are subcritical and here we use Direct Numerical Simulations (DNS) to explicitly unveil it for the possible unstable modes in this flow configuration. We run our DNS as initial-value problems where the initial condition is given by the equilibrium solution $\bar{\mathscr{Z}}(\eta) = G_\eta(\eta)$ perturbed by (3.30) and (3.31) depending on the specific phase velocity we want to excite. Then we run the simulations in the neighborhood of the bifurcation points and use a^* - the first maximum in the temporal evolution of $a(t)$ - to track the solution's bifurcations. Above the bifurcation point, where the equilibrium state is linearly unstable, we expect the perturbations to grow exponentially as predicted by the linear analysis. We know from the weakly nonlinear theory and the choice of small viscosity that the bifurcation must be subcritical. Indeed below the bifurcation point we observe two possible scenarios. Strong enough perturbations allow the solution to nonlinearly saturate to an amplitude a^*, independent on A_0, which is the natural continuation in the bifurcation diagram of the linearly unstable states. Below a specific threshold in A_0, the solution shows no coherent structures and suffer a number of slowly decaying oscillations. Therefore we pick this threshold as mark of the unstable perturbations in the linearly stable region, and for solutions developing a persistent pattern we pick the first saturation maximum. By collecting these values for a range of J and different initial conditions (I_0 and I_2) we build the bifurcation diagram in figure 3.13a. The weakly nonlinear theory, which relies on the assumption of inviscid fluid and sharp interfaces, predicts the formation of two subcritical bifurcations departing from $\bar{J}(0, 0)$ and $\bar{J}(\pm 2, 0)$. In our numerical simulations we can clearly see the subcritical nature of the bifurcations

points which is being preserved by the introduction of the external layers even though we are considering thick interfaces in a viscous flow, whereas their branching is different. In Balmforth et al. (2012) they show the bifurcation diagram for the TCI when $\nu = 10^{-6}$ and $d = 0.2$ and we observe here that the introduction of two extra interfaces do not affect the overall structure of the branching which is similar for the three unstable modes. This is not surprising since only nearest-neighbor interactions are accounted by the model, thus no far field interactions can play a role here to change the bifurcations structure.

We divide the bifurcation diagram in three regions: region I is where $J < \bar{J}(0, 0.2)$; for region II $\bar{J}(0, 0.2) < J < \bar{J}(\pm 2, 0.2)$; in region III $J > \bar{J}(\pm 2, 0.2)$. We show the solutions in these regions, relative to the $c_r = 0$ or ± 2 initial value problems, in panel a,b), c,d) and e,f) respectively. The linear analysis says that in region I both phase velocities are stable, in region III are both unstable and in region II only $c_r = 0$ is unstable. On the other hand weakly nonlinear analysis says that $\bar{J}(0, 0.2)$ and $\bar{J}(\pm 2, 0.2)$ are subcritical bifurcation points. In region III we observe the linear growth of modes with $c_r = 0$ and $c_r = \pm 2$ to nonlinearly saturate at a^*. At this point a Taylor-Caulfield billow grows inside the layer embedded by the two resonating interfaces $\eta = c$ and moves with a phase speed equal to the background mean shear velocity. When we move to regions where the excited modes are stable the state reached in a^* has the same shape we described when J is bigger, but the process leading the fluid to this state is affected by the magnitude (A_0) of the initial perturbation. When A_0 is small enough the flow go has decaying oscillation - lower branches in 3.13a - and when A_0 is strong enough the solution converges to the upper branch of the same panel.

Secondary instabilities can be triggered in the flow by fully developed billows. Regardless the mode being excited, eventually the remaining billows will grow. In figure 3.13e,f we can clearly see this process when the modal perturbations are excited in region III. In panel e) we show the case of $c_r = 0$. The central billow forms during the linear growth and when nonlinearities stabilize its growth we see small oscillations in his shape. When these are strong enough the two adjacent billows form simultaneously. On the other hand when $c_r = 2$ is excited, after its formation, the next mode being excited by its oscillations, is in $\eta = -2$ and then $\eta = 0$, see panel f). From the time series in panel e) and f) we also see that the time in which secondary instabilities set in is ten time bigger in the symmetric case ($c_r = 0$), while when $c_r = 2$ the asymmetry somehow can trigger these instabilities earlier.

In region II we observe that the phenomenologies are the same but require longer times, and the asymmetry of the state shown in d) speed up the growth of the other billows. In region I we see something different: while the asymmetric initial condition $I_{\pm 2}$ will lead to the full billows configuration, the symmetric I_0 is not strong enough to trigger growth in near instabilities waves.

Linear stability analysis tells us that also higher wavenumbers may become unstable if high enough Richardson numbers are provided. Here we want to understand which is the nonlinear evolution of small scale TCI. Again, we consider a $M = 4$ fluid of smooth interfaces of thickness $d = 0.2$. The stability analysis tells us that if we consider $J = 3.6$, wavenumbers $k = 1$, 2, 3 and 4 are unstable. Therefore we run simulations where the equilibrium state is perturbed by i_k, with $A_0 = 0.01$. In figure 3.14 we report numerical simulations for k =2, 3 and 4 respectively in panels a), b) and c) (the last goes together with the three snapshots). The linear growth of the initial state reflects the wavenumber kicked by i_k, as we can see in panel a), b) and c). In these panels we show the evolution of the first four wave numbers where (*black*) is $k = 1$, (*blue*) is $k = 2$, (*red*) is $k = 3$ and (*magenta*) is $k = 4$. From these simulations we see that high wavenumber modes are unstable to secondary instabilities that will promote longer wavelength structures. In panel a) we see mode $k = 2$ to exponentially grow, saturates for a finite amount of time until $k = 1$ kicks in and replaces $k = 2$. In panel b) we see mode $k = 3$ to exponetially grow, but quickly merge to $k = 1$ skipping $k = 2$. Finally in panel c), and in the snapshots below, we report numerical computation of $k = 4$. After this mode kicks in and saturates (first snapshot) we observe the four billows per layer to merge to two billows per layer (see second snapshot). This is also an unstable configuration and thereafter mode $k = 1$ grows and finally stabilizes the fluid.

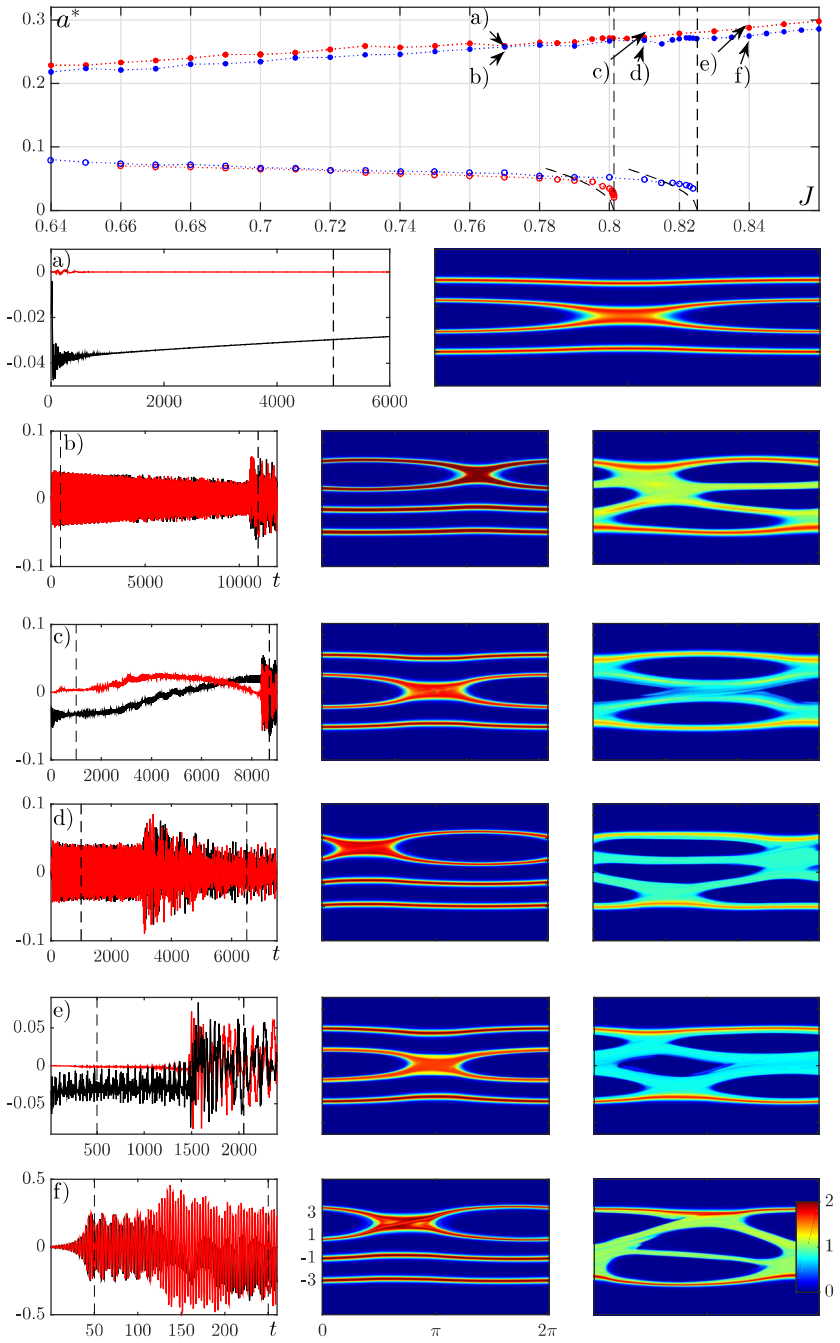

Figure 3.13: Bifurcation diagram of the saturation maxima a^* agains the Richardson number J. We consider $M = 4$ interfaces of thickness $d = 0.2$ with a viscosity $\nu = 10^{-6}$ and $Pr = 1$. We focus on pure modes (I_0 or I_2) with $k = 1$ and phase velocity $c_r = 0$ or ± 2. The two dashed vertical lines represent $\bar{J}(0, 0.2)$ and $\bar{J}(\pm 2, 0.2)$ and the two thick dashed curves are the amplitude equation's solutions predicted by weakly nonlinear theory. In panels a)-f) we report solutions for initial value problems in region I-III. The left panels show the real ($-$) and imaginary ($-$) part of mode $\Phi_1(t)$ and the vertical dashed line is when the snapshot on the right panel have been taken.

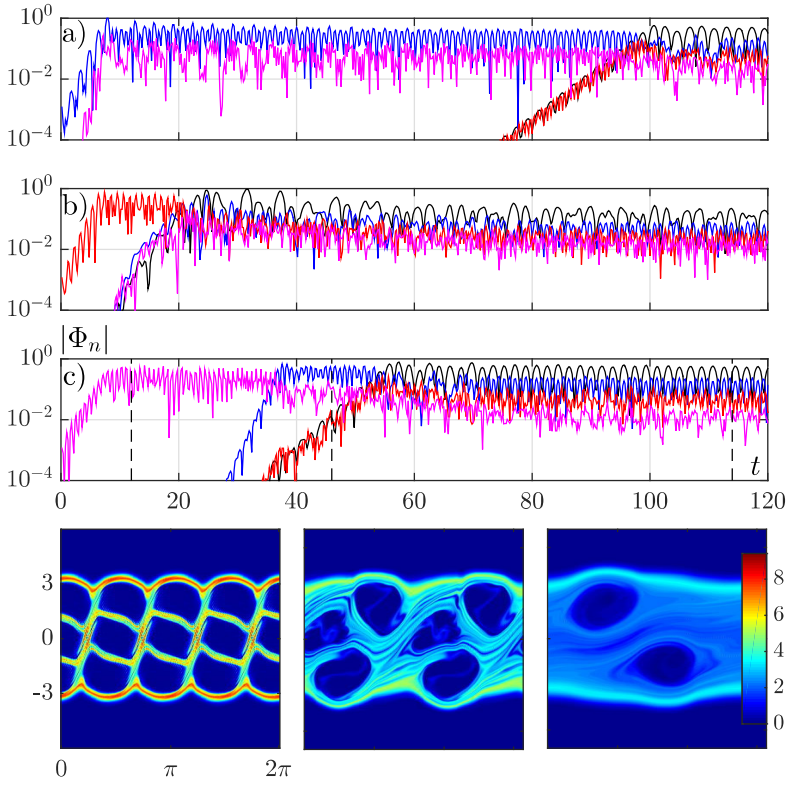

Figure 3.14: We compare billows merging for initial perturbations (3.29) of increasing wavenumber. We consider $M = 4$ interfaces of thickness $d = 0.2$ in a fluid of viscosity $\nu = 3 \cdot 10^{-4}$ and $J = 3.6$ which allow wavenumbers $k = 1$, 2, 3 and 4 to be unstable. In panel a), b) and c) we show the time evolution of $|\Phi_n|$ where the black, blue, red and magenta lines are for $n = 1$, 2, 3 and 4 respectively. In panel a) we perturb the equilibrium state using i_2, in panel b) is i_3 and in panel c) i_4. The three snapshots of the solution show the merging of billows when mode $k = 4$ is initially induced in the fluid. In panel c) we show by vertical dashed lines the time at which these snapshots are taken.

Chapter 4

Conclusions

In this thesis the Candidate studied instabilities in stratified shear flows. The field is broad and contributions have been multiple. In this work the density stratification is assumed to be stabilizing, therefore lighter fluids lay above heavier ones. In few cases such stratifications proved to be capable of destabilizing otherwise stable fluids, contradicting the common idea of buoyancy forces having a restoring effects. Here we study two different systems and how the density stratification affects the stability of their equilibrium solutions.

In the first case we consider the stratified counterpart of the Kolmogorov flow, a two-dimensional parallel flow of sinusoidal form. This flow has been widely studied and shows a rich number of states departing from the laminar solution as viscosity is lowered. Two branches of solutions lead the flow to chaotic states, and here we compare this (almost) known route to chaos to progressively stratified Kolmogorov flows. One branch is characterized by horizontally drifting solutions, the other by horizontally steady (in mean) solutions. The first shows a Pomeau-Manneville route to chaos - transition to chaos is due to intermittency of bursting solutions. The second was left obscure in previous works: a periodic orbit solution loses its stability toward a somehow chaotic state. In this thesis a finer investigation have been done, and a new solution, precursor to the transition to chaos, have been observed. The periodic orbit undergoes a supercritical period-tripling bifurcation. Thereafter a Lyapunov exponents analysis proves that the subsequent bifurcation of this newly observed state is toward chaos.

Given the set of all bifurcations in the unstratified case, increasing stratifications (and therefore Richardson numbers) are accounted. Whilst the set of bifurcations is almost

unchanged for Richardson number less than 10^{-3}, we observe some variations in the bifurcations from $Ri = 10^{-3}$ and higher. As we expect there is a general tendency for state transitions to onset at higher Reynolds numbers, whereas a somehow unexpected enhancement of the number of available states is also observed. When $Ri = 10^{-3}$ the period-tripling bifurcation becomes subcritical and suffer three period-doubling bifurcations before it gets to chaotic solutions. When the Richardson number is increased to $5 \cdot 10^{-3}$ we observe significant differences. A window of chaotic solutions, proved again by positivity of a Lyapunov exponent, opens up at middle Reynolds numbers on the periodic orbit solution branch. Then a completely different route to chaos departs from it: the periodic orbit has a supercritical period-doubling bifurcation, which later on becomes chaotic. At even higher Reynolds number a roughly period-tripled state appear, which again undergoes a threefold period-doubling bifurcation before becoming chaotic. Another striking change is on the drifting solution's branch. It shows a precursor periodic bursting solution where the state regularly jumps among four available drifting solutions. It is therefore clear that a stabilizing density gradient increases the critical Reynolds numbers needed to trigger state's transitions, while "unlocking" a number of new states inaccessible to the unstratified Kolmogorov flow.

The second part of the thesis is devoted to the analysis of instabilities due to waves generated by density defects. The formation of multilayered fluids is common in natural environments as oceans and lakes where layering can be a result of turbulent mixing or double-diffusive convection. The density gradient between layers is usually high and sharp, giving the possibility to interfacial waves to grow and propagate. In such systems there is also a ubiquitous shear velocity, that is assumed to be linear here, and has the effect of Doppler-shifting the interfacial waves. Among fundamental instability processes as Kelvin-Helmholtz instability or Holmboe wave instability, Taylor (1931) theorized an instability given by two interfacial waves which resonates thanks to the background shear. As Taylor explained in his paper and Caulfield (1994); Caulfield et al. (1995) shows in his works, such instability proved to be difficult to be observed in natural systems and laboratory experiments as well, despite its theoretical explanation. One of the reason lie in the nonlinear development of the instability. It produces elliptical billows between the resonating interfaces which are embedded by vorticity filaments. Being the fluid stratified, such vorticity defects support the formation of secondary Kelvin-Helmholtz and Holmboe wave instabilities which rapidly destroy the finite amplitude state produced by the Taylor-Caulfield

Instability (TCI). In this work the main purpose is to investigate the susceptibility of a number of constant density layers separated by equally spaced sharp interfaces to TCI and their subsequent nonlinear evolution.

Assuming the fluid to be inviscid and interfaces to be sharp, the linear stability analysis tell us that TCI due to resonance of nearest neighbor interfaces are the most unstable and easy to access. Then the second neighbor interfaces resonances are the next most unstable instabilities and so on. Far neighbor instabilities, while having smaller growth rates than nearest neighbor interfaces, exist also in narrow instability domains, making them particularly difficult to be observed. Moreover amongst every nearest neighbor TCI, the strongest are located in the core of the layered structure. To test the robustness of these results two different studies have been done. The first considers finite thickness interfaces of piecewise-linear profile, the second consider a statistical number of realizations of unevenly thick layers. The simple shape of the interface we consider in the first test, allows to write an explicit dispersion relation when the system has two interfaces. We observe that small scales waves need higher stratifications to become unstable compared to the sharp interfaces counterpart. Moreover an infinite number of equally distant instability domains appear of which solutions have an increasing number of oscillation within the interface. For the second test linear stability analysis is conducted for a hundred of realizations showing that unevenly displaced interfaces play a small role in the stability of the layers introducing negligible variations in the stability of the fluid.

Inspired by the linear stability results, where the strongest instabilities come from nearest neighbor interactions, we observe their strongest growth happens to be in the limit of small wavenumbers and Richardson numbers. Therefore, following the defect theory approximation introduced by Balmforth et al. (2012), where the layers are flattened inside a defect of horizontal dimension much larger than the vertical one, we obtain a reduced system of equations. The linear stability analysis of the equilibrium state under these approximations reduces to solve a dispersion relation of integral form which can be easily solved numerically. This allows to consider more exotic interface profiles. Assuming hyperbolic tangent interfaces allow to study the dependence of the critical Richardson number for the onset of instability and their subsequent growth rate. We observe that the onset of instabilities is a non-monotonic function of the thickness, with the bifurcation point being lowered by small thickening and then increasing for thicker interfaces. At the same

time the thickness progressively suppresses the growth of unstable waves. A remarkable investigation is also made possible in the defect limit, by introducing viscosity in the linear stability analysis. We observe viscosity to have a destabilizing effect on the fluid, not only it allows resonance-induced instabilities as the inviscid counterpart, but also it makes stable or unstable otherwise marginally stable waves. This observation cannot be explained by the waves interaction approach valid for inviscid fluid and therefore a new instability mechanism must be proposed.

Under the same approximations we consider weakly nonlinear perturbations of the equilibrium solution. In the limit case of inviscid fluid we obtain an amplitude equation describing a secondary solution bifurcating subcritically from the equilibrium state. Therefore we solve numerically the nonlinear equations in the small viscosity limit and observe a subcritical bifurcation as well. Moreover we confirm the linear stability predictions for which core layers instabilities destabilize before outer layers instabilities and observe that no matter which TCI is triggered first, eventually a TCI billow per layer will form. We also observe that small scales TCI, available at high Richardson numbers, suffer secondary instabilities in the form of vortex-pairing coalescence.

Chapter 5

Bibliography

A. Alexakis. On Holmboe's instability for smooth shear and density profiles. *Physics of Fluids (1994-present)*, 17(8):084103, 2005.

D. Armbruster, B. Nicolaenko, N. Smaoui, and P. Chossat. Symmetries and dynamics for 2-d Navier-Stokes flow. *Physica D: Nonlinear Phenomena*, 95(1):81–93, 1996.

V.I. Arnol'd and L.D. Meshalkin. Seminar led by A.N. Kolmogorov on selected problems of analysis (1958-1959). *Usp. Mat. Nauk.*, 15:20–24, 1960.

C. Arratia, C.P. Caulfield, and J.M. Chomaz. Transient perturbation growth in time-dependent mixing layers. *Journal of Fluid Mechanics*, 717:90–133, 2013.

P.G. Baines and H. Mitsudera. On the mechanism of shear flow instabilities. *J. Fluid Mech.*, 276:327–342, 1994.

N. J. Balmforth, A. Roy, and C. P. Caulfield. Dynamics of vorticity defects in stratified shear flow. *Journal of Fluid Mechanics*, 694:292–331, 2012.

N.J. Balmforth. Stability of vorticity defects in viscous shear. *Journal of Fluid Mechanics*, 357:199–224, 1998.

N.J. Balmforth and Y. Young. Stratified Kolmogorov flow. *Journal of Fluid Mechanics*, 450:131–167, 2002.

N.J. Balmforth, D. del Castillo-Negrete, and W.R. Young. Dynamics of vorticity defects in shear. *Journal of Fluid Mechanics*, 333:197–230, 1997.

A. M. Batchaev. Laboratory simulation of the Kolmogorov flow on a spherical surface. *Izvestiya, Atmospheric and Oceanic Physics*, 48(6):657–662, 2012.

A.M. Batchaev and M.V. Kurgansky. Periodic shear flow instability in a weakly stratified fluid. *Izv.Atmos.Oceanic Phys.*, 22(1):1–5, 1986.

A.M. Batchaev, V.A. Dovzhenko, and M.V. Kurgansky. Simulation of shear flow in a stratified fluid. *Izv.Atmos.Oceanic Phys.*, 20(6):439–442, 1984.

O.O. Bendiksen. Nonlinear mode interactions and period-tripling flutter in transonic flow. *Journal of fluids and structures*, 19(5):591–606, 2004.

N.F. Bondarenko, M.Z. Gak, and F.V. Dolzhanskiy. Laboratory and theoretical models of plane periodic flows. *Izv.Atmos.Oceanic Phys.*, 15(3):711–716, 1979.

J. M. Burgess, C. Bizon, W. D. McCormick, J. B. Swift, and H. L. Swinney. Instability of the Kolmogorov flow in a soap film. *Physical Review E - Statistical Physics, Plasmas, Fluids, and Related Interdisciplinary Topics*, 60(1):715–721, 1999.

P. Caillol. Nonlinear internal waves in the upper atmosphere. *Geophysical and Astrophysical Fluid Dynamics*, 99(4):271–308, 2005.

R.A. Cairns. The role of negative energy waves in some instabilities of parallel flows. *Journal of Fluid Mechanics*, 92(01):1–14, 1979.

J.R. Carpenter, N.J. Balmforth, and G.A. Lawrence. Identifying unstable modes in stratified shear layers. *Physics of Fluids*, 22(5):054104, 2010a.

J.R. Carpenter, E.W. Tedford, M. Rahmani, and G.A. Lawrence. Holmboe wave fields in simulation and experiment. *Journal of Fluid Mechanics*, 648:205, 2010b.

J.R. Carpenter, E.W. Tedford, E. Heifetz, and G.A. Lawrence. Instability in stratified shear flow: Review of a physical interpretation based on interacting waves. *Applied Mechanics Reviews*, 64(6):060801, 2011.

C.P. Caulfield. Multiple linear instability of layered stratified shear flow. *Journal of Fluid Mechanics*, 258:255–285, 1994.

C.P. Caulfield and W.R. Peltier. The anatomy of the mixing transition in homogeneous and stratified free shear layers. *Journal of Fluid Mechanics*, 413:1–47, 2000.

C.P. Caulfield, W.R. Peltier, S. Yoshida, and M. Ohtani. An experimental investigation of the instability of a shear flow with multilayered density stratification. *Physics of Fluids*, 7(12):3028–3041, 1995.

G.J. Chandler and R.R. Kerswell. Invariant recurrent solutions embedded in a turbulent two-dimensional Kolmogorov flow. *Journal of Fluid Mechanics*, 722:554–595, 2013.

C.Z. Cheng and G. Knorr. The integration of the vlasov equation in configuration space. *Journal of Computational Physics*, 22(3):330–351, 1976.

P.A. Davis and W.R. Peltier. Resonant parallel shear instability in the stably stratified planetary boundary layer. *Journal of the Atmospheric Sciences*, 33(7):1287–1300, 1976.

V. Franceschini, C. Tebaldi, and F. Zironi. Fixed point limit behavior of N-mode truncated Navier-Stokes equations as N increases. *Journal of Statistical Physics*, 35(3-4):387–397, 1984.

G. Gambino, M.C. Lombardo, and M. Sammartino. Adaptive control of a seven mode truncation of the Kolmogorov flow with drag. *Chaos, Solitons and Fractals*, 41(1):47–59, 2009.

P. Garaud, B. Gallet, and T. Bischoff. The stability of stratified spatially periodic shear flows at low Péclet number. *Physics of Fluids*, 27(8):084104, 2015.

A.E. Gill. A mechanism for instability of plane Couette flow and of Poiseuille flow in a pipe. *Journal of Fluid Mechanics*, 21(03):503–511, 1965.

B.K. Goswami. Observation of some new phenomena involving period tripling and period doubling. *International Journal of Bifurcation and Chaos*, 05(01):303–312, 1995.

B.K. Goswami. Self-similarity in the bifurcation structure involving period tripling, and a suggested generalization to period n-tupling. *Physics Letters, Section A: General, Atomic and Solid State Physics*, 245(1-2):97–109, 1998.

A. Guha and G.A. Lawrence. A wave interaction approach to studying non-modal homogeneous and stratified shear instabilities. *Journal of Fluid Mechanics*, 755:336–364, 2014.

C.C. Hamakiotes and S.A. Berger. Periodic flows through curved tubes. the effect of the frequency parameter. *Journal of Fluid Mechanics*, 210:353–370, 1990.

H. Helmholtz. On discontinuous movements of fluids. *Phil. Mag.*, 36:337–346, 1868.

J. Holmboe. On the behavior of symmetric waves in stratified shear layers. *Geophys. Publ*, 24:67–113, 1962.

M. Inubushi, M. U. Kobayashi, S. Takehiro, and M. Yamada. Covariant Lyapunov analysis of chaotic Kolmogorov flows and time-correlation function. In *Procedia IUTAM*, volume 5, pages 244–248, 2012.

Lord Kelvin. Hydrokinetic solutions and observations. *Phil. Mag.*, 42:362–377, 1871.

M.V. Kurganskii. Instability of internal gravity waves propagating at small angles to the vertical. *Izvestia Akademii nauk SSSR. Fizika atmosfery i okeana*, 16(10):1024–1033, 1980.

H. Lamela, G. Carpintero, and F.J. Mancebo. Period tripling and chaos in the dynamic behavior of directly modulated diode lasers. *IEEE Journal of Quantum Electronics*, 34 (10):1797–1801, 1998.

V. Lee and C.P. Caulfield. Nonlinear evolution of a layered stratified shear flow. *Dynamics of atmospheres and oceans*, 34(2):103–124, 2001.

A. Libchaber and J. Maurer. A Rayleigh Bénard experiment: Helium in a small box. In T. Riste, editor, *Nonlinear Phenomena at Phase Transitions and Instabilities*, volume 77 of *NATO Advanced Study Institutes Series*, pages 259–286. Springer US, 1982.

E. Lorenz. Barotropic instability of Rossby wave motion. *J. Atmos. Sci.*, 29:258–264, 1972.

D. Lucas and R. Kerswell. Spatiotemporal dynamics in two-dimensional Kolmogorov flow over large domains. *Journal of Fluid Mechanics*, 750:518–554, 2014.

D. Lucas and R. Kerswell. Recurrent flow analysis in spatiotemporally chaotic 2-dimensional Kolmogorov flow. *Physics of Fluids*, 27(4), 2015.

A.J. Manfroi and W. Young. An investigation of chaotic Kolmogorov flows. *J. Atmos. Sci.*, 56:784–800, 1999.

C. Marchioro. An example of absence of turbulence for any Reynolds number. *Communications in Mathematical Physics*, 105(1):99–106, 1986.

A. Mashayek and W.R. Peltier. The 'zoo' of secondary instabilities precursory to stratified shear flow transition. Part 1 Shear aligned convection, pairing, and braid instabilities. *Journal of Fluid Mechanics*, 708:5–44, 2012a.

A. Mashayek and W.R. Peltier. The 'zoo' of secondary instabilities precursory to stratified shear flow transition. Part 2 The influence of stratification. *Journal of Fluid Mechanics*, 708:45–70, 2012b.

L.D. Meshalkin and Ia G. Sinai. Investigation of the stability of a stationary solution of a system of equations for the plane movement of an incompressible viscous liquid. *Journal of Applied Mathematics and Mechanics*, 25(6):1700–1705, 1961.

A.A. Nepomniashchii. On stability of secondary flows of a viscous fluid in unbounded space. PMM vol. 40, no. 5, 1976, pp. 886-891. *Journal of Applied Mathematics and Mechanics*, 40(5):836–841, 1976.

B. Nicolaenko and Z.-S. She. Coherent structures, homoclinic cycles and vorticity explosions in Navier-Stokes flows. In *Topological fluid mechanics (Cambridge, 1989)*, pages 265–277. Cambridge Univ. Press, Cambridge, 1990.

H. Okamoto and M. Shoji. Bifurcation diagrams in Kolmogorov's problem of viscous incompressible fluid on 2-d flat tori. *Japan Journal of Industrial and Applied Mathematics*, 10(2):191–218, 1993.

W. M'F. Orr. The stability or instability of the steady motions of a perfect liquid and of a viscous liquid. Part I: A perfect liquid. *Proc. R. Irish Acad. Sect.*, A(27):9–68, 1907a.

W. M'F. Orr. The stability or instability of the steady motions of a perfect liquid and of a viscous liquid. Part II: A viscous liquid. *Proc. R. Irish Acad. Sect.*, A(27):69–138, 1907b.

N. Platt, L. Sirovich, and N. Fitzmaurice. An investigation of chaotic Kolmogorov flows. *Physics of Fluids A*, 3(4):681–696, 1991.

G. Ponetti, M. Sammartino, and V. Sciacca. Formation of coherent structures in Kolmogorov flow with stratification and drag. *Acta Applicandae Mathematicae*, 132(1):483–492, 2014.

J. W. S. Rayleigh. On the stability, or instability, of certain fluid motions. *Proc. London Math. Soc.*, 12:57–72, 1880.

O. Reynolds. An experimental investigation of the circumstances which determine whether the motion of water shall be direct or sinuous, and of the law of resistance in parallel channels. *Phil. Trans. R. Soc. Lond.*, 174:935–982, 1883.

H. Schlichting. Zur entstehung der turbulenz bei der plattenströmung [on the onset of turbulence in boundary layer flow]. *Z. Angew. Math. Mech.*, 13:171–174, 1933.

G. B. Schubauer and H. K. Skramstad. Laminar boundary-layer oscillations and stability of laminar flow. *J. Aeronaut. Sci.*, 14:69–78, 1947.

J.F. Scinocca and R. Ford. The nonlinear forcing of large-scale internal gravity waves by stratified shear instability. *Journal of the atmospheric sciences*, 57(5):653–672, 2000.

Z.S. She. Metastability and vortex pairing in the Kolmogorov flow. *Physics Letters A*, 124 (3):161–164, 1987.

G.I. Sivashinsky. Weak turbulence in periodic flows. *Physica D: Nonlinear Phenomena*, 17 (2):243–255, 1985.

W.D. Smyth and J. N. Moum. Ocean mixing by Kelvin-Helmholtz instability. *Oceanography*, 25:140–149, 2012.

W.D. Smyth, G.P. Klaassen, and W.R. Peltier. Finite amplitude Holmboe waves. *Geophysical & Astrophysical Fluid Dynamics*, 43(2):181–222, 1988.

A. Sommerfeld. Ein beitrag zur hydrodynamischen erklaerung der turbulenten fluessigkeitsbewegungen. In *Proceedings of the 4th International Congress of Mathematicians III, Rome, Italy*, volume 4, pages 116–124, 1908.

B. Suri, J. Tithof, R. Mitchell Jr., R.O. Grigoriev, and M.F. Schatz. Velocity profile in a two-layer Kolmogorov-like flow. *Physics of Fluids*, 26(5), 2014.

B.R. Sutherland. *Internal gravity waves.* Cambridge University Press, 2010.

G.I. Taylor. Stability of a viscous liquid contained between two rotating cylinders. *Philosophical Transactions of the Royal Society of London A: Mathematical, Physical and Engineering Sciences*, 223(605-615):289–343, 1923. ISSN 0264-3952. doi: 10.1098/rsta.1923.0008.

G.I. Taylor. Effect of variation in density on the stability of superposed streams of fluid. *Proc.R.Soc.London*, 132:499–523, 1931.

E.W. Tedford, R. Pieters, and G.A. Lawrence. Symmetric Holmboe instabilities in a laboratory exchange flow. *J. Fluid Mech.*, 636:137–153, 2009.

A. Thess. Instabilities in two-dimensional spatially periodic flows. Part I: Kolmogorov flow. *Physics of Fluids A*, 4(7):1385–1395, 1992.

S.A. Thorpe. A method of producing a shear flow in a stratified fluid. *J. Fluid Mech.*, 32 (04):693–704, 1968.

S.A. Thorpe. Experiments on the instability of stratified shear flows: miscible fluids. *Journal of Fluid Mechanics*, 46(02):299–319, 1971.

W. Tollmien. Über die entstehung der turbulenz [On the onset of turbulence]. *Nachr. Ges. Wiss, Göttingen, Math. Phys. Klasse*, 1:21–44, 1929.

A. Wolf, J. B. Swift, H. L. Swinney, and J. A. Vastano. Determining Lyapunov exponents from a time series. *Physica D: Nonlinear Phenomena*, 16(3):285–317, 1985.

Appendix A

TCI related problems

A.1 In-depth linear stability analysis

A.1.1 Randomly displaced interfaces

In geophysical systems layers have a characteristic vertical dimension L and each layer stochastically displaces from it by small amounts. Here we want to test the reliability of linear analysis results for the ideal geometry of evenly spaced steps explained in §3.4 when more realistic flow geometries are accounted. The aforementioned section focuses on M sharp interfaces (3.8) in the inviscid and non-diffusive limit. To introduce stochasticity in the displacement of interfaces in $y = \pm 1, \pm 3, \ldots, \pm(M-1)$ we consider $\{\sigma_j \,|\, j = -M+3, \ldots, M-3\}$ to be normal distributed random numbers. Moreover we choose to keep the density difference between the layers constant and to keep the outer interfaces in $y = \pm(M-1)$.

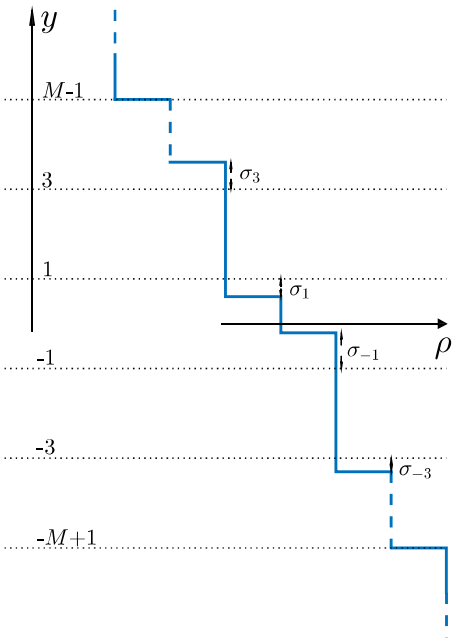

Figure A.1: Density stratification of a fluid with a number M of interfaces displaced by $\{\sigma_j | \, j = -M+3, \ldots, M-3\}$ from the ideal configuration shown in figure 3.1.

The comparison to the ideal case is made

with the analogous of figure 3.3 and 3.5 where we superpose a density function which counts the number of occurrences inside bins of fixed size - the horizontal and vertical domains are subdivided in 100×100 bins - and normalized by the number of realizations (100). According to figure 3.3 we count the marginally stability curves passing through the bins, whilst following figure 3.5 we collect c. The fluid geometry is shown in figure A.1 and we run 100 realizations $\{\sigma_j\}$ for the uneven configuration to have an idea on how the stability analysis results are affected by these displacements.

Here we consider four interfaces embedded in the fluid for which the coefficients matrix of the linear problem (3.46) becomes

$$\mathscr{G}_4^{\sigma} = \begin{Vmatrix} K(3-c)^2-1 & -\epsilon & -\epsilon^2 & -\epsilon^3 \\ -\epsilon & K(1+\sigma_1-c)^2-1 & -\epsilon & -\epsilon^2 \\ -\epsilon^2 & -\epsilon & K(1+\sigma_{-1}+c)^2-1 & -\epsilon \\ -\epsilon^3 & -\epsilon^2 & -\epsilon & K(3+c)^2-1 \end{Vmatrix}. \tag{A.1}$$

The two middle interfaces are shifted by σ_1 and σ_{-1} which are random numbers generated using a normal distribution of standard deviation 0.2. The dispersion relation $D(c; J, k) = \det(\mathscr{G}_4^{\sigma}) = 0$ has eight roots which are computed numerically in the same fashion explained in §3.4 and following that analysis we show marginal stability lines on the (J, k)-plane and a cut through at $k = 0.01$ computing c as function of J. This computations are summarized by mean of the density function, shaded colors in figure A.2, and compared to the evenly spaced configuration (red lines). In panel a) of figure A.2 we show collection of marginal stability lines and we observe that the strongest departures from the ideal case are related to the near neighbor interfaces which always involve displaced interfaces. On the contrary the furthest interfaces (B^+B^-) are the less affected since are kept in the same position as in the ideal case. A similar scenario is reported in panel b) of the same figure where we decided to show only positive phase velocities of unstable modes. The resonance between nearest-neighbor interfaces is (unsurprisingly) the most affected since is the only one involving displaced interfaces. Moreover we observe a shift in the bifurcation point and the possibility of faster and slower growing modes[1].

[1] in the conclusion write it is in line with the results of Churilov(2016)

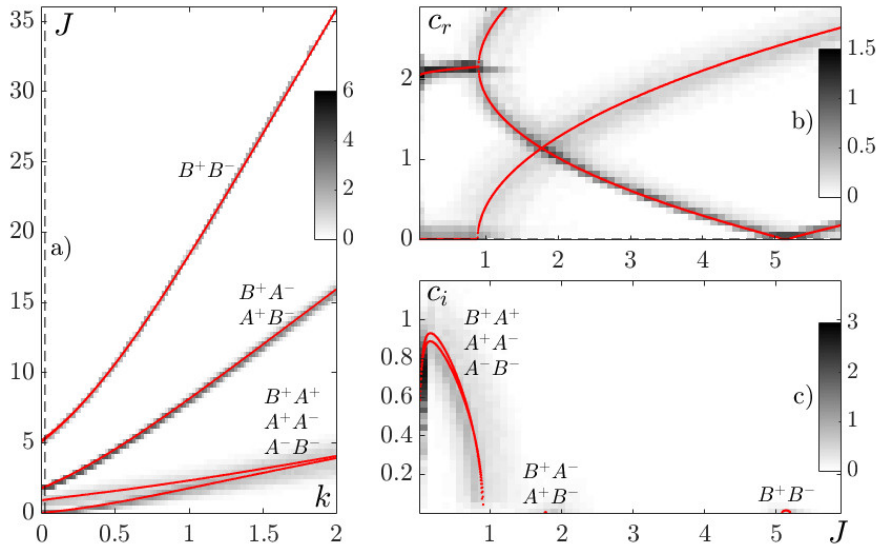

Figure A.2: Stability boundaries (a) and phase velocity $c = c_r + c_i$ (b and c) for internal gravity waves in a $M = 4$ interfaces fluid. The red curves come from the equally spaced layers. The 100 realizations of $\{\sigma_j\}$ are summarized by showing the shaded density function which counts the occurrence of a stability boundary inside a grid-cell. In panel a) the dashed line shows where we cut through ($k = 0.01$) in panels b) and c) We displace the position of the interfaces using a normal distribution and resume 100 realizations using a density plot (gray regions).

A.1.2 Piecewise-linear interfaces

In this section we consider a more realistic instance of the two interfaces TCI problem. The assumption of a sharp density variation is left behind and replaced with the piecewise-linear interface. We conduct the linear stability analysis of waves, again, in an inviscid and non-diffusive fluid finding an explicit dispersion relation from the Taylor-Goldstein equation (3.33). We consider a piecewise-linear density interface, which in term of the vertical buoyancy field gradient is

$$\Theta(y) = \frac{1}{4d}(1 - \mathrm{sgn}(|y|/d - 1)), \tag{A.2}$$

and d measures the thickness of the interface. The equilibrium profile is then $G_y(y) = J[\Theta(y-1) + \Theta(y+1)]$ and the solution of the Taylor-Goldstein equation (3.33) is

$$\psi = \begin{cases} A_+ e^{-k(y-1)} & y > 1 + d \\ \psi_+ & |y-1| < d \\ B_+ e^{ky} + B_- e^{-ky} & |y| < 1 - d \\ \psi_- & |y+1| < d \\ A_- e^{+k(y+1)} & y < -1 - d \end{cases} \tag{A.3}$$

where the outer and core part of the solution are solutions of the Helmholtz equation themselves, whilst ψ_+ and ψ_- are unknown solutions of

$$\frac{d^2\widehat{\psi}}{dy^2} = -\mathcal{K}^2\widehat{\psi}, \text{ where } -\mathcal{K}^2 = k^2 - \frac{J}{2d\,(y-c)^2}, \tag{A.4}$$

inside the two interfaces centered in $y = 1$ and $y = -1$. Continuity of the solution and its derivative at the inner edges of the two interfaces $y = \pm(1-d)$ gives the four conditions

$$\widehat{A}_+ = b_+ + \hat{\epsilon} b_-, \quad G_+\widehat{A}_+ = (b_+ - \hat{\epsilon} b_-), \tag{A.5}$$

$$\widehat{A}_- = \hat{\epsilon} b_+ + b_-, \quad G_-\widehat{A}_- = (\hat{\epsilon} b_+ - b_-), \tag{A.6}$$

where we defined the quantities

$$b_\pm = B_\pm e^k, \quad \hat{A}_\pm = \psi_\pm e^{kd}, \quad \hat{\epsilon} = e^{-2k(1-d)}, \quad G_\pm = \frac{1}{k}\left.\frac{\psi'_\pm}{\psi_\pm}\right|_{\pm(1-d)}. \tag{A.7}$$

After some algebra we get the dispersion relation

$$(G_+ - 1)(G_- + 1) - \hat{\epsilon}^2(G_+ + 1)(G_- - 1) = 0 \tag{A.8}$$

which is useless since $G_\pm$ is still an undetermined quantity. Therefore we look for solutions inside the two interfaces. As we already mentioned, the equation inside the interface is (A.4), which looks like an Helmholtz equation, but with a wavenumber depending on the vertical coordinate y. To ease the problem and to remove the dependence upon y, we replace it by $Y_\pm = \pm 1$ inside the interfaces, thus the new wavenumber becomes

$$\mathcal{K}_\pm^2 = \frac{J}{2d(Y_\pm - c)^2} - k^2. \tag{A.9}$$

Now an explicit solution can be found and asking for continuity of the solution and its derivative in the outer edges of the interfaces $y = \pm(1+d)$, we get

$$\psi_\pm = A_\pm e^{-kd}\left[\cos\theta_\pm \mp \frac{k}{\mathcal{K}_\pm}\sin\theta_\pm\right], \text{ where } \theta_\pm = \mathcal{K}_\pm\Big(y \mp (1+d)\Big). \tag{A.10}$$

Now evaluating these solutions in $y = \pm(1-d)$, as the definition of $G_\pm$ asks, we get

$$G_\pm = \frac{1}{k}\frac{\psi'_\pm}{\psi_\pm} = \pm\frac{\mathcal{K}_\pm}{k}\frac{T_\pm - k/\mathcal{K}_\pm}{1 + kT_\pm/\mathcal{K}_\pm}, \text{ where } T_\pm = \tan(2d\mathcal{K}_\pm). \tag{A.11}$$

We solve numerically the dispersion relation (A.8) which produces the results shown in figure A.3. The instability band with the lowest J follows the result for a discontinuous pair of interfaces for small k. However, the band then bends upward away and from the asymptote $J = 2k$. More instability bands are also available at specific Richardson numbers, which correspond to normal modes with an increasing number of spatial oscillations within each interface. These solutions are shown in the insets of figure A.3. The marginally stable bands occur when $G_\pm = O(1)$ and provided (A.11) this happens when $T_\pm = 0$ leading to the condition

$$J = \frac{n^2\pi^2}{2d} \tag{A.12}$$

marked in figure A.3 by red dots. As for the piecewise-constant stratified fluid, we observe weaker growth in the higher Richardson number bands - see right panel of figure A.3.

A.2 Weakly non-linear theory

We set up weakly non-linear approximations of the defect equations (3.25) and (3.26) to describe the primary bifurcation of the laminar solution $\bar{U} = y$ with background density profile $H(\eta) = G_\eta(\eta)$. We look for solutions that evolve over long timescales, thus we rescale the time as $T = \varepsilon t$. The linear stability of the defect problem suggests that unstable modes

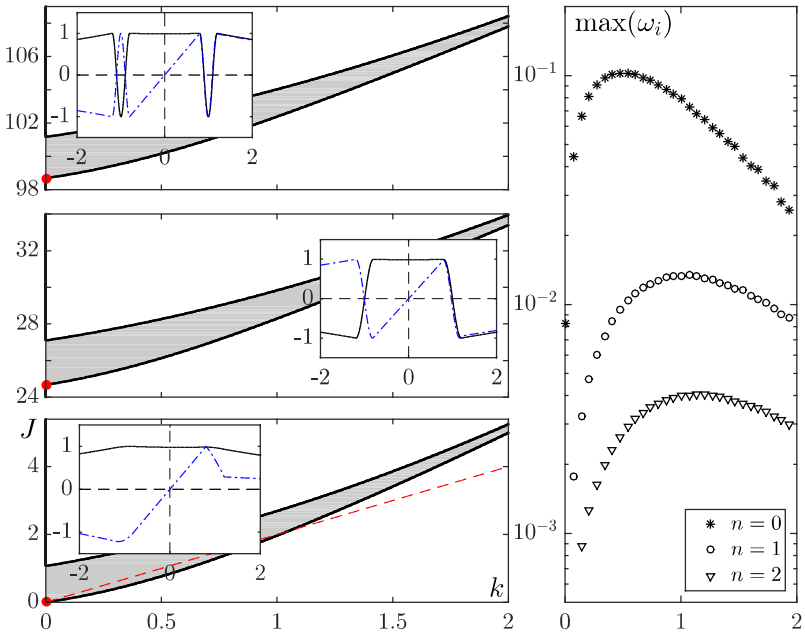

Figure A.3: Dispersion relation for internal gravity waves growing in a three layers fluid. The two interfaces are piecewise-linear with thickness $d = 0.2$. In left panels we show the unstable bands and the solution of Taylor-Goldstein equation on the marginal stability boundaries. The shaded region is where the waves are unstable and the black lines correspond to the marginal stability boundaries. The red dots are predictions (A.12) of where the bands arise and the red dashed line is the $k \gg 1$ limit, $J = 2k$, for sharp interfaces. In the insets we show the solutions on the upper ($.-$) and lower ($-$) marginal stability curve at $k = 0.2$. In the right panel we show the maximum growth rate inside the first five unstable bands.

with different phase velocities do not interact, allowing us tu introduce a reference system moving at the phase velocity of the unstable wave $\tilde{x} = x - ct$. We define $\mathscr{Z}(x, \eta, t) = z(\tilde{x}, \eta, T)$, and ask for $\langle z(\tilde{x}, \eta, T) \rangle = 0$. Injecting these rescales into (3.25) and (3.26) and using the chain rule to unveil the dependence on the newly defined variables we get

$$(\eta - c) z_{\tilde{x}} + \Phi_{\tilde{x}} H_\eta = -\varepsilon z_T - \Phi_{\tilde{x}} z_\eta, \tag{A.13}$$

$$\mathscr{L}\Phi = \int_{-\infty}^{+\infty} z(\tilde{x}, \eta, T) d\eta, \tag{A.14}$$

where $H(\eta) = G_\eta(\eta)$ is defined in (3.11). In the expansion procedure we also use the horizontal average of (A.13) which is

$$\varepsilon \overline{z}_T = \overline{(\Phi z_{\tilde{x}})}_\eta, \text{ where } \overline{(\dots)} = \frac{1}{2\pi} \int_0^{2\pi} (\dots) d\tilde{x}. \tag{A.15}$$

The asymptotic expansion is made in term of ε to approximate the vertical gradient of the background buoyancy $H(\eta)$, the defect scalar field $z(\tilde{x},\eta,T)$, the leading order streamfunction inside the defect $\Phi(\tilde{x},T)$ and the bulk Richardson number J, such that

$$H = H_0 + \varepsilon^2 H_2 + \dots, \quad z = \varepsilon z_1 + \varepsilon^2 z_2 + \dots, \tag{A.16}$$

$$\Phi = \varepsilon\Phi_1 + \varepsilon^2\Phi_2 + \dots \quad \text{and} \quad J = J_0 + \varepsilon^2 J_2 + \dots \tag{A.17}$$

where the coefficients of the expansions are $O(1)$. Substituting these expansions in (A.13), (A.13) and (A.15) and collecting terms of the same order in ε give us a number of equations which allow to describe the primary bifurcation.

At $O(\epsilon)$ we find that

$$z_1 = -\frac{H_{0\eta}\Phi_1}{(\eta - c)}, \qquad \Phi_1 = A(T)e^{i\tilde{x}} + c.c.. \tag{A.18}$$

after integrating the first equation in $\tilde{x}$. The leading order streamfunction Φ_1 is given by a normal mode of wavenumber $k = 1$ and propagating at c. The temporal evolution of the amplitude $A(T)$ will be determined by equations coming from higher orders in ε. We recall that in the defect approximation, these phase velocities are determined by resonances between nearest neighbor interfaces. Thus system of reference will move at velocities $c = 0, \pm1, \pm2, \dots, \pm(M-2)$. Terms of $O(\varepsilon)$ in the integral equation (A.14) give

$$2 = \int_{-\infty}^{+\infty} \frac{H_{0\eta}}{(\eta - c)} d\eta \equiv I_1 \tag{A.19}$$

where we substituted (A.18) and called the integral I_1. At this order the horizontally averaged equation (A.15) is identically zero.

At next order, $O(\varepsilon^2)$, the contribution from the defect equation is

$$z_{2\tilde{x}} = -(z_{1T} + H_{0\eta}\Phi_{2\tilde{x}} + z_{1\eta}\Phi_{1\tilde{x}})/(\eta - c), \tag{A.20}$$

and after we integrate horizontally this equation we find

$$z_2 = \overline{z_2} - \frac{H_{0\eta}}{\eta - c}\Phi_2 - \frac{H_{0\eta}}{(\eta - c)^2}\Phi_{1\tilde{x}T} + \frac{\Phi_1^2 - \overline{\Phi_1^2}}{2(\eta - c)}\left(\frac{H_{0\eta}}{\eta - c}\right)_\eta, \tag{A.21}$$

where we used the relation $-\Phi_{1x} = \int \Phi_1 d\tilde{x}$ and integrated by part the last term. In this equation $\overline{z_2}$ and Φ_2 are unknown and are found thanks to the $O(\varepsilon)$ terms in (A.14) and (A.15). From the integral equation (A.14) we find

$$\Phi_2 = -\frac{I_3}{4}\left(A^2 e^{2i\tilde{x}} + c.c\right), \text{ where } I_3 = \int_{-\infty}^{+\infty} \frac{H_{0\eta}}{(\eta - c)^3} d\eta, \tag{A.22}$$

in which we used $\langle z(\tilde{x},\eta,T)\rangle = 0$. From the second order terms in the horizontal average (A.15) we get

$$\overline{z_2}_T = \left(\overline{\Phi_1 z_{2\tilde{x}} + \Phi_2 z_{1\tilde{x}}}\right)_\eta = \left(\frac{H_{0\eta}}{(\eta-c)^2}\right)_\eta \left(|A|^2\right)_T \tag{A.23}$$

which after substituting z_1, z_2, Φ_1 and Φ_2 and integrating in time gives

$$\overline{z_2} = \left(\frac{H_{0\eta}}{(\eta-c)^2}\right)_\eta \left(|A|^2 - |A_0|^2\right) \tag{A.24}$$

where we assumed $A(0) = A_0$ and $\overline{z_2}(\eta,0) = 0$.

We move to next order, $O(\varepsilon^3)$, and get

$$z_{3x} = -\left(H_{0\eta}\Phi_{3x} + H_{2\eta}\Phi_{1\tilde{x}} + z_{2T} + z_{1\eta}\Phi_{2\tilde{x}} + z_{2\eta}\Phi_{1\tilde{x}}\right)/(\eta - c), \tag{A.25}$$

$$\overline{z_3}_T = \left(\overline{\Phi_1 z_{3\tilde{x}} + \Phi_2 z_{2\tilde{x}} + \Phi_3 z_{1\tilde{x}}}\right)_\eta, \tag{A.26}$$

$$\mathscr{L}\Phi_3 = \int_{-\infty}^{+\infty} z_3\, d\eta. \tag{A.27}$$

By integrating (A.25) in $\tilde{x}$ we obtain an equation where, as in $O(\varepsilon^2)$, the unknowns are $\overline{z_3}$ and Φ_3. From (A.14) we find an expression for Φ_3 in terms of $e^{i\tilde{x}}$ and its harmonics. By isolating the contribution of $e^{i\tilde{x}}$ we obtain the amplitude equation

$$I_3 A_{TT} = IA + \left(I_3^2 + 2I_5\right)|A|^2 A/4. \tag{A.28}$$

where

$$I_5 = \int_{-\infty}^{+\infty} \frac{H_{0\eta}}{(\eta-c)^5} d\eta \text{ and } I = \int_{-\infty}^{+\infty} \frac{H_{2\eta}}{\eta - c} d\eta - 2I_5|A_0|^2 \tag{A.29}$$

and we assume $|A_0| \ll 1$, which is reasonable since we consider small initial perturbations. I, I_3, I_5 are three coefficients of integral form which depend on $H(\eta)$ - the background vertical buoyancy gradient.

This is the general setup for the asymptotic analysis and now we focus, as an example, to the case of $M = 4$ discontinuous interfaces (3.8) for which (3.11) becomes

$$H = G_y = J\Big[\delta(\eta-3) + \delta(\eta-1) + \delta(\eta+1) + \delta(\eta+3)\Big]. \tag{A.30}$$

As we stated in (A.17) the Richardson number expands as $J = J_0 + \epsilon^2 J_2 + \dots$ about the stability boundary $J_0 = \bar{J}_s(c)$. While the subscript s indicates it is the bifurcation point for the sharp interfaces problem, c is the unstable phase velocity of nearest neighbor interfaces

resonances. As we found in (3.49), from the defect limit linear stability analysis when $c = 0$ the critical Richardson number is $\bar{J}_s(0) = 9/10$ and when $c = \pm 2$ it is $\bar{J}_s(\pm 2) = 450/484$. Now if we plug (A.30) into the integral coefficients of (A.28) we find $I_3/\bar{J}(c) = 164/27$, $I_5/\bar{J}(c) = 7300/729$ and $I = 20J_2/9$ and the secular solution of (A.28) becomes

$$|A| = \sqrt{-\frac{I}{I_3^2 + 2I_5}}, \tag{A.31}$$

where to keep the solution real J_2 must be negative, which makes the bifurcation subcritical as is shown with a dashed line in figure 3.13.

We should note that the results of this section rely on two assumptions: the fluid is inviscid and the interfaces discontinuous. While these assumptions allow straightforward analytical results, for numerical purposes are computationally demanding. In our numerical simulations we assume $\nu > 0$ and $d > 0$ which shift the position of the critical Richardson numbers. For these reason, in order to compare the results of the weakly non-linear theory and the numerically computed bifurcation diagram, see figure 3.13, we show the secular solution (3.64) branching out from the $\bar{J}(c, d)$ relative to the thick-interfaces problem found in §3.4.3.

Our last remark in this appendix is about the initial conditions (3.30) and (3.31). If we plug $c = i\,c_0$ into (A.18) we get (3.30), while when $c = 2 + i\,c_2$ we get (3.31), triggering a specific TCI in the fluid.